



NTNU – Trondheim
Norwegian University of
Science and Technology

Structural Safety Assessment of Reinforced Concrete Structures with Nonlinear Finite Element Analyses and the Significance of the Modelling Uncertainty

Application to Structural Walls

Ingrid Nilsen-Nygaard

Civil and Environmental Engineering

Submission date: June 2015

Supervisor: Max Hendriks, KT

Norwegian University of Science and Technology
Department of Structural Engineering



MASTER'S THESIS 2015

SUBJECT AREA: Computational mechanics Concrete Structures	DATE: 10.06.2015	NO. OF PAGES: 150 14+104+32
---	---------------------	--------------------------------

TITLE:

Structural Safety Assessment of Reinforced Concrete Structures with Nonlinear Finite Element Analyses and the Significance of the Modelling Uncertainty
Application to Structural Walls

Konstruksjonssikkerhetsvurdering av armerte betongkonstruksjoner med ikke-lineære elementanalyser og betydningen av modelleringsusikkerheten.
Bruk på konstruksjonsvegger

BY:

Ingrid Nilsen-Nygaard



SUMMARY:

NLFEA in structural safety assessment of reinforced concrete structures introduces potentially significant uncertainties to the design procedure due to complex numerical modelling, requiring comprehension, and management by suitable safety formats. The modelling uncertainty comprises the uncertainties introduced by the solution strategy, the FEA software and the user to the design procedure. Solution strategy is used as a collective term for the finite element model and the analysis procedure.

A structural safety assessment of a reinforced concrete structural wall is performed with emphasis on assessing and evaluating the modelling uncertainty. A solution strategy based on recommendations by *the Dutch guidelines* (DG) is attempted validated for use on structural walls. A significant value of the modelling uncertainty is observed in this study, estimated to a mean ratio of experimental to predicted strength $\theta_m=1.21$ and a coefficient of variation of the modelling $V_0=6.6\%$ for multiple structural walls for the selected solution strategy. The constitutive modelling indicates to be the main contributor to the systematic underestimation of the load capacity. The design capacities from the evaluated safety formats with NLFEA exceed the design capacity assessed by an analytical method of strut-and-tie modelling. Deficiencies and sources of modelling uncertainty are highlighted in the discussions. The observed deficiencies need to be addressed before the selected solution strategy should be defined as validated for use on structural walls in general. Prescribed values of the modelling uncertainty, and no correction of bias in the model in the safety formats, might be improper for many problems. The difficulty of handling bias, and the modelling uncertainty's dependency to a selected solution strategy and software, is stressed during this evaluation. Model validation and a conscious inclusion of the modelling uncertainty into the safety formats confirms as essential for a reliable and possibly profitable use of NLFEA in a structural safety assessment.

SUPERVISOR: Prof.dr.ir.M.A.N. Hendriks, NTNU and University of Delft

CO-SUPERVISOR: Industrial PhD-candidate Morten Engen at NTNU and Multiconsult

CARRIED OUT AT: The Department of Structural Engineering, NTNU

Preface

This report is the result of a master's thesis at the Norwegian University of Science and Technology (NTNU) at the Department of Structural Engineering (KT). The report corresponds to 20 weeks work and 30 study points the spring 2015.

Nonlinear finite element analyses (NLFEA) in a structural safety assessment involve relevant topics such as the modelling uncertainty and global safety formats. My main motivation for this thesis was to increase my knowledge of concrete material behaviour and the use of NLFEA in design of concrete structures. Especially interesting was the relevance of guidelines for NLFEA on concrete structures, which may lead to an increased confidence and efficiency of the method.

I would like to thank my supervisor Prof.dr.ir. M.A.N. Hendriks at NTNU and the University of Delft and co-supervisor Industrial PhD-candidate Morten Engen at NTNU and Multiconsult for helpful guidance and interesting discussions along the way. Their input and advices has contributed to an increased dedication and understanding for the work related to this thesis. Associate Professor Jan Arve Øverli has been helpful with providing necessary literature and in discussions of the analytical calculations. The work has been very educational, and I have appreciated the opportunities to find directions within the main scope to reflect my personal learning goals for this thesis. Thanks to my fellow students for a positive work environment, useful dialogues and great motivation during the semester.

Trondheim, 10.06 2015



Ingrid Nilsen-Nygaard

Abstract

Nonlinear finite element analyses (NLFEA) allow for simulation of the expected *real* nonlinear structural behaviour of reinforced concrete structures. NLFEA in structural safety assessment does however introduce potentially significant uncertainties to the design procedure due to complex numerical modelling, which requires comprehension, and management by suitable safety formats. The modelling uncertainty comprises the uncertainties introduced by the solution strategy, the finite element analysis (FEA) software and the user to the design procedure. Solution strategy is used as a collective term for the finite element model and the analysis procedure.

In this master's thesis, a structural safety assessment of a reinforced concrete structural wall is performed, with emphasis on assessing and evaluating the modelling uncertainty. The nonlinear FEA software DIANA, version 9.6, is used for all the finite element analyses, and a previously experimental test study of structural walls is used as reference case. Validation of a solution strategy based on recommendations by *the Dutch guidelines* (DG) for use on structural walls is focused on, since validated guidelines for NLFEA may help minimize the modelling uncertainty and improve the efficiency of the design method. The actual modelling uncertainty is estimated by a statistical approach to multiple structural walls, and relevant global safety formats are applied in the safety assessment, and evaluated with emphasis on the incorporated value of the modelling uncertainty and the impact on the design capacity. The design capacity is also assessed by an analytical method of strut-and-tie modelling. Deficiencies and sources of modelling uncertainty are highlighted in the discussions. The results should be relevant for further studies on this subject and possibly also for later users of NLFEA in assessment of concrete structures for a safer and more efficient use.

The estimated modelling uncertainty of a mean ratio of experimental to predicted strength $\theta_m=1.21$ and a coefficient of variation of the modelling $V_\theta=6.6\%$ reflects the observed similar behaviour of multiple walls, though at low applied load levels compared to the experimental tests. The constitutive modelling indicates to be the main contributor to the systematic underestimation of the load capacity. The evaluated safety formats provide

design capacities greater than by the analytical method, where the safety format by Schlune et.al and ECOV provide the highest design capacity.

Significant values of the modelling uncertainty are observed in this study. Until the observed limitations in DG and the FEA software DIANA have been addressed, the selected solution strategy should not be considered as validated for use on structural walls in general, based only on this study. Prescribed, low values of the modelling uncertainty and no correction of bias in the model in the safety formats may be improper for many problems. The difficulty of handling bias, and the modelling uncertainty's dependency on a selected solution strategy and FEA software, is clarified during this evaluation. Model validation and a conscious inclusion of the modelling uncertainty into the safety formats is confirmed as essential for a reliable use of NLFEA in structural safety assessment.

Sammendrag

Ikke-lineære elementanalyser (NLFEA) gjør det mulig å simulere den forventede virkelige konstruksjonsresponsen av armerte betongkonstruksjoner. NLFEA i sikkerhetsvurdering av konstruksjoner introduserer imidlertid potensielt betydelige usikkerheter til dimensjoneringsprosedyren på grunn av kompleks numerisk modellering, som krever forståelse og håndtering ved hjelp av passende sikkerhetsformater. Modelleringsusikkerheten omfatter usikkerheten introdusert til dimensjoneringsprosedyren av løsningsstrategien, programvaren for elementanalysene (FEA) og brukeren. Løsningsstrategi brukes som et samlebegrep på elementmodellen og analyseprosedyren.

I denne masteroppgaven blir en sikkerhetsvurdering av en konstruksjonsvegg i armert betong utført, med vektlegging på tilnærming og evaluering av modelleringsusikkerheten. Det ikke-lineære elementprogrammet DIANA, versjon 9.6, brukes i alle elementanalysene, og et tidligere eksperimentelt teststudie på konstruksjonsvegger brukes som referansetilfelle. Det er fokusert på validering av en løsningsstrategi basert på anbefalinger i *de Nederlandske retningslinjer* (DG) til bruk på konstruksjonsvegger, ettersom validerte retningslinjer for NLFEA kan hjelpe å minimere modelleringsusikkerheten og forbedre effektiviteten av dimensjoneringsmetoden. Den faktiske modelleringsusikkerheten er estimert gjennom en statistisk tilnærming ved NLFEA med den valgte løsningsstrategien på flere konstruksjonsvegger. Relevante globale sikkerhetsformater er brukt i sikkerhetsvurderingen av veggen, og evaluert med fokus på den implementerte verdien av modelleringsusikkerheten og dens påvirkning på den dimensjonerende kapasiteten. Analytiske beregninger ved bruk av stavmodeller er også utført for sammenligning. Mangler og kilder til modelleringsusikkerhet er fremhevet i diskusjonene. Resultatene burde være av relevans for videre studier på dette temaet, og muligens for senere brukere av NLFEA i sikkerhetsvurderinger av betongkonstruksjoner for en mer sikker og effektiv bruk.

Modelleringsusikkerheten er estimert til en gjennomsnittsrate av eksperimentell til beregnet kapasitet $\theta_m=1.21$ og en variasjonskoeffisient til modelleringen $V_\theta=6.6\%$ som reflekterer den observerte lignende oppførselen av flere vegger, men for et lavt påført lastnivå

sammenlignet med de eksperimentelle testene. Den numeriske modelleringen av materialene indikeres å være en hovedkilde til den systematiske underestimeringen av lastkapasiteten. De evaluerte sikkerhetsformatene fører til dimensjonerende kapasiteter større enn ved de analytiske beregningene, der sikkerhetsformatet ECOV og det nye sikkerhetsformatet av Schlune et.al gir de høyeste dimensjonerende kapasitetene.

Vesentlig høye verdier av modelleringsusikkerheten er observert i dette studiet. Frem til de observerte begrensningene i DG og FEA programvaren DIANA har blitt undersøkt, bør ikke den valgte løsningsstrategien bli vurdert som validert for bruk på konstruksjonsvegger basert kun på dette studiet. Forhåndsbestemte, lave verdi av modelleringsusikkerheten og ingen korreksjon for $\theta_m \neq 1.0$ i sikkerhetsformatene vil kunne være ukorrekt for mange tilfeller. Vanskeligheten med å håndtere tilfeller der $\theta_m \neq 1.0$, og modelleringsusikkerhetens avhengighet til en valgt løsningsstrategi og elementprogram, er belyst i denne evalueringen. Modellvalidering og en bevisst inkludering av modelleringsusikkerheten i sikkerhetsformatene bekreftes som vesentlig for en sikker bruk av NLFEA i sikkerhetsvurderinger av konstruksjoner.

Contents

Preface.....	i
Abstract.....	iii
Sammendrag.....	v
Abbreviations and nomenclature.....	xi
1 Introduction.....	1
PART I: THEORY	
2 NLFEA in structural safety assessment of reinforced concrete structures	7
2.1 General.....	7
2.2 The design procedure with NLFEA	7
2.2.1 Two-step design procedure.....	8
2.2.2 One-step design procedure	8
2.3 Current practice: existing regulations and guidelines	9
2.4 The modelling uncertainty	11
2.5 Reliability and safety formats in NLFEA	13
2.5.1 The partial safety factor method (PSF).....	14
2.5.2 The global resistance factor method (GRF).....	14
2.5.3 The estimation of coefficient of variation of resistance method (ECOV)...	15
2.5.4 New safety format by Schlune et.al.....	15
3 Material behaviour and numerical modelling of reinforced concrete	17
3.1 Fracture mechanics	17
3.2 Smearred cracking.....	18
3.2.1 Total strain based crack model	18
3.2.2 Shear retention factor.....	19
3.3 Concrete in tension	20
3.4 Concrete in compression.....	20
3.5 Multiaxial behaviour of concrete	22
3.6 Reinforcement and interaction with concrete	24

PART II: SELECTION OF SOLUTION STRATEGY

4	Case study framework	27
4.1	Experiment by Lefas et.al on reinforced concrete structural walls.....	27
4.1.1	Results from experimental study	28
4.1.2	Previous studies	28
4.2	Solution strategy based on <i>the Dutch guidelines</i> (DG).....	29
4.2.1	Preliminary analyses	29
4.2.2	Finite element discretization.....	30
4.2.3	Geometry, boundary constraints and loading	32
4.2.4	Numerical material modelling in DIANA	35
4.2.5	Solution procedure.....	42
5	NLFEA results from the case study.....	45
5.1	Results from the base models	45
5.1.1	Concrete cracking and reinforcement yielding.....	46
5.1.2	Global failure	47
5.1.3	Stiffness	47
5.1.4	Multiaxial stress state	51
5.1.5	Concrete expansion.....	53
5.1.6	Summary of the results from the base models.....	55
5.2	Sensitivity study of the base models	55
5.2.1	Objective and results presentation	56
5.2.2	Mesh sensitivity	56
5.2.3	Tensile behaviour and crack models.....	57
5.2.4	Compressive behaviour	57
5.2.5	Concrete expansion and passive confinement effect.....	58
5.2.6	Summary of the sensitivity analyses	59
6	Discussion of results from the case study.....	61
6.1	Multiaxial stress effects	61
6.1.1	Concrete confinement effects	61

6.1.2	Volumetric concrete expansion	62
6.2	Concrete compressive behaviour	63
6.3	Concrete tensile behaviour and structural stiffness	64
6.4	Other observed effects	65
6.5	Selection of solution strategy	66
PART III: THE MODELLING UNCERTAINTY AND STRUCTURAL SAFETY ASSESSMENT		
7	Estimation of the modelling uncertainty.....	69
7.1	Introduction.....	69
7.2	Application of the selected solution strategy to multiple structural walls	69
7.2.1	Revised results from the experiment by Lefas et.al.....	69
7.2.2	Revised solution strategy	69
7.2.3	Results from NLFEA of multiple walls.....	72
7.3	Estimation of the modelling uncertainty	78
8	Structural safety assessment of a structural wall	81
8.1	Assessment by an analytical method: Strut-and-tie modelling.....	81
8.1.1	Strut-and-tie models.....	82
8.1.2	Results from the strut-and-tie models.....	82
8.2	Assessment with NLFEA with safety formats	84
8.2.1	Material parameters in the safety formats	84
8.2.2	Results from NLFEA with safety formats	86
8.2.3	Study of the effect of the modelling uncertainty	87
8.3	Summary of results from the structural safety assessment	88
9	Discussion of results – the modelling uncertainty and structural safety assessment.	91
9.1	Estimation of the modelling uncertainty	91
9.1.1	General results and model validation	91
9.1.2	Similar studies	92
9.1.3	Sample size and the modelling uncertainty factor	92
9.2	Structural safety assessment.....	92

9.2.1	General results	92
9.2.2	Reliability level and inclusion of the modelling uncertainty.....	93
9.2.3	The influence of the modelling uncertainty.....	93
PART IV: CONCLUSIONS AND RECOMMENDATIONS FOR FUTHER WORK		
10	Conclusions	97
11	Recommendations for further work.....	99
References.....		101
Appendices.....		105

Abbreviations and nomenclature

Abbreviations

CPU	Central Processing Unit
DG	The Dutch Guidelines
EC2	Eurocode NS-EN-1992-1-1
ECOV	Estimation of coefficient of variation of resistance method
FEA	Finite element analysis/analyses
FEM	Finite element method
<i>fib</i>	International Federation for Structural Concrete
GRF	Global resistance factor method
JCSS	Joint Committee on Structural Safety
LFEA	Linear finite element analysis/analyses
LS	Load step
NLFEA	Nonlinear finite element analysis/analyses
NLFEM	Nonlinear finite element method
PSF	Partial safety factor method
SFLC	<i>Spurious full lateral constraint</i>
SLS	Serviceability limit state
SRF	Shear retention factor
STM	Strut-and-tie model
ULS	Ultimate limit state
2D	Two-dimensional
3D	Three-dimensional

Nomenclature

b	Width of the wall
c	Concrete cover of main reinforcement
d_{\max}	Maximum aggregate size
f_c	Concrete cylinder compressive strength

f_{cu}	Concrete compressive cube strength
f_t	Concrete cylinder tensile strength
f_{cf}	Confined concrete compressive strength
f_{cm}	Mean concrete cylinder compressive strength
f_{ctm}	Mean concrete cylinder tensile strength
f_{lat}	Hydrostatic pressure/lateral stress
f_u	Ultimate strength of the reinforcement steel
f_y	Yield strength of the reinforcement steel
$f_{\Delta i}$	Reduced material strength in safety format by Schlune et.al
Δf	Reduction of material strength in safety format by Schlune et.al
h	Height of wall
h_{eq}	Equivalent length; crack bandwidth in tension; crushing bandwidth in compression
h_R	Strain hardening modulus
l_{av}	Average crack spacing
$l_{e,max}$	Maximum finite element side length
n_{cr}	Number of cracks within a finite element, modification factor of the tensile fracture energy.
p	Equivalent plastic strain
r	Parameter to represents the nonlinear analysis
s	Distance from location of FT to tensile wall edge
$s_{r,max}$	Maximal crack spacing
t	Thickness of the wall
x	Compressive zone width
z	Internal moment arm
A	Area of a two-dimensional element
$A_{c,ef}$	Effective area of concrete in tension
A_s	Reinforcement area per unit length
E_c	Young's modulus of the concrete
E_{har}	Hardening modulus
E_s	Young's modulus of the reinforcement steel
F_C	External compressive force

F_H	Applied horizontal load
F_T	External tensile force
F_V	Applied vertical load
G_c	Compressive fracture energy
G_F	Fracture energy
G_F^{RC}	Modified tensile fracture energy
G_{F0}	Parameter for the fracture energy
K_ε	Peak strain factor
K_σ	Peak stress factor
N_i	External forces in crack spacing calculation
R_d	Design load capacity (resistance) of the structure
R_{exp}	Ultimate capacity (resistance) of the structure from experiment
R_u	Ultimate predicted load capacity (resistance) of the structure
V	Volume of a solid element
V_f	Coefficient of variation of the variable to model the modelling uncertainty
V_g	Coefficient of variation of the variable to model the modelling uncertainty
V_R	Coefficient of variation of the resistance
V_θ	Coefficient of variation of the variable to model the modelling uncertainty
α	Concrete compressive strain in parabolic curve by DIANA; Threshold angle in multi-directional crack model
α_{cc}	Reduction factor to concrete design strength in EC2
α_{lat}	Average lateral damage variable
α_R	Sensitivity factor for the resistance side
β_R	Reliability index on the resistance side
$\beta_{\sigma cr}$	Maximum strength reduction factor
δ	Displacement
Δ_{fi}	Reduction value of material strength in safety format by Schlune et.al
ε	Strain
ε_c	Concrete compressive strain
ε_{cu}	Concrete compressive ultimate strain
ε_{c0}	Concrete compressive strain at compressive strength
ε_u	Concrete tensile strain defining shape of exponential tension softening curve

ϵ_V	Volumetric strain
ϵ_0	Concrete tensile strain at tensile strength
γ	Ratio of ultimate predicted mean load capacity to design load capacity
γ_c	Partial safety factor for concrete
γ_{GL}	The global safety factor in GRF
γ_s	Partial safety factor for steel
γ_R	Global resistance factor in GRF; Global safety factor in ECOV and safety format by Schlune et.al
γ_{Rd}	The modelling uncertainty factor
$\rho_{s,ef,i}$	Ratio of reinforcement area to effective concrete area
σ	Stress
τ_{bms}	Mean bond strength between steel and concrete
θ	Variable to model the modelling uncertainty; Crack angle; Angle in strut-and-tie model frame
θ_m	Mean ratio of experimental to predicted load capacity
ν	Poisson's ratio
ϕ_i	Reinforcement bar diameter

General subscripts

m	Mean value
k	Characteristic value
d	Design value
c	Concrete; compression
i	Random variable
x	Coordinate
y	Coordinate; yield
u	Ultimate value

1 Introduction

Verification of structural design by use of numerical simulations and global safety formats was recently adopted as an alternative design method in *fib* Model Code 2010 [1]. The nonlinear finite element method is considered a relevant method for structural analyses of reinforced concrete structures, by including important nonlinear phenomena such as redistribution of internal forces during loading, and nonlinear material behaviour by concrete cracking and reinforcement yielding. Re-assessment of existing concrete structures may require nonlinear structural analyses to acquire the intended reliability level or to avoid conservative approaches for new-builds.

Nonlinear finite element analyses (NLFEA) are to date mainly used as a second step in the design procedure, for capacity control of critical structural sections, where linear finite element analyses (LFEA) govern the global load distribution. A one-step design procedure utilizes NLFEA directly in a structural safety assessment, and hence includes the global nonlinear behaviour of concrete structures. Only the real material parameters can simulate the realistic structural behaviour, and an additional global safety format is required to fulfil the reliability requirements of the structural design [1]. Various safety formats are available, and the subject of correct inclusion of *the modelling uncertainty* is recently much discussed [2-4].

NLFEA introduces a potential for significant uncertainties in all steps from idealization of the physical problem, discretization into finite elements, numerical material modelling, selection of solution procedures and the final interpretation of the analyses. Solution strategy is further used as a collective term of the complete finite element model and analysis procedure [5], and *the modelling uncertainty* is defined as the uncertainty introduced by the solution strategy, the finite element analysis (FEA) software and the user to the design procedure [4]. The modelling uncertainty needs to be accounted for in a suitable global safety format, along with uncertainties in material and geometrical dimensions.

Previous studies reveal significant variations of the modelling uncertainty for various structural types and failure modes [4], however research work remains for further

estimation of the uncertainty and development of strategies for managing this. Model validation is an essential step in the design procedure to limit the modelling uncertainty [6]. Published guidelines for NLFEA on concrete structures can provide recommendations that defines suitable solution strategies verified for various structural types, which may reduce the modelling uncertainty and enhance the efficiency of the design procedure.

In relation to recent and ongoing studies on the modelling uncertainty [3, 5, 7], this thesis aims at examining the significance of the modelling uncertainty by a structural safety assessment of a reinforced concrete structural wall using NLFEA. A major focus will be given the model validation aspect, by an attempt to validate a solution strategy based on the recommendations given in *the Dutch guidelines* (DG) for use on structural walls [8]. Through a comprehensive model validation process and further evaluation of relevant global safety formats for assessment of the structures design capacity, the uncertainty associated with a solution strategy and the FEA software used will be visualized and discussed. Special attention is given to the inclusion of the modelling uncertainty in the safety formats, and the influence on the design capacity.

A previous experimental study of multiple structural walls is selected for further study, to enable comparison of the analysis results to the test results [9]. A case study on a reinforced concrete structural wall is used to evaluate a solution strategy based on *the Dutch guidelines* (DG), both idealized as a plane stress problem and as a solid problem. The case study and supporting discussion result in selection of a solution strategy for use in the structural safety assessment. The structure is discretized with a coarse mesh to improve the efficiency of the design method. The modelling uncertainty is estimated through a statistical approach by utilization of the selected solution strategy to multiple structural walls. The structural safety assessment is performed for a structural wall using both an analytical method by strut-and-tie modelling for comparison with a traditional analysis method, and four relevant safety formats. The estimated modelling uncertainty is compared to the prescribed values provided by *fib* Model Code 2010, and the effect on the design capacity is evaluated.

The thesis is divided into four parts:

- **PART I: THEORY**

Chapter 2: Introduction to NLFEA in structural safety assessment and relevant guidelines and safety formats. Chapter 3: Theory of material behaviour and numerical modelling of reinforced concrete.

- **PART II: SELECTION OF SOLUTION STRATEGY**

Chapter 4 & 5: Defining and evaluating a solution strategy based on recommendations by DG in a case study on a structural wall specimen, with both two – and three-dimensional finite elements. Chapter 6: Discussion of the observed effects from the case study, resulting in a selection of a final solution strategy for further use on structural walls in this study.

- **PART III: THE MODELLING UNCERTAINTY AND STRUCTURAL SAFETY ASSESSMENT**

Chapter 7: Estimation of the modelling uncertainty by using the selected solution strategy on multiple structural walls with varying geometry, concrete strength and applied loading. Chapter 8: Structural safety assessment of a structural wall specimen applying analytical method of strut-and-tie modelling and by NLFEA, with the relevant safety formats. Chapter 9: Discussion of the effect of the various safety formats and the significance of the modelling uncertainty in the design procedure.

- **PART IV: CONCLUSIONS AND RECOMMENDATIONS FOR FURTHER WORK**

Chapter 10: Conclusions regarding the applicability of the selected solution strategy to structural walls, the various safety formats evaluated and the significance of the modelling uncertainty. Chapter 11: Recommendations for further work.

PART I: THEORY

2 NLFEA in structural safety assessment of reinforced concrete structures

2.1 General

Finite element method (FEM) is commonly used for numerical solving of continuum problems. The numerical method is by definition not an exact solution, where a physical problem is discretized into elements of finite sizes. In the displacement method, the shape of a displacement field within the elements is assumed and equilibrium is solved by integral [1]. By enforcing equilibrium and compatibility at the element nodes, the systems stiffness relationship can be defined and the global nodal displacements calculated. In a nonlinear finite element analysis, the stiffness and load often becomes functions of the displacement, and the relation between force and displacement vectors hence nonlinear that requires nonlinear equilibrium solutions by an iterative scheme. Appropriate convergence criteria govern the accuracy of the solution procedure. An analysis procedure with nonlinear finite element analyses (NLFEA) comprises definition of a suitable finite element model and a suitable analysis procedure. The definition *solution strategy* by Engen is used throughout the thesis as a collective term of the choices regarding finite element type and integration scheme, material models, iteration method and convergence criteria [5]. The uncertainties introduced to the design procedure with NLFEA by the selected solution strategy, FEA software and possible user factors is termed *the modelling uncertainty*.

2.2 The design procedure with NLFEA

Inclusion of nonlinear material behaviour such as cracking of the concrete and yielding of the reinforcement and allowing for redistributions of internal forces provides the possibility to assess the realistic structural global response. A nonlinear finite element analysis can handle nonlinearities in material, geometry and contact conditions, where the nonlinear material behaviour is the most prominent in reinforced concrete structures in general [6]. Superposition of load cases is not applicable due to the nonlinear nature of the analysis method, and the loading history is often of great importance [10]. This generates new challenges for use of NLFEA on large concrete structures with complex loading conditions,

though this topic will not be further addressed in this thesis. An ongoing PhD study by Engen addresses this topic in detail [11].

An accurate solution strategy can consequently serve as a virtual test of the structures and substitute comprehensive physical experiments. Only implementation of the *real* material parameter values, implemented to suitable material models that comprise modelling of all relevant material behaviour and properties for the specific problem, can reproduce the realistic structural behaviour [1, 8]. Mean material parameters, or in-situ mean material parameters for existing structures, define the materials most likely strength and behaviour. Design material strengths by use of partial safety factors provide low values of the material parameters and can produce inaccurate failure mode and an unrealistic structural behaviour [12].

2.2.1 Two-step design procedure

Until recently, the design procedure with nonlinear finite element analyses has mainly comprised a two-step procedure with safety assessment of the structure at sectional level only, illustrated as the left path in Figure 2.1. The first step assesses the distribution of elastic internal forces produced by the external loading by linear finite element analyses (LFEA), using linear-elastic material properties. The second step utilizes NLFEA for capacity estimation of critical cross sections, and the safety of the structure can therefore only be verified at a sectional level. The two-step procedure directly defines the design capacity and design action effects by use of partial safety factors in accordance with Eurocode 1992-1-1 [13]. A significant advantage of LFEA is the validity of the principle of linear superposition. However, the incompatible constitutive relations in LFEA and NLFEA yields an inconsistent solution and only local verification of the structural capacity.

2.2.2 One-step design procedure

NLFEA with mean material parameters allows for a realistic assessment of the structural behaviour, and requires a reliability assessment at a global level by a suitable global safety format. The path to the right in Figure 2.1 illustrates how NLFEA may be used directly in structural safety assessment of a concrete structure. Note that the total schematic illustration in Figure 2.1 is defined for design of large concrete structures, keeping the early design by LFEA [11]. A structural analysis using NLFEA with mean material parameters transforms the applied loading into internal forces and predicts the most realistic structural response

by the selected solution strategy. To control the global design capacity of the structure, a suitable global safety format must be applied. *fib* Model Code 2010 was published in 2013, including recommendations for verification of design assisted by nonlinear numerical solution with safety formats. The most relevant safety formats are presented in section 2.5. The safety assessment on a global level will depend on the structural failure mode and the structural system behaviour [12]. A solution strategy for safety assessment based on nonlinear analysis requires model validation to assure accurate and objective results [6].

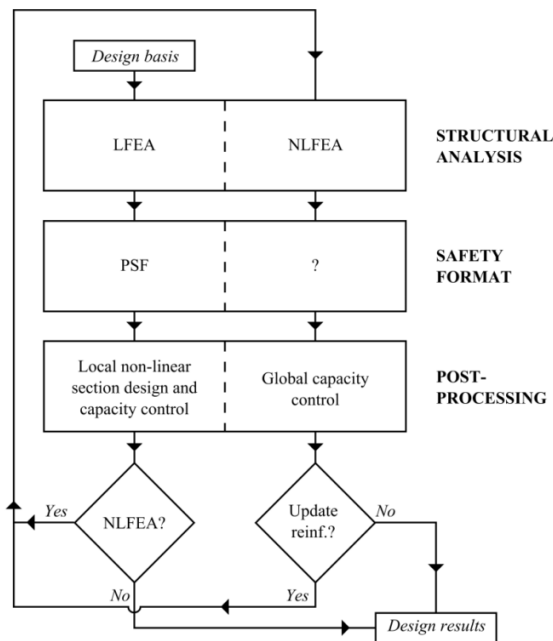


Figure 2.1: Schematic illustration of possible design procedure with NLFEA in design of concrete structures [11].

2.3 Current practice: existing regulations and guidelines

Nonlinear finite element analyses has been performed on concrete structure for over 40 years [14], and the following summarizes important sources of regulations and guidelines used in assessment of concrete structures. To date, an unambiguous approach for nonlinear finite element analysis on reinforced concrete structures does not exist [15]. The failure mode, the structural type, the selected solution strategy and FEA software used in the analyses will affects the results. Significant uncertainties are expected, and experience and knowledge by the analyst is required for reliable results [14]. Well-validated solution

strategies provided by guidelines could both increase the efficiency and reliability of the design procedure and limit the modelling uncertainty. Numerical simulations in verification of design and global safety formats for the purpose of structural safety assessment with NLFEA are relevant topics in the research environment to date [1, 2, 4, 6].

Eurocodes

Eurocode NS-EN-1992-1-1 (EC2) provides a thorough set of technical rules for design of concrete structures in buildings in SLS and ULS [13]. General recommendations for nonlinear analysis methods are provided, with requirements for implementation of suitable material nonlinearity, accurate stiffness reproduction and sufficient consideration of uncertainties. EC2 provides a nonlinear constitutive relation for concrete in uniaxial compression and for confined concrete due to constrained concrete expansion. For design of discontinuity regions with nonlinear distribution of strains EC2 suggests strut-and-tie modelling (STM) that follows the lower bound theorem of plasticity. Eurocode 1992-2 for bridges includes a safety format consistent with the global resistance safety factor method (GRF) described in section 2.5 [16].

fib

The International Federation for Structural Concrete (*fib*) serves state-of-the-art concrete knowledge for concrete structures. The *fib* Model Code 2010 also includes recent developments and new ideas, and recently the design procedure by numerical simulation was included as an alternative method of design of concrete structures [1]. The required reliability level is ensured by use of provided global safety formats, and the *fib* Model Code 2010 recommends use of minimum two different safety formats for an independent verification of the design capacity. The provided safety formats enable evaluation of safety based on various levels of use of probabilistic theory, presented in section 2.5 [1]. The *fib* Bulletin 70 includes background information of the *fib* Model Code 2010, especially relevant is the background for the recommended constitutive modelling of reinforced concrete [17]. *fib* also provides the Bulletin No. 45, a practical guide to finite element modelling of concrete structures where an overview of relevant numerical modelling concepts of reinforced concrete is given [15].

The Dutch guidelines (DG)

The Dutch Ministry of Infrastructure and the Environment in 2012 published a technical report containing guidelines for NLFEA on reinforced concrete beams and girders under

quasi-static and monotonic loading, as a state-of-the-art within NLFEA for concrete structures [8]. This is further referred to as *the Dutch guidelines* (DG). The main objective for the guidelines was for use in safety assessment of existing infrastructure to estimate the full ultimate structure capacity. DG provide specifications for a complete solution strategy by finite element modelling and analysis procedure, leaving subjective selections by the analyst to a minimum. DG are closely connected to the *fib* Model Code 2010. A validation of the guidelines to other structural types could assist future users and approach the desire of a general solution strategy with low modelling uncertainties.

Other

Chalmers University of Technology in 2008 published a guideline for NLFEA on concrete bridges in shear and torsion [18]. M.Sc. Morten Engen is currently working on an industrial PhD study on application of nonlinear finite element analysis in design of large concrete structures, with aim of a robust solution strategy for NLFEA to be used in the offshore industry [11]. Safety formats for NLFEA is a widely discussed subject to date, e.g. Schlune et.al in 2012 proposed a new safety format with a new approach to the material uncertainty estimation and direct inclusion of the experienced modelling uncertainty that has been further studied by several researches recently [2, 4, 6, 12]. The Joint Committee on Structural Safety (JCSS) provides the JCSS Probabilistic Model Code presenting state-of-the-art probabilistic approaches, and new developments within safety formats and the definition of the modelling uncertainty [19].

2.4 The modelling uncertainty

Idealizations from the physical structure, discretization into finite elements, combining of material models, solution procedures, the FEA software utilized and user interference all contribute to uncertainties in the results, and are summarized as *the modelling uncertainty*. Vecchio discussed the importance of the awareness of questions regarding reliability and accuracy in a NLFEA of concrete structures [14]. Numerous material behaviour models and possible incompatibility between the models, diversity in basic theoretical approaches to numerical modelling of concrete, inappropriate choice of FEA software and incomplete knowledge and experience are all factors that could increase the modelling uncertainty. Figure 2.2 visualizes the diversity in NLFEA results performed in a “blind” competition by simulation of a simple orthogonally reinforced panel under monotonic loading, resulting in

about 30 entries from also highly reputable researches on the topic [14]. The experimental results were unknown during the competition, contributing to high modelling uncertainties since specific selections to the solution strategy regarding e.g. failure mode and observed material behaviour was not possible.

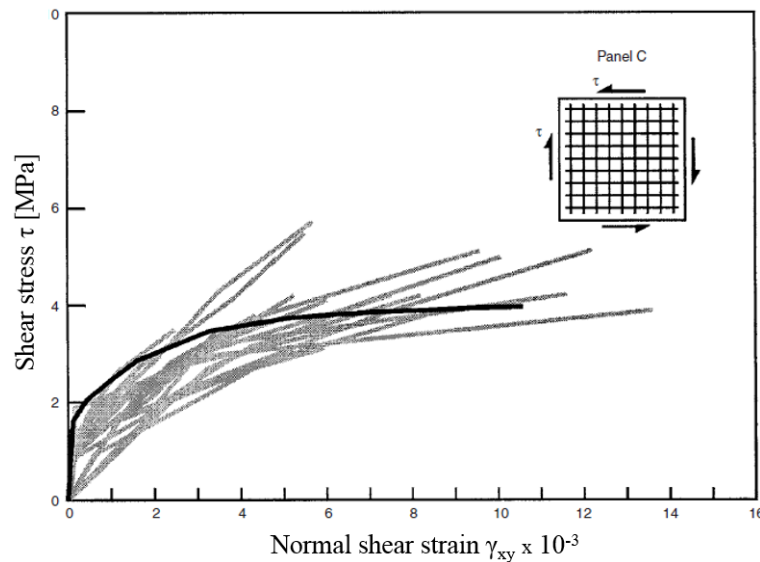


Figure 2.2: Results from “blind” competition on NLFEA of a panel [14].

Cervenka indicated that the modelling uncertainty can be reduced by model validation [6]. The term model validation is used herein considering the validation of the applicability of a solution strategy and FEA software to a certain structural type. The validation should comprise a justification of the approximations done in selection of the constitutive models and the discretization into finite elements, confirmed by prediction of the correct structural behaviour [1]. *fib* Model Code 2010 requires physical material tests to validate the constitutive relations, structural tests to validate the solution strategy and the FEA software’s ability to simulate the correct structural behaviour and a mesh validation to a minimum of three different finite element sizes that should provide similar results [1]. Validation of the structural response is performed by benchmarking calculations on a similar structure as to be assessed [6]. Estimation of the modelling uncertainty is a final step in the model validation process, quantifying the actual numerical model behaviour compared to known results from experiments.

Assuming a typical lognormal distribution the structural capacity [1], the modelling uncertainty can be quantified by two parameters θ_m and V_θ according to JCSS [19]. θ_m is the mean ratio of experimental to numerically predicted strength of all analyses, and V_θ is the corresponding coefficient of variation of modelling. V_θ illustrates the variation of the analysis results and $\theta_m \neq 1.0$ implies a bias in the NLFEA results, hence θ_m may be referred to as the bias factor. NLFEA on multiple structural types using a selected solution strategy would ideally result in an unbiased estimate with a low coefficient of variation, implying an average exact estimation of the ultimate load capacity and thus a well-validated model. Experiments have proved modelling uncertainty sensitivity to both structural type and failure mode, Schlune et.al report results for the coefficient of variation of modelling of 5-30% for bending failure and 15-40% for shear failure [4].

2.5 Reliability and safety formats in NLFEA

Assessment of the structural safety for achieving the required structural reliability level is the final step of the design procedure with NLFEA. Application of a suitable global safety format to the ultimate load capacity from NLFEA with mean material parameters, estimates the design capacity. The design capacity is affected by uncertainties in the materials, the geometrical dimensions and in the modelling, that all need to be treated in a satisfactory approach to obtain the required reliability level [4]. *fib* Model Code 2010 offers assessment of the design resistance R_d on three levels based on probabilistic theory; full probabilistic method for a given reliability index β or failure probability P_f , a global resistance method and a partial safety factor method. The two latter approaches are considered as most relevant for practical design. *fib* Model Code 2010 offers two global resistance methods in addition to the partial safety factor method (PSF) for assessment of the structural safety and estimation of the structural design resistance in ultimate limit state. The global resistance method is a simplified probabilistic approach based on approximations to estimate the design resistance, while the partial safety factor method utilizes design values of the material parameters directly in a global safety evaluation. The safety formats listed below are also provided in *the Dutch guidelines* (DG) [8].

- The partial safety factor method (PSF)
- The global resistance factor method (GRF)

- The estimation of coefficient of variation of resistance method (ECOV)

The global safety formats manage the structure resistance part of the global resistance verification, and the design actions must be treated by the Eurocode format [13]. Schlune et.al in 2012 proposed a new safety format as an *improved ECOV* method, based on an experienced unsafe approach of the current safety formats by not satisfactorily accounting for the modelling uncertainty [4]. This safety format is not included in the *fib* Model Code 2010 or DG to date, though is recently positively referred to by reputable researchers [2, 12].

- The new safety format proposed by Schlune et.al

The four safety formats are evaluated in a safety assessment of a structural wall in PART III, and are presented in detail below. A function r is used for representation of the nonlinear analysis with the specified material parameters [1].

2.5.1 The partial safety factor method (PSF)

Eurocode 1992-1-1 (EC2) utilizes the method of partial safety factors for design at sectional level, and the basic variables in the analysis are treated as deterministic values. For use of PSF in NLFEA, the design resistance is directly calculated by implementing the design values of the material parameters calculated by use of partial safety factors $\gamma_S=1.15$ and $\gamma_C=1.5$, and additionally reduced to account for the modelling uncertainty by the modelling uncertainty factor $\gamma_{Rd}=1.06$ [1].

$$R_d = r(f_d, \dots) \quad (2.1)$$

2.5.2 The global resistance factor method (GRF)

The global resistance of the structure is treated as a random variable. Reduced mean material parameters $f_{cm}=0.85f_{ck}$ and $f_{ym}=1.1f_{yk}$ results in the unique safety factor γ_{GL} for both concrete and steel. The combination of the partial factor of resistance $\gamma_R=1.2$ and the modelling uncertainty factor $\gamma_{Rd}=1.06$ resulting in the global safety factor $\gamma_{GL}=1.27$ [1]. It

is not possible to include a higher value of the modelling uncertainty factor in this safety format.

$$R_d = \frac{r(f_{mGRF}, \dots)}{\gamma_{GL}} \quad (2.2)$$

2.5.3 The estimation of coefficient of variation of resistance method (ECOV)

The method assumes a lognormal distribution described by the mean resistance $r(f_{cm}, \dots) = R_{um}$ and the coefficient of variation V_R of the resistance. A material sensitivity study in two nonlinear analyses with mean and characteristic values of the material parameters respectively determines V_R . The global resistance factor γ_R applies for the mean resistance, and for a 50-year reference period at ULS verification the reliability index $\beta = 3.8$ should be used for a satisfactory reliability level with a sensitivity factor $\alpha_R = 0.8$ for new structures [1]. The modelling uncertainty factor $\gamma_{Rd} = 1.06$ is advised to increase for poorly validated models.

$$V_R = \frac{1}{1.65} \ln \left(\frac{r(f_{cm}, \dots)}{r(f_{ck}, \dots)} \right) \quad (2.3)$$

$$\gamma_R = e^{\alpha_R \beta V_R} \quad (2.4)$$

$$R_d = \frac{r(f_{cm}, \dots)}{\gamma_{Rd} \gamma_R} \quad (2.5)$$

2.5.4 New safety format by Schlune et.al

Schlune et.al questioned the improper modelling uncertainty implementation in the current safety formats [4]. The new safety format can be interpreted as an *improved ECOV* and assumes a lognormal distribution of the resistance. The resistance uncertainty is governed by a global safety factor γ_R , and the coefficient of variation of the resistance is explicitly defined by the three coefficient of variations of the material, geometrical and modelling by respectively V_f , V_g and V_θ in formula 2.6. An estimated value of V_θ can hence be explicitly included, and possible bias in the results is corrected for by including the bias factor θ_m in the global safety factor γ_R , referring to formula 2.10 [4]. For existing structures, mean in

situ concrete strength $f_{cm, is} = 0.85f_{cm}$ should be used. Schlune et.al propose two additional nonlinear analyses for a material sensitivity study to assess V_f , with reduction of the two basic material parameters related to failure by one at the time by Δf_i . That is the concrete compressive strength f_{cm} and the reinforcement steel yield strength f_{ym} . A step size parameter c and the coefficient of variation of the in situ material strengths are additional information required, Schlune et.al recommend $c=2.15$ for most accurate results from experimental experiences [4].

$$V_R = \sqrt{V_\theta^2 + V_g^2 + V_f^2} \quad (2.6)$$

$$\Delta f_i \approx f_i(1 - e^{-cV_i}) \quad (2.7)$$

$$f_{\Delta i} \approx f_{im} - \Delta f_i \quad (2.8)$$

$$V_f \approx \frac{1}{r(f_{cm}, \dots)} \cdot \sqrt{\left(\frac{r(f_{cm}, \dots) - r(f_{cm} - \Delta f_c, f_{ym}, \dots)}{\Delta f_c} \right)^2 \sigma_{f_c}^2 + \left(\frac{r(f_{cm}, \dots) - r(f_{cm}, f_{ym} - \Delta f_y, \dots)}{\Delta f_y} \right)^2 \sigma_{f_y}^2} \quad (2.9)$$

$$\gamma_R = \frac{e^{\alpha_R \beta V_R}}{\theta_m} \quad (2.10)$$

$$R_d = \frac{r(f_{cm}, \dots)}{\gamma_R} \quad (2.11)$$

3 Material behaviour and numerical modelling of reinforced concrete

During the following case study in Part II, it will turn out that the modelling of the material is likely to be the main contributor to the load capacity limitation. A more thorough theory section regarding general concrete behaviour and numerical material modelling of reinforced concrete is consequently given. The specific material models used in the case study are presented in section 4.2.4.

3.1 Fracture mechanics

Fracture mechanics defines failure in a material by an energy criterion, often accompanied with a strength limit [20]. Concrete design codes such as EC2 do not depend on fracture mechanics, though to avoid spurious mesh sensitivity of the concrete failure it is recommended to utilize [20]. Fracture mechanics handles the energy release in a failure zone. Size effects and mesh sensitivity can be overcome by defining the post-peak behaviour in the concrete constitutive models to the fracture energy G_F and the equivalent length h_{eq} illustrated in Figure 3.2(b). Basic fracture mechanics divides fracture in a material into three modes where mode I is in general of highest interest for engineering approach of concrete behaviour, see Figure 3.1 [21]. This fracture energy is defined as the required energy for development and opening of a unit area of a crack [22].

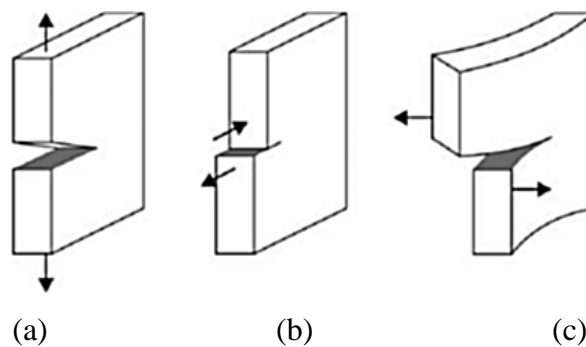


Figure 3.1: Three fracture modes (a) Mode I: opening mode, (b) Mode II: in-plane shear and (c) Mode III: out-of-plane shear [21].

3.2 Smearred cracking

Cracking in concrete is physically a geometrical discontinuity. The two main approaches for numerical modelling of cracks are by discrete or smeared cracking. Modelling of discrete cracking disconnects nodes and creates discrete cracks at the interfaces between finite elements, which violates the displacement method in FEM and limits the crack locations to the interface between the finite elements [23]. An alternative is to model the effect of the cracking as smeared, with a crack band that smears the effect of cracking over a crack bandwidth h_{eq} , with dependency to the fracture energy to ensure an energy-equivalent fracture process [22]. Smeared cracking is in general preferred for use in structures where multiple cracks are expected, and is based on averaged stresses and strains [24]. The fracture energy is also modelled as smeared, where infinitely many small cracks with equally small crack openings releases energy uniformly distributed within the crack bandwidth [20]. The material stiffness matrix is altered at the initiation of the first crack, from isotropic elastic to orthotropic, which results in a reduced stiffness in the direction perpendicular to the crack. The equivalent length h_{eq} is interpreted as the fracture process zone and refer to the crack bandwidth in tension and the crushing bandwidth in compression.

3.2.1 Total strain based crack model

Vecchio and Collins introduced the modified compression field theory, which utilizes a total strain based model for describing stresses and strains [25]. A single relation for stresses and strains describes the tensile and compressive behaviour, where the stress becomes a function of the strain. The total strain based crack model is suitable for ultimate limit state analyses with failure mainly due to cracking or crushing of the concrete [24].

The total strain crack model evaluates stresses in the crack directions. Orthogonal crack models are commonly used, and can be defined as either fixed or rotating with respectively constant or continuously updated crack orientations. Fixed crack models restrain any change of the crack direction after initiated cracking, and the stresses and the strains are evaluated in a fixed coordinate system. The rotating crack model rotates the materials orthotropic axes to coincide with the principal strain axes at all times, and stresses and strains are evaluated along the direction of the principal strains. Smeared orthogonal crack

models can in general lead to shear stress locking and fixed crack orientation can further give too stiff behaviour [23, 26]. Rots and Blaauwendraad found that the stress locking is mesh objective, with explanation that displacement compatibility is violated independent of the finite element size [23]. Stress locking issues might be solved by use of a non-orthogonal crack model such as the multi-directional fixed crack model, that does not constrain the cracks to be orthogonal [24]. This crack model however requires a manual input of a threshold angle α at which a new crack initiates when reached, due to a rotating principal stress field after initial cracking [23].

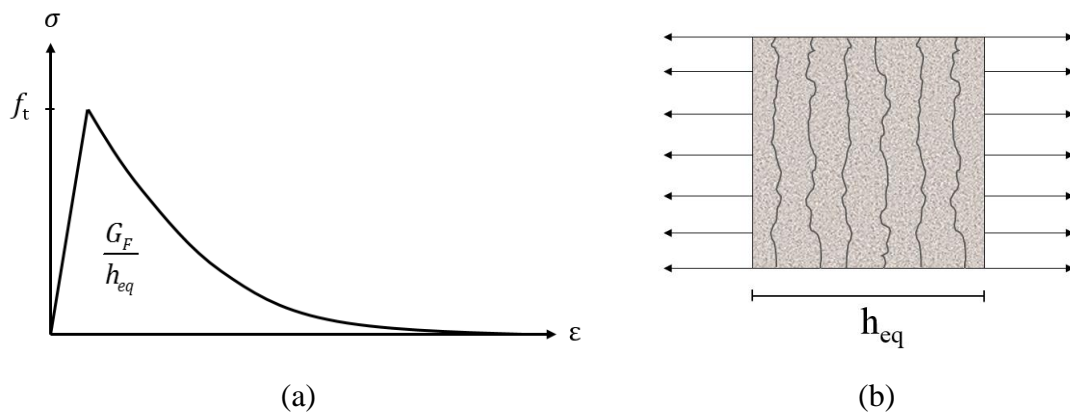


Figure 3.2: (a) Tension softening relation based on fracture energy G_F (b) illustration of smeared cracks in a finite element with equivalent length h_{eq} .

3.2.2 Shear retention factor

The concrete's ability to transfer shear parallel to the crack for small crack widths is referred to as aggregate interlock or shear retention [21]. A shear retention factor (SRF) is necessary to define in a fixed crack model to reduce the shear stiffness in cracked concrete, and hence specify the shear behaviour in cracked concrete by retaining only a percentage of the elastic shear capacity [26]. A variable shear retention factor is often recommended to limit user contribution to an unrealistic value of the SRF [8, 26]. A constant shear retention factor can be interpreted as a value of aggregate interlock in the model, and should be given a value larger than zero to avoid numerical instabilities. Gonzales recommended a SRF of 0.1 as a low value, though high enough to avoid numerical instabilities [27]. A too high value for the constant SRF can result in a non-conservative prediction of the structural capacity and severe shear stress locking behaviour [26].

3.3 Concrete in tension

Plain concrete is a brittle material where cracks develop perpendicular to the stress direction when exceeding the concrete tensile strength, which is in general about 10 times smaller than the compressive strength [28]. The concrete is assumed linear elastic until exceedance of the concrete tensile strength. Small bridging stresses remains across the crack for small crackwidths, and a tension softening relation describes the descending bridging stresses for increasing concrete tensile strains in the post-peak region [15]. Using a smeared crack model, the softening branch should be defined on the fracture energy G_F to reduce mesh sensitivity, as illustrated in Figure 3.2(a). Reinforced concrete structures gain much of their tensile capacity from the reinforcement and its interaction to the concrete, see section 3.6.

3.4 Concrete in compression

A concrete cylinder in uniaxial compression will behave linear elastic until about $0.3f_c$, where f_c is the concrete compressive strength [28]. At this point stable microcrack propagation initiates with following material stiffness reduction. The compressive strength f_c defines a vertex, initiating a descending branch with macrocracking, until the ultimate compressive strain is reached and compressive failure occurs. Until approximately $0.8f_c$, concrete exerts compacting, implying a decrease of the initial concrete volume. A point of minimum volume is reached at this stress level, and dilatation occurs as a result of unstable microcrack propagation. [28] This volume expansion effect is illustrated in Figure 3.3(b), with negative volumetric strains ε_v defining a volume expansion. Volume expansion of concrete in uniaxial compression could be described mathematically by a Poisson's ratio value of $\nu > 0.5$. Inhomogeneity of the concrete can lead to material points not reaching this stress state simultaneously, and the neighbouring concrete will exert a confining effect. This results in a triaxial compressive stress state in the critical material point and transverse tensile stresses in the surrounding concrete, and a *splitting* failure is initiated when the transverse tensile stresses exceeds the concrete tensile strength [29].

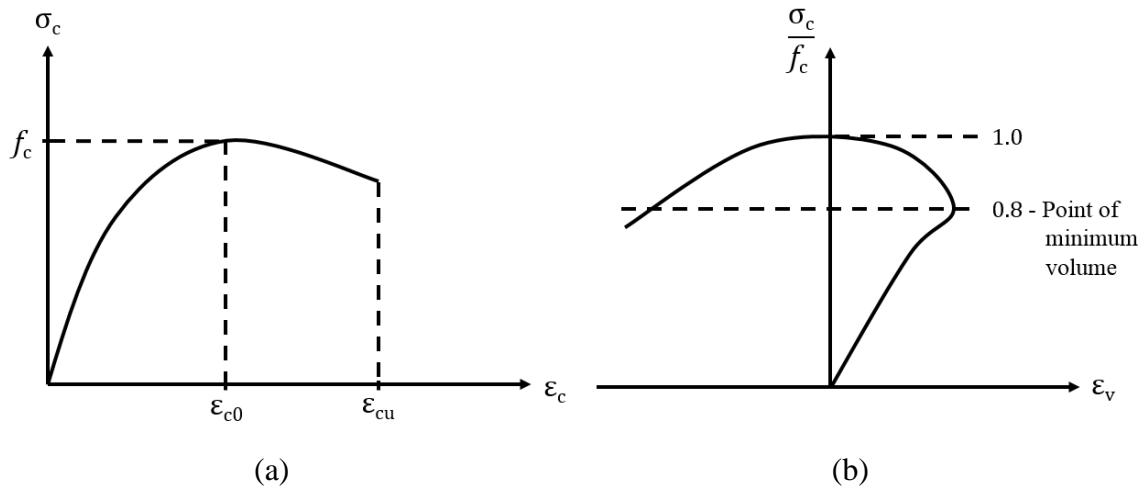


Figure 3.3: (a) General uniaxial compression curve and (b) illustration of volume expansion effect in concrete with ϵ_v volumetric strains. Figures based on [28].

The descending branch in Figure 3.3(a) describes a strain softening relation in compression, with decreasing stresses for increasing strains. The descending branch governs the crushing process in concrete, and the dependency to the compressive fracture energy G_C regularized on the equivalent length, or the crushing bandwidth, h_{eq} reduces the mesh sensitivity during localization of strains [8]. When concrete in compression exhibits strain softening, localization is expected with a damage zone where all further deformation occurs while the remaining structure unloads [15]. Several definitions of the descending branch is proposed in the literature, and the relevance discussed [17, 24]. *fib* states that the branch is highly dependent on the specimen geometry, the boundary conditions and the possibility for an internal load redistribution [17]. *fib* further states that the descending branch describes the behaviour of softening due to microcracking.

Size effect is a consequence of a strain localization, and the descending branch of the compressive curve is dependent on the specimen size, and hence not a pure material parameter [15]. Several sources claim the size dependency of the descending branch to the test specimen size the material parameters were extracted from [22, 30]. Hanjari proposed a modification of the compressive curve as illustrated in Figure 3.4(a) to correct the value G_C relative to the test specimen.

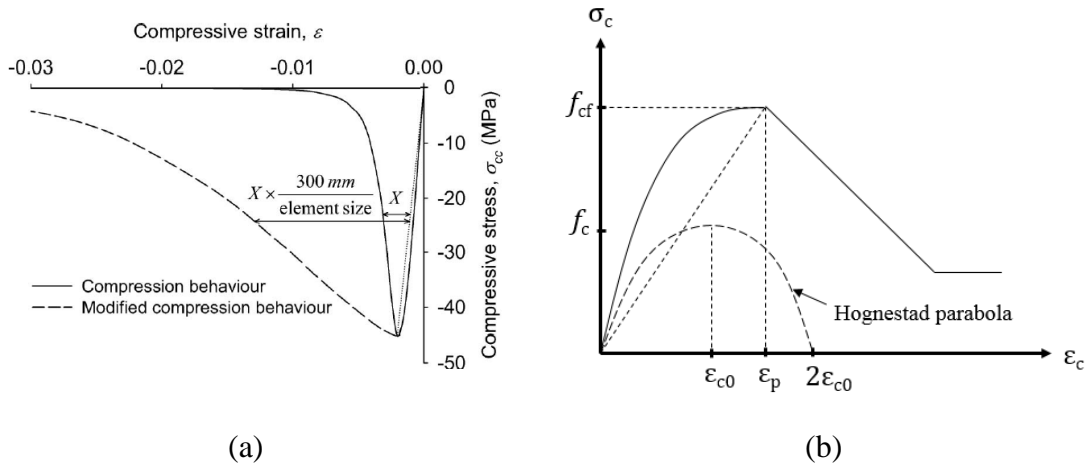


Figure 3.4: (a) Correction of softening compressive strains from a concrete test specimen size of 300 mm [30] and (b) confined concrete stress-strain relation by Vecchio, redrawn figure [31].

3.5 Multiaxial behaviour of concrete

The multiaxial stress state in concrete has proved to be an essential phenomenon to include for a realistic concrete material behaviour [25, 28, 32]. Compression softening refers to the reduction of compressive strength due to occurrence of large transverse tensile strains, creating cracks transverse to the compressive stress direction. Vecchio & Collins provide a model for this effect that utilizes a reduction factor β_{cr} for reduction of the peak stress and strain [25].

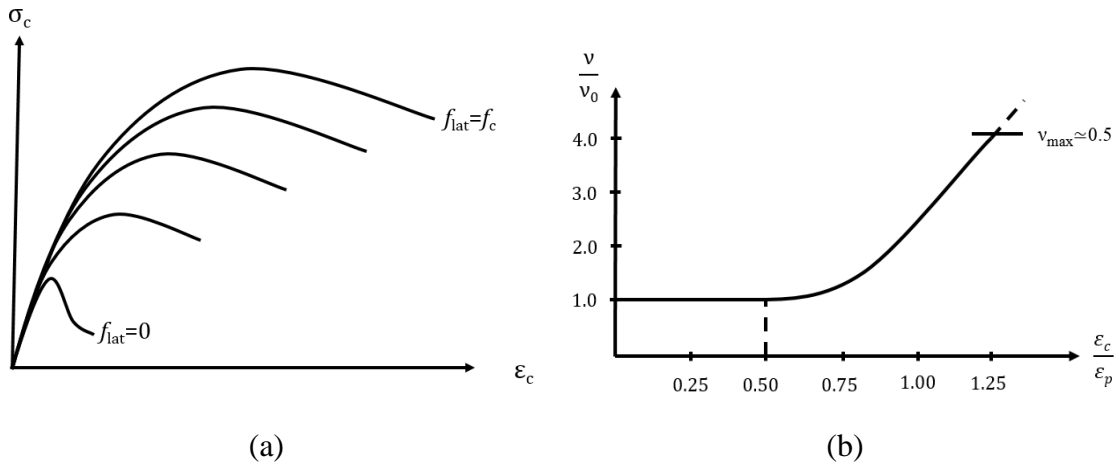


Figure 3.5: (a) Effect of lateral confinement on strength and ductility in plain concrete with f_{lat} the hydrostatic pressure and (b) increased Poisson's ratio for increasing concrete strains. Figures redrawn from [28, 31].

Lateral displacements perpendicular to the uniaxial compression or tension direction is governed by the Poisson's ratio, and referred to as the Poisson's effect. Under biaxial – or triaxial compression states, the lateral strains due to the Poisson's effect can be of great significance. Because of micro cracking for high compressive stresses, the lateral expansion increases for increasing compressive stresses. This equals a progressively increasing effective Poisson's ratio for large compressive strains, illustrated in Figure 3.5(b).

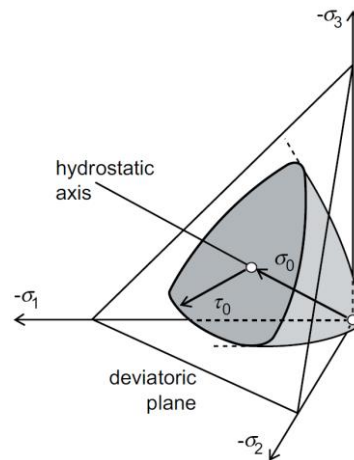


Figure 3.6: Three-dimensional concrete failure surface in deviatoric plane [6].

Concrete is a pressure-dependent material, where an increased hydrostatic stress will increase the concrete strength and ductility by preventing microcrack propagation. Selby and Vecchio early emphasized the importance of including this effect in analyses of reinforced concrete to model a realistic three-dimensional behaviour [28]. The three-dimensional failure surface in Figure 3.6 illustrates the increase in concrete strength for a confined concrete specimen. Vecchio used the constitutive relation illustrated in Figure 3.4(b) for confined concrete in a study on concrete expansion [31], increasing both the peak stress and strain and limiting the final degradation of the stress with a resulting ductile behaviour. Passive lateral confinement occurs when the concrete expansion is constrained due to boundary conditions, neighbouring concrete or reinforcement, or by a combination.

3.6 Reinforcement and interaction with concrete

Reinforcement steel may be assumed linear elastic up to an elasticity limit defined by the yield stress and – strain with equal properties in tension and compression. The stability of the analyses may be increased by including work hardening of the steel, which means an increase of strength by increasing strains defined by a hardening modulus E_{har} [8].

The bond between the concrete and the steel reinforcement makes reinforced concrete structures useful since the tensile loads are carried by the reinforcement. Bond cracking is a result from a relative displacement between the reinforcement and the concrete, referred to as bond slip, occurring for shear forces at the interface exceeding the bond strength and illustrated in Figure 3.7(a). Tension stiffening describes the fact that reinforced concrete in tension exerts a stiffer behaviour than a plain reinforcement bar alone. Stress distribution occurs at the crack localization along the reinforcement bar, where stresses are transferred from the cracked concrete to the reinforcement bar and back to the uncracked concrete between cracks, see Figure 3.7(b).

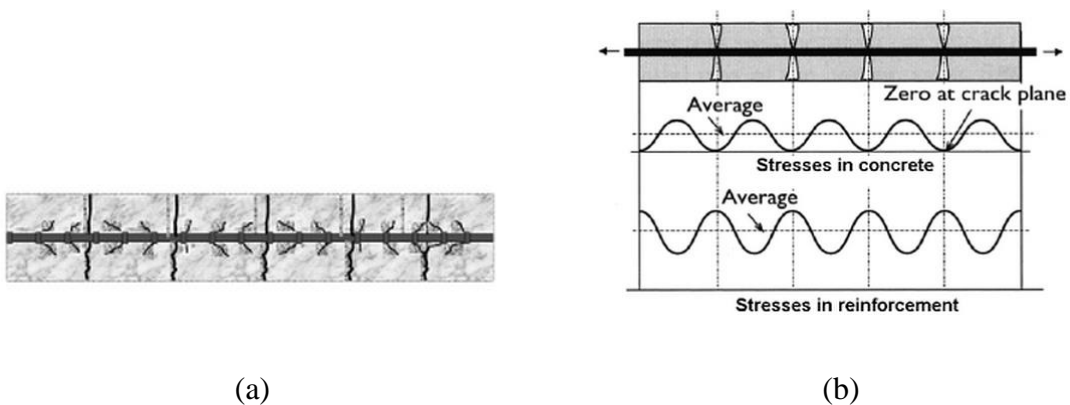


Figure 3.7: (a) Bond cracking at reinforcement steel bar and (b) illustration of tension stiffening effect [15]

PART II: SELECTION OF SOLUTION STRATEGY

4 Case study framework

Guidelines providing verified solution strategies that defines well-validated models could limit the resulting modelling uncertainty and hence increase the benefit of using NLFEA in design. *The Dutch guidelines* (DG) are validated for use on girders and partly for slabs, though a final validation for structural walls is not documented to date [8].

Buildings often include reinforced concrete structural walls for bracing against horizontal loads such as wind and earthquake, and for transferring vertical loads over multiple floors. Structural walls may carry mainly in-plane shear forces and axial loads, and similar structures are found in offshore gravity based substructures. These structures may be idealized as plane stress problems where the stresses normal to the wall thickness can be neglected. Two-dimensional finite element models will also reduce the complexity and the effectiveness in terms of numerical computational time. Large and existing structures are however likely to be modelled with solid elements in practice [5]. A solution strategy based in the recommendations in DG is used to define two *base models* with plane stress and solid brick elements respectively, further referred to as the 2D base model and the 3D base model. The main objective of the case study is to assess the ultimate load capacity of the structural wall and interpret the overall structural behaviour of the base models. This will serve as the foundation for making a justified selection of a final solution strategy for further use on structural walls in section 6.5, based on one of the two base models.

4.1 Experiment by Lefas et.al on reinforced concrete structural walls

A well-documented experiment executed by Lefas et.al on structural walls serves as reference case throughout the thesis [9]. The experiment is validated in subsequent studies, and several studies are later referring to this particular experiment [5, 28, 31]. Lefas et.al investigated strength, deformation characteristics and failure mechanisms in an extensive experimental test on 13 large-scale structural wall specimens subjected to monotonically increased horizontal load at the wall top edge [9]. Two types of walls with varying height to width ratio, reinforcement ratio, concrete strengths and additional axial load level were tested until failure[9].

4.1.1 Results from experimental study

The wall specimen SW21 with height to width ratio two without additional axial loading is studied in the case study. Geometry, reinforcement layout and experimental setup is presented in Figure 4.2. The tested wall specimens failed in a ductile mode, and collapsed due to failure of the compressive zone by vertical crack propagation, after a significant reduction of the compressive zone depth. Yielding of the vertical reinforcement initiated at about 40% of the failure load level. A main conclusion from the experiment was that the high load capacity of the structural walls was connected to the triaxial compressive stress condition occurring in the compressive zone, due to a combination of large compressive and shear forces. Volume dilatation of the concrete in critical compressive regions was identified as a main contributor to the triaxial compressive stress state. The failure mechanism of the wall specimens is illustrated in Figure 4.1.

4.1.2 Previous studies

Vecchio analysed all the wall specimens numerically with good correlation between NLFEA and experimental results, though the expansion effects in the concrete was designated as critical for reproducing the high load capacity [31]. Selby and Vecchio further confirmed this in a larger study that comprised the modified compression field theory developed for cracked reinforced concrete panels [28]. Jonas Stene Pettersen the spring semester 2014 wrote a master's thesis at NTNU on the same wall specimen, with aim to assess the influence of large finite plane stress element sizes to the ultimate load capacity prediction [32]. A low load capacity prediction was observed, and the lack of volumetric expansion modelling in DIANA was indicated as a main source of error.

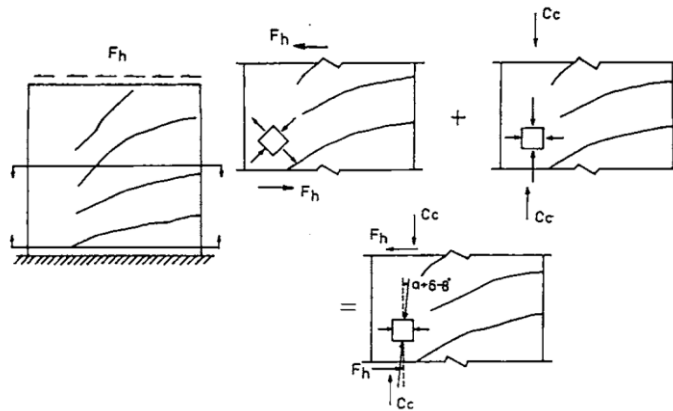


Figure 4.1: Illustration of failure mechanism in all the wall specimens [9].

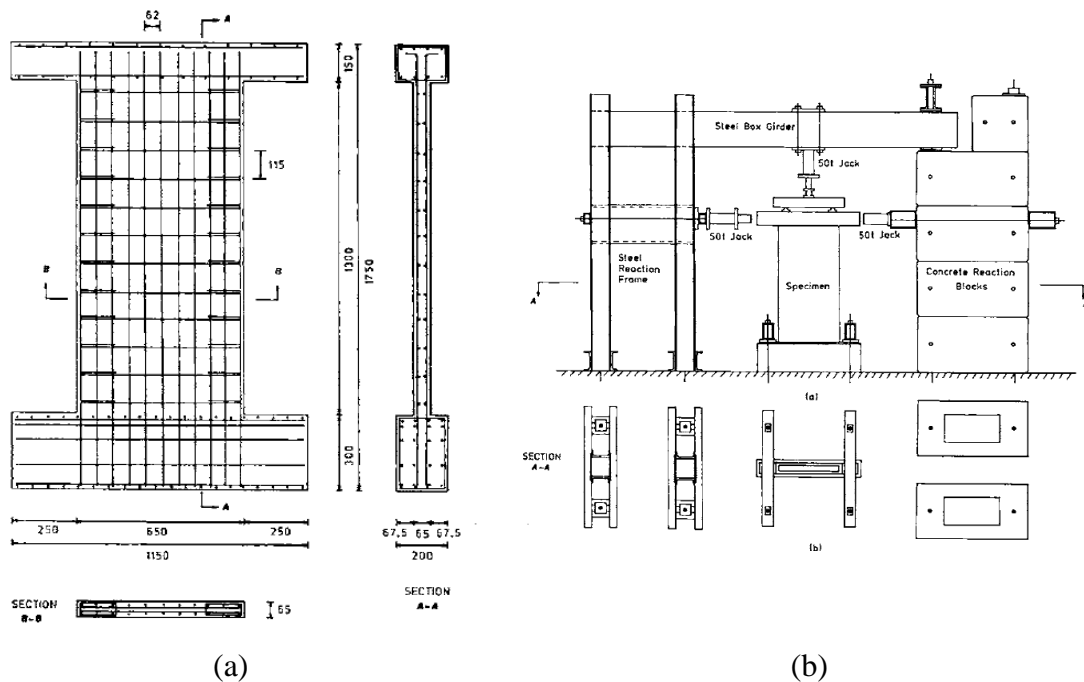


Figure 4.2: (a) Geometry and reinforcement details of Type II wall specimen and (b) representation of the test rig for the wall specimens, elevation – and plan view [9].

4.2 Solution strategy based on *the Dutch guidelines* (DG)

The recommendations provided by *the Dutch guidelines* (DG) were used to define a solution strategy for two base models, where the main differences are the finite element type and the geometrical modelling of the upper beam. See appendix F for a representative input data file and analysis command file.

The displacement based finite element method using the FEA software DIANA, version 9.6, is used in all the finite element analyses. The software provides complex uniaxial material models that can be implemented into finite element models using basic material parameters, and advanced solution procedures for nonlinear finite element analyses [33].

4.2.1 Preliminary analyses

To verify the finite element model regarding units, validate the models elastic stiffness and select suitable, though rather coarse, finite element sizes, reference analytical calculations were performed and compared with static linear finite element analyses (LFEA). The analytical calculations and complete LFEA results are presented in Appendix A. Table 4.1

summarizes the most relevant results from the preliminary analyses, indicating small deviations of $\pm 0.5\%$ for the selected finite element sizes of 130 mm, see section 4.2.2.

Table 4.1: LFEA on simplified FE-model of the wall specimen, δ_A displacement from analytical calculation.

	Global finite element size [mm]	$\delta_{\text{LFEA}} / \delta_A$
	65*65	1.0060
Plane stress elements	130*130	1.0047
	325*325	0.9975
	65*65*65	0.9960
Solid brick elements	130*130*65	0.9949
	325*325*65	0.9886

4.2.2 Finite element discretization

The finite element method approximates the physical structural problem by division into a number of elements of finite size. The quality of the predicted structural response will depend on the selections made on size, shape, interpolation degree and numerical integration scheme of the finite elements.

Finite element size scale

Rather large finite elements might be required for less expensive and more efficient analyses in a design procedure. Interaction properties to the reinforcement are often coupled to the finite element sizes [15]. Present literature does not provide a clear finite element size scale. A combination of the definition by Lackner and Mang [34] and the *fib* Bulletin 45 [15] was used to assess the relative finite element size, together with recommendations on a maximum finite element size in DG. The *member* scale in Figure 4.3(c) is interpreted as analogous to the *large* scale in *fib* Bulletin 45. DG provide a recommendation of an upper limit of the finite element size to avoid a snap-back in the stress-strain relationship and to avoid extreme jumps in the stress field among the elements that can lead to inaccurate results [8]. The criterion for maximum element size depend on the concretes modulus of elasticity, fracture energy and tensile strength presented in Table 4.2, and resulted in an approximate maximum element side length of $l_{e,\text{max}} \approx 135$ mm.

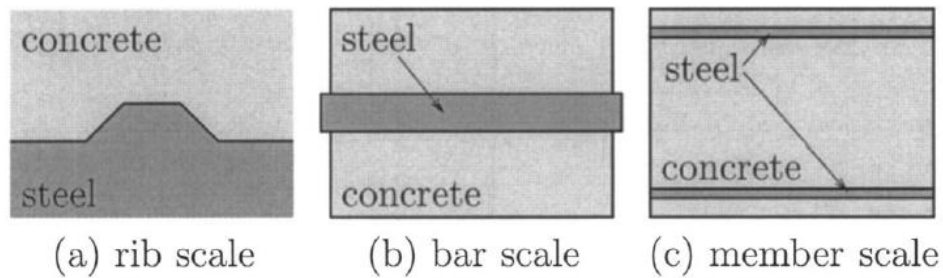


Figure 4.3: Finite element size scale according to Lackner and Mang [34].

Concrete

The finite element size was chosen based on the preference of quite large elements for an effective analysis procedure within limits of good accuracy. Both base models utilize quadratic finite elements of 130×130 mm, with one element over the wall thickness for the solid elements referring to the highlighted values in Table 4.1. This finite element size is within the member scale and thus large scale in *fib* Bulletin 45, and also within the recommended maximum finite element side length criterion $l_{e,max}$ in DG [8].

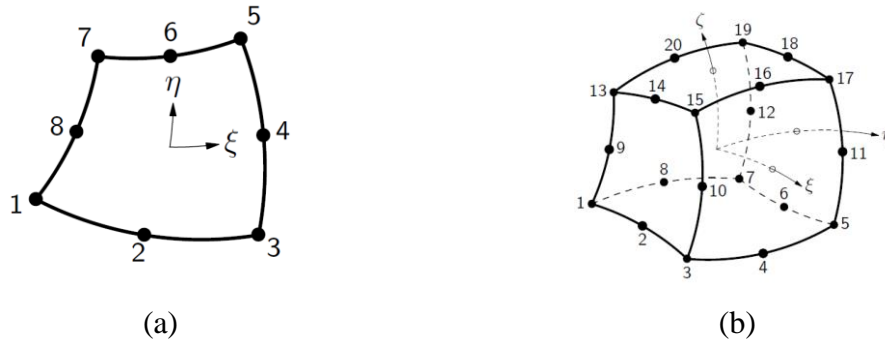


Figure 4.4: (a) Plane stress element CQ16M and (b) solid brick element CHX60 [35].

DG suggest quadrilateral elements in 2D and hexahedral elements in 3D based on quadratic interpolation of the displacement field, which implies a linear distribution of stresses and strains along the element edges [8]. Quadrilateral 8-node isoparametric plane stress elements CQ16M and twenty-node isoparametric solid brick elements CHX60 was used in the 2D and 3D base model respectively, illustrated in Figure 4.4. Use of these elements on the structural wall generates no distorted elements.

Reinforcement

The reinforcement was implemented as straight embedded reinforcement bars with no own degrees of freedom and perfect bond. Perfect bond is recommended by *fib* for large scale elements, and is also considered sufficient by DG [8, 15]. Due to the assumed perfect bond, the strains in the reinforcement are calculated on basis of the displacement field in the concrete elements.

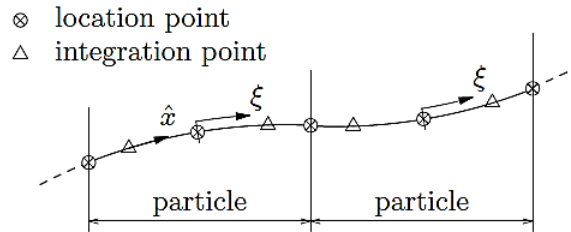


Figure 4.5: Topology of embedded reinforcement bar elements [35].

Numerical integration

Reduced integration of the concrete elements may result in spurious modes at prominent cracking, this was bypassed by using a full Gaussian integration scheme on the concrete elements [8]. Since the reinforcement bars were embedded in the concrete elements, it was sufficient to utilize reduced integration of the reinforcement bars as illustrated in Figure 4.6. The total bar length is automatically divided into particles within the concrete elements, and DIANA performs numerical integration within each particle, see Figure 4.5.

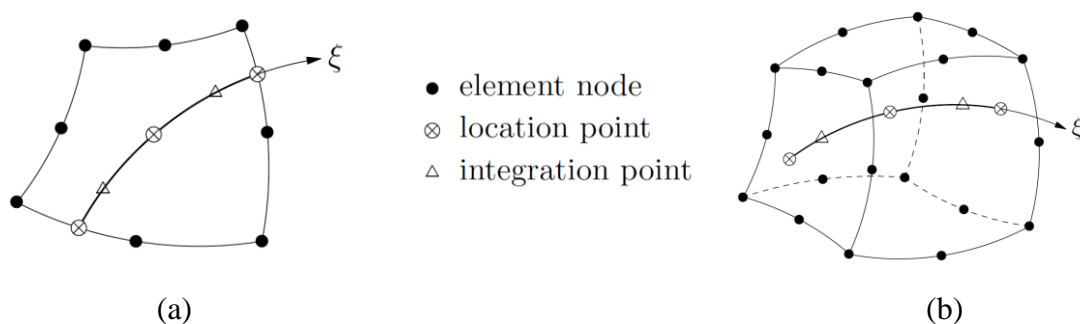


Figure 4.6: Reinforcement embedded bar element implementation to (a) plane stress element and (b) solid brick element [35].

4.2.3 Geometry, boundary constraints and loading

Several model generations of the structural wall geometry were modelled to assess the influence of the boundary conditions on the predicted ultimate load capacity. For load

transfer and foundation of the wall on the experiment, a lower beam and upper beam was present referring to Figure 4.2(a). The beams did not need to serve as reinforcement anchorage in the finite element model due to use of perfect bond. The upper beam was in the experiment heavily reinforced and with a thickness more than three times the wall thickness [9], and was thus chosen to be modelled as linear elastic concrete, to serve only as load transfer in both the base models and to avoid local damage at the concentrated load. A study of the influence of the lower beam effect was performed, results are enclosed in Appendix B. The study indicated that the lower beam was of little significance for the global structural response, and the presented boundary conditions were interpreted as sufficient without inclusion of the lower beam. This also generalizes the base models to other cases of structural walls, where the load bearing area outside the structure may be unknown or difficult to define. The fixed support of the wall was induced by restraining all nodal displacements along the wall base. The horizontal load F_H was applied as an equivalent displacement, as a single nodal displacement in the 2D base model and as a uniform distributed displacement in three nodes over the thickness of the elements in the 3D base model. The reinforcement layout was provided by Figure 4.2(a) from the experimental report [9].

2D base model

The 2D base model included a fully reinforced and cantilevered upper beam, with linear elastic concrete to avoid damage of the upper beam due to the concentrated load. See Figure 4.7 for geometry, loading and boundary conditions.

3D base model

The transition into a three-dimensional model generated some simplifications of the upper beam geometry, which proved to have no significant effect on the global structural response. The upper beam was given the same width as the wall, with no inclusion of horizontal or shear reinforcement due to the linear elastic concrete. The reinforcement layout is equal as for the 2D base model, though with the additional transverse part of the shear stirrups and exact spacing of the reinforcement bars in-plane, see Figure 4.8.

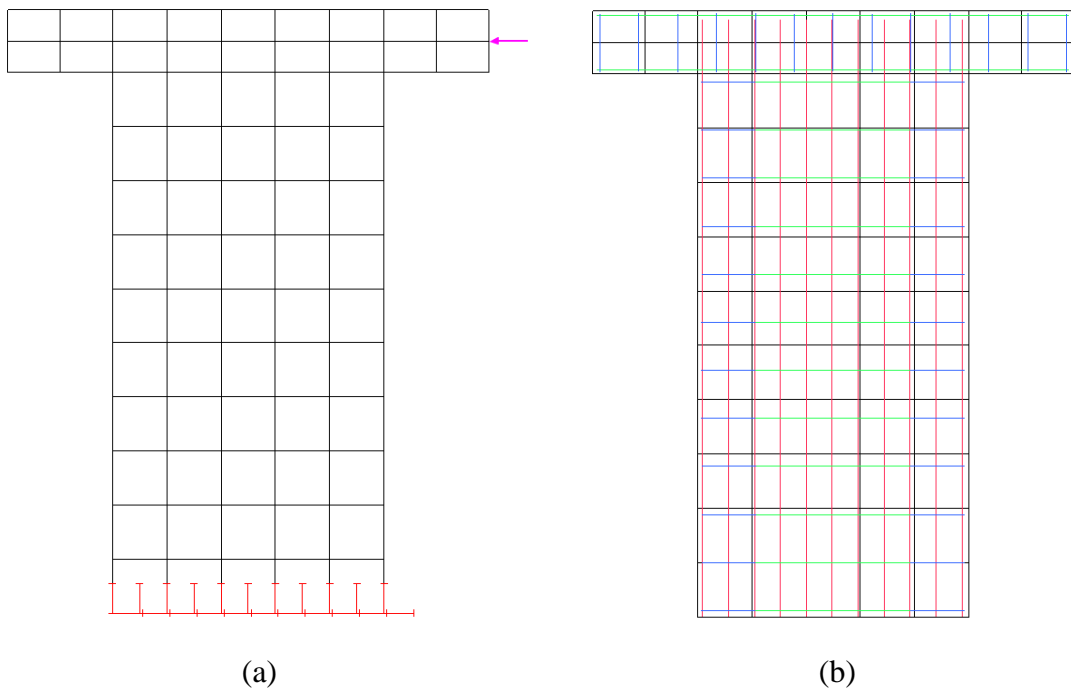


Figure 4.7: (a) Mesh, boundary constraints and loading and (b) all reinforcement in the 2D base model.

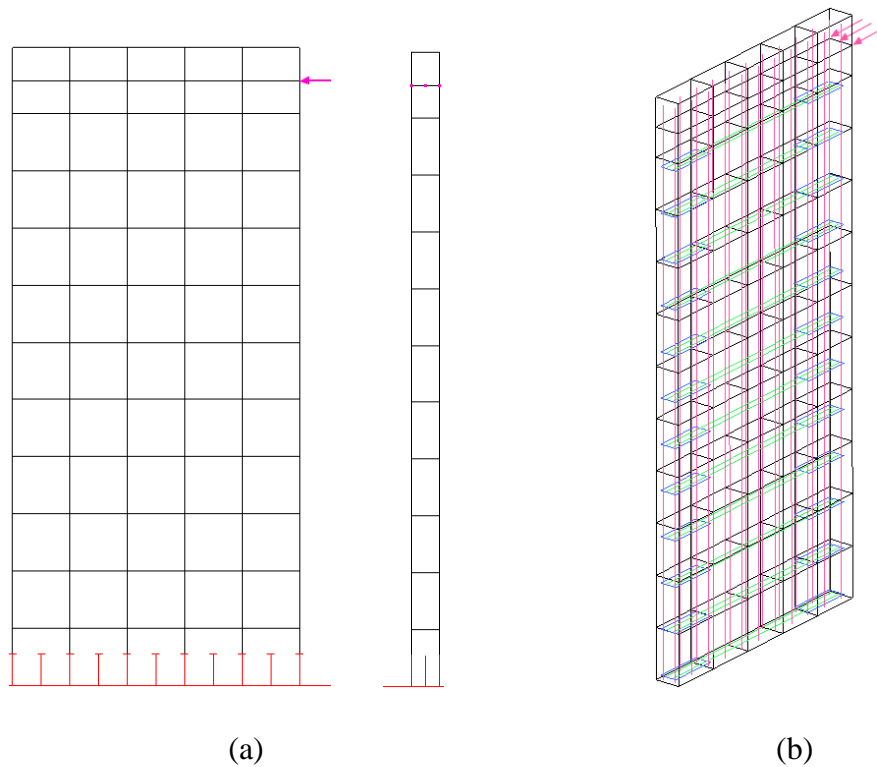


Figure 4.8: (a) Mesh, boundary constraints and loading and (b) all reinforcement in the 3D base model.

4.2.4 Numerical material modelling in DIANA

All the constitutive models and material parameter calculations presented in this section are proposed by DG is else is not specified.

Constitutive modelling

DIANA provides constitutive models based on uniaxial concrete behaviour, with extensions for inclusion of multiaxial effects [24]. DG recommends specific constitutive models for reinforced concrete structures, also for three-dimensional finite element modelling. Only mode I fracture energy regarding energy dissipated by crack opening is treated, hence $G_F^I = G_F$.

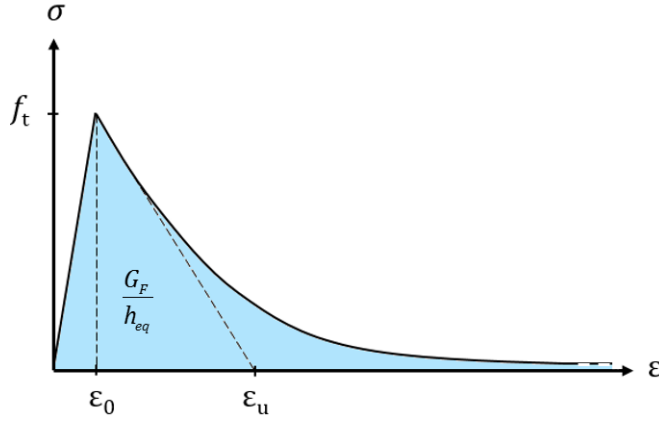
Concrete crack model and shear behaviour

A total strain based fixed crack model was used in all the analyses, with a constant shear retention factor (SRF) of 0.1 for realistic stress transfer after cracking and numerical stability [5, 27]. This value implies that ten percent of the shear stiffness retains in the cracked concrete. DG suggest a variable SRF, though the variable shear retention models in DIANA requires manual input of unknown values of shear stress and strain limits [24]. The alternative damage based shear retention factor provided by DIANA resulted in severe post-peak convergence problems and a more brittle failure in early analyses. A rotating crack model resulted in a similar convergence problem. An orthogonal crack models implies two or three orthogonal cracks at each integration point in two and three-dimensional finite elements respectively. For total strain based crack models, DIANA by default determines the equivalent length, or the crack bandwidth, h_{eq} to reduce mesh size dependency, with default values \sqrt{A} for quadratic plane stress elements and $\sqrt[3]{V}$ for solid brick elements [24]. Poisson's ratio was kept constant at $\nu=0.15$ until initiation of cracking, with following reduction at the same rate as the secant modulus.

Concrete tensile response

Concrete tensile behaviour was modelled as linear elastic until the tensile strength is reached and cracking initiated. Following, a softening branch with exponential shape, defined by ϵ_u , and dependency to the fracture energy G_F regularized on the crack bandwidth h_{eq} was used to reduce mesh sensitivity, illustrated in Figure 4.9. The tension softening branch allows for bridging stresses in cracked concrete and provides more localized cracks.

For all linear elastic concrete behaviour, a reduced Young's modulus E_c by a factor of 0.85 accounted for initial cracking.



$$\varepsilon_0 = \frac{f_t}{E_c} \quad (4.1)$$

$$\varepsilon_u = \frac{G_F}{h_{eq} f_t} \quad (4.2)$$

$$\sigma = f_t e^{\left(\frac{-(\varepsilon - \varepsilon_0)}{\varepsilon_u}\right)} \quad (4.3)$$

Figure 4.9: Uniaxial concrete tensile stress-strain behaviour with exponential softening. Formula for σ in [8]. Redrawn figure from [24].

Concrete compressive response

A parabolic curve with a descending branch is recommended by DG. DIANA provides a parabolic curve that reduces the concrete compressive strength to zero at an ultimate strain α_u illustrated in Figure 4.10(a). The compressive fracture energy G_C governs the descending branch of the compressive curve only, see formula 4.4 from the DIANA 9.6 material library [24]. The descending branch in the parabolic curve differs from the compression curve suggested by *fib* Bulletin 70, where the branch is limited to a maximum of ultimate strain of $\varepsilon_u=0.35\%$ at a reasonably high stress level [17].

$$\int_{\alpha_c}^{\alpha_u} f d\alpha_j = \left[f_c \left(\alpha_j - \frac{1}{3} \left(\frac{\alpha_j - \alpha_c}{\alpha_u - \alpha_c} \right)^3 \right) \right]_{\alpha_c}^{\alpha_u} = \frac{G_C}{h_{eq}} \quad (4.4)$$

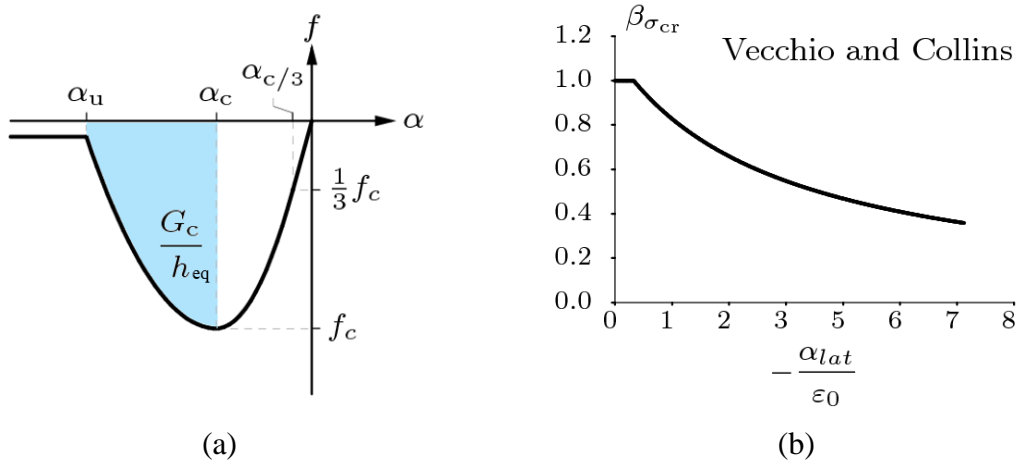


Figure 4.10: (a) Uniaxial concrete compressive stress-strain behaviour and (b) reduction factor of compressive strength due to lateral cracking [24].

Concrete multiaxial response

The multiaxial behaviour of concrete is in DIANA provided by extensions for increasing the compressive strength and strain by confinement effects, and decreasing the compressive strength due to lateral cracking. DG state that the increase of strength and ductility due to confining lateral stresses is conservative no neglect. Referring to previous studies of the wall specimen [31, 32], confinement effects were included with a model proposed by Selby & Vecchio, which defines the peak stress factor $K_{\sigma} = f_{cf}/f_c$ and an assumed peak strain factor $K_{\epsilon} = K_{\sigma}$ [24]. The increase of strength is in DIANA governed by the Hsieh-Ting-Chen failure surface defined on stress invariants, principal stresses and the confined concrete compressive strength [24].

Reduction of the concrete compressive strength occurs due to lateral cracking, and was implemented with a model proposed by Vecchio and Collins illustrated in Figure 4.10(b), and limited by maximum reduction factor $\beta_{\sigma_{cr}} = 0.4$. This model only reduces the strength, that implies a constant $\beta_{\sigma_{cr}} = 1.0$ for the strains. DIANA 9.6 does not provide a model for explicit modelling of concrete volumetric expansion.

Reinforcement behaviour and interaction with concrete

A bilinear stress-strain diagram was used for the reinforcement steel presented, in Figure 4.11(a) with a nominal hardening modulus $E_{har} = 0.02E_s$ due to lack of ultimate strain ϵ_{su} information. Equivalent behaviour in tension and compression was assumed. Perfect bond

between the concrete and the reinforcement was used, as considered sufficient accurate by DG and by *fib* for large finite elements [8, 15].

Redistribution of tensile stresses from the concrete cracks to the reinforcement bars and back to the concrete between cracks is referred to as tension stiffening. DG suggest that if the average crack spacing l_{av} in the concrete is smaller than the crack bandwidth h_{eq} , the fracture energy G_F should be increased by a factor n_{cr} to allow for several cracks within the element [8]. Else, the tension softening relation based on the unmodified tensile fracture energy G_F can be used. The finite element mesh used was rather coarse, and the average crack spacing needed to be calculated in order to decide whether an increase of the fracture energy was necessary. Formulas in *fib* Model Code 2010 and the course literature in Concrete Structures 3 at NTNU were used in the crack spacing calculations [1, 36]. The first reference assumes cracks by pure tension in the element, resulting in cracks orthogonal to the reinforcement [1]. DG states that a directional average should be used if crack development in a significant angle to the reinforcement is expected. Inclined cracks were expected, and the latter reference provides alternative methods for other stress states by including the crack angle between the vertical reinforcement and the principal tensile direction. The method in *fib* Model Code 2010 in formula 4.5 with the values $k=1$, $\tau_{bms}=1.8f_t$ for short term loading was used to calculate $s_{r,max,x}$ and $s_{r,max,y}$ [1]. The index i refer to the reinforcement direction x and y , and the effective concrete area was calculated as a wall in tension.

$$s_{r,max,i} = 2 \left(kc_i + \frac{1}{4} \frac{f_t}{\tau_{bms}} \frac{\varphi_{si}}{\rho_{s,ef,i}} \right) \quad (4.5)$$

The two alternative methods for calculating the crack angle depend only to the reinforcement ratios. A conservative simplification of pure shear loading with $N_x=N_y=0$ of the walls was used. Alternative 2 in formula 4.6 assumes yielding of the reinforcement in both directions, while alternative 3 in formula 4.7 assumes linear elastic reinforcement and concrete in compression, and no tensile strength of the concrete. The alternative methods resulted in significantly lower crack spacing values than the method of maximum crack spacing in *fib* Model Code 2010, providing a conservative approach. The index j refer to alternative 2 and 3.

$$\text{Alternative 2} \quad \tan^2 \theta_2 + \left(\frac{N_x}{N_{xy}} - \frac{N_y}{N_{xy}} \frac{A_{sx}}{A_{sy}} \right) \tan \theta - \frac{A_{sx}}{A_{sy}} = 0 \quad (4.6)$$

$$\text{Alternative 3} \quad \tan^4 \theta_3 + \frac{N_x}{N_{xy}} \tan^3 \theta - \frac{N_y}{N_{xy}} \frac{A_{sx}}{A_{sy}} \tan \theta - \frac{A_{sx}}{A_{sy}} = 0 \quad (4.7)$$

$$\text{Directional average} \quad s_{\theta_j} = \frac{1}{\frac{\cos \theta_j}{s_{r,\max,y}} + \frac{\sin \theta_j}{s_{r,\max,x}}} \quad (4.8)$$

Detailed calculations and definitions are presented in Appendix C. The modification factor n_{cr} and modified fracture energy G_F^{RC} are defined below [8].

$$n_{cr} = \max \left(1, \frac{h_{eq}}{l_{av}} \right) \quad (4.9)$$

$$G_F^{RC} = n_{cr} G_F \quad (4.10)$$

The average crack spacing was calculated as the average of the results from the two alternative methods of calculation, with resulting $l_{av}=86.7$ mm. Based on this, tension stiffening was taken into account according to the procedure described in DG by formula 4.9 and 4.10. It was found that this had a limited effect on the global capacity, 0.8% and 0.9% for SW21 in 2D and 3D respectively, and later 0.2% for SW11 in 3D, and was not used further in this project. All the presented results in this thesis are thus calculated with the unmodified tensile fracture energy G_F as presented in Table 4.2, and interaction between reinforcement and concrete was accounted for by the tension softening branch as suggested by DG [8].

Material parameters

For a realistic structural response true, or mean, material parameters are used [1, 8]

Concrete material parameters

All the concrete material parameters were calculated on basis of the mean concrete compressive cylinder strength f_{cm} . The concrete cube strength f_{cu} was given in the experimental report, and the transition to mean cylinder strength was given by the

4 CASE STUDY FRAMEWORK

simplification $f_{cm}=f_c'=0.85f_{cu}$ [9]. The calculated mean concrete material parameters for SW21 are presented in Table 4.2. The method of estimating the fracture energy G_F in DG depends on the maximum aggregate size d_{max} , which was assumed equal to 16 mm considering the relativeness to the physical thickness of the wall and the given information of used aggregate size of 10 mm in all the wall specimens [9]. DG state that the formula for G_F in *fib* Model Code 2010 may provide higher values, and recommends a conservative approach if the parameter effects are not further studied [8]. The definition in DG proved conservative compared to the definition in *fib* Model Code 2010, and was used in this thesis.

Table 4.2: Mean concrete material parameters for SW21 by DG [8, 9].

Concrete material parameter	Expression in DG	Value	Unit
Mean compressive strength f_{cm}	-	36.38	MPa
Characteristic compressive strength f_{ck}	$f_{ck} = f_{cm} - \Delta f$	28.38	MPa
Mean tensile strength f_{ctm}	$f_{ctm} = f_{ct0,m} \left(\frac{f_{ck}}{f_{ck0}} \right)^{\frac{2}{3}}$	2.81	MPa
Fracture energy G_F	$G_F = G_{F0} \left(\frac{f_{cm}}{f_{cm0}} \right)^{0.7}$	0.0741	Nmm/mm ²
Compressive fracture energy G_C	$G_C = 250G_F$	18.52	Nmm/mm ²
Young's modulus after 28 days	$E_{ci} = E_{c0} \left(\frac{f_{cm}}{f_{cm0}} \right)^{\frac{1}{3}}$	33 836	MPa
Reduced Young's modulus E_C	$E_C = 0.85E_{ci}$	28 761	MPa
Poisson's ratio ν	-	0.15	-

With constant parameters:

$$\Delta f = 8MPa$$

$$f_{ck0} = f_{cm0} = 10MPa$$

$$f_{ck0,m} = 1.4MPa$$

$$G_{F0} = 0.030Nmm / mm^2 \quad \text{for } d_{max}=16 \text{ mm}$$

$$E_{c0} = 22000MPa$$

Reinforcement steel material parameters

Three different reinforcement bar diameters with varying steel properties were used in the experiment. Mean values of the yield strength f_{ym} was used, see Table 4.3. Young's modulus for the reinforcement steel $E_s=200\ 000\ \text{MPa}$ was used and due to no information regarding ultimate strain ϵ_{su} for the reinforcement, the suggestion by DG of a nominal value $E_{har}=0.02E_s$ was used with a large value for the equivalent plastic strain p . An additional control of the most critical reinforcement stress level towards the ultimate strength f_{uk} was performed at the ultimate load level. h_R is calculated by a formula in [37].

Table 4.3: Reinforcement steel material parameters [8, 9].

Reinforcement bar diameter [mm]	Mean yield strength [MPa] $f_{ym} = f_{yk} + 10\text{MPa}$	Ultimate strength [MPa] f_{uk}
4	430	490
6.25	530	610
8	480	565

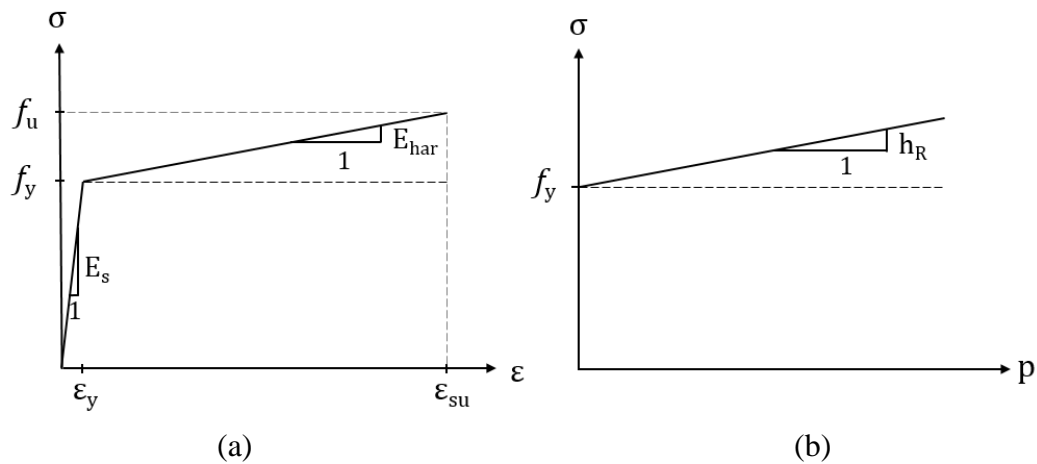


Figure 4.11: Reinforcement steel stress-strain diagram, same properties in tension and compression. Defined on (a) total strains and (b) equivalent plastic strains.

$$E_{har} = 0.02E_s = 4000\text{MPa}$$

$$h_R = \frac{E_{har}E_s}{E_s - E_{har}} = 4082\text{MPa}$$

4.2.5 Solution procedure

Load incrementation

The horizontal load F_H was applied indirectly with displacement control for a stable research approach [8]. Displacement control also allows for proceeding beyond initial peaks without use of arc-length method as illustrated in Figure 4.12. Explicit load steps were preferable in this study for better comparison and control of the structural response, though DG suggests the use of an automatic load incrementation and an arc-length procedure to ensure stability. The load steps were explicitly defined with initial steps about a third of the displacement value that initiated flexural cracking. The loading sequence comprised five initial load steps of 0.1 mm, with following step sizes of 0.5 mm until failure. This loading sequence lead to reaching the peak load and failure within 20-30 load steps, which is desirable for an efficient use of NLFEA by reducing the analysis time [5].

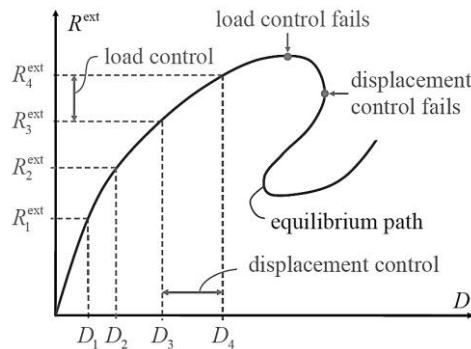


Figure 4.12: Displacement control scheme [38].

Equilibrium iteration

A standard Newton-Raphson solution procedure with line searches was used in all the analyses, for a stable and robust solution procedure. Line searches are especially effective for problems where the stiffness of the structure undergo rapid stiffness changes, e.g. caused by cracking and yielding in reinforced concrete [39]. A number of ten line searches during each iteration, and a maximum of 50 iterations within each increment, was set to limit the CPU-time and hence requiring an effective solution procedure. The default solver of in DIANA, Parallel Direct Sparse, solved the system of equilibrium equations [40].

Convergence criteria

Convergence criteria on both force-norm and energy-norm with tolerances of respectively 10^{-2} and 10^{-3} was used, though allowing the analysis to proceed beyond non-converged load steps as this does not necessarily imply failure. The non-converged load steps were evaluated in the post-processing procedure. DG suggest an energy-norm of 10^{-4} , though this lead to some difficulties obtaining convergence in the pre-peak region. The non-converged load steps indicated to be mainly due to the solution procedure and not due to failure, and a less restrictive energy-norm of 10^{-3} was used in agreement with analyses performed by Engen [5].

5 NLFEA results from the case study

The two preliminary solution strategies are defined in section 4.2, comprising the two *base models*. The following sections presents the results of the two base models with a supporting sensitivity study on mesh sensitivity and critical effects regarding the constitutive modelling. The main objective is to predict the ultimate load capacity R_{um} . Lefas et.al reported an ultimate load capacity $R_{exp}=127.0$ kN at 20.61 mm displacement for the wall specimen SW21 [9].

Results presentation

All the experimental results presented in load-displacement and secant stiffness plots are interpreted by best mean from curves provided in the experimental report, and may not be considered exact. For contour plots of tensile concrete strains the colour ranges presented in Figure 5.1 are used, with mean concrete tensile strength $f_t=f_{ctm}$. Compressive stresses – and strains are defined as negative.

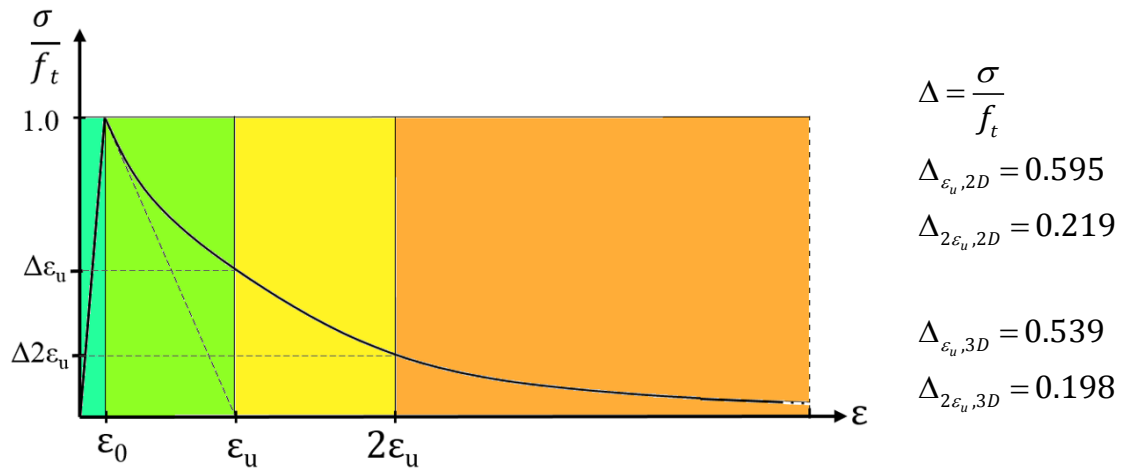


Figure 5.1: Colour contour ranges defining the concrete tensile strains with corresponding stress ratios at the tensile strain limits for the two base models [8].

5.1 Results from the base models

The total load-displacement response of the two base models, until reaching the reinforcement ultimate strength f_{uk} , is presented in Figure 5.2, and the non-converged load steps (LS) are marked. Convergence recovers and the load again increases, concurrently with a spurious increase of stresses visible by crudely exceeding the tensile strength. The

failure is thus defined at initial peak load, further justified in section 5.1.2. The failure of the reinforcement in the last presented post-peak load step in Figure 5.2 is thus not relevant. All the following results are until the first non-converged load step if else is not specified. The solution procedure is stable, with convergence in all pre-peak load steps for both the base models. The 3D base model converges within an average of 5.4 and maximum of 14 iterations, while the same for the 2D base model is 11.6 and 44 iterations.

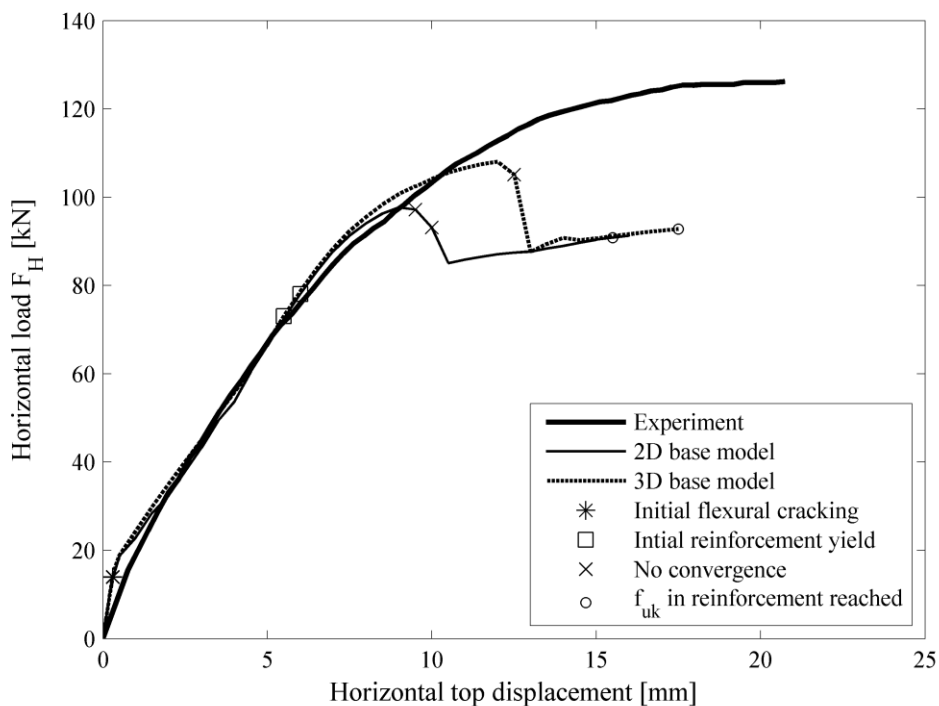


Figure 5.2: Total load-displacement response for the two base models.

The predicted ultimate load capacities:

- 2D base model: $R_{um}=97.7$ kN at LS 22 and 9 mm displacement. 76.9% of R_{exp} .
- 3D base model: $R_{um}=108.0$ kN at LS 28 and 12 mm displacement. 85.0 % of R_{exp} .

5.1.1 Concrete cracking and reinforcement yielding

The base models initiate flexural cracking at 0.3 mm displacement and 13.9 kN, see Figure 5.5(a) and Figure 5.6(a). The experimental values were respectively 0.32 mm and 10 kN. The propagating crack pattern during loading is presented in Figure 5.5 and Figure 5.6, resulting in vertical crack propagation in the compressive zone at peak load level, initiating

a splitting failure. The illustrated crack propagation during loading is in good compliance with the reported sequence by Lefas et.al. Initial yielding of the tensile reinforcement occurs at 6.0 mm displacement and 78.0 kN for the 2D base model, while at 5.5 mm and 73.1 kN for the 3D base model. In the experiment, this was observed at 5.81 mm displacement and 80 kN. The horizontal web reinforcement and the shear stirrups do not approach their yield limit prior to failure, this agrees well with the experiment. Figure 5.3 illustrates the stress envelope in the two most critical vertical reinforcement bars in tension and compression respectively.

5.1.2 Global failure

Justification of the initial peak load as point of global failure is supported by the following observations:

- The drop post-peak observed in the global response, followed by non-converged load steps and a spurious increases in stress, see Figure 5.2 and Figure 5.7.
- A large rotation of the principal stress field, a shift of the critical compressive zone location and a vertical crack propagation in the compressive zone at or directly after peak load level. See Figure 5.5, Figure 5.6, Figure 5.9 and Figure 5.10.

A splitting failure visible directly after peak load implies a failure mode similar as reported from the experiment. The compressive zone localizes within the outer base element at the compressive edge prior to failure, illustrated in Figure 5.10. A very small compressive zone at failure was also reported from the experiment. Figure 5.7 visualizes the gradually increasing shear stress level and with a re-localisation of the critical stress zone after the peak load level.

5.1.3 Stiffness

The secant stiffness change during loading presented in Figure 5.4 can serve as measure of the structural stiffness change during loading, estimated as the load F_H over the top horizontal displacement in each load step. A poor prediction of the stiffness at low load levels is observed. Nonlinearities such as progressive cracking and yielding of the reinforcement decreases the initial stiffness, and the horizontal initial region illustrates the linear elastic concrete behaviour before cracking with no stiffness reduction.

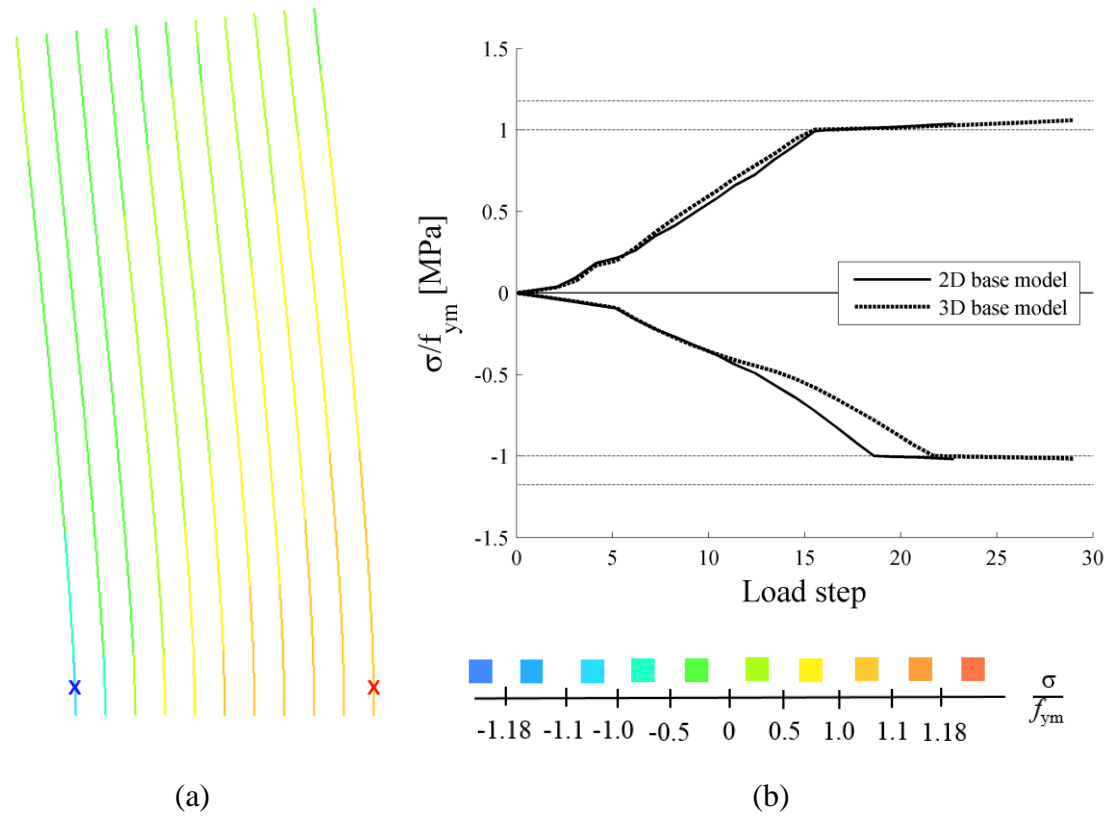


Figure 5.3: Gaussian stress in vertical reinforcement, max/min value in element. (a) Contour plot at peak load level in 3D base model, deformation factor 10. (b) Stress in bar elements x during loading. Ultimate strength marked at $1.18 \sigma/f_{ym}$.

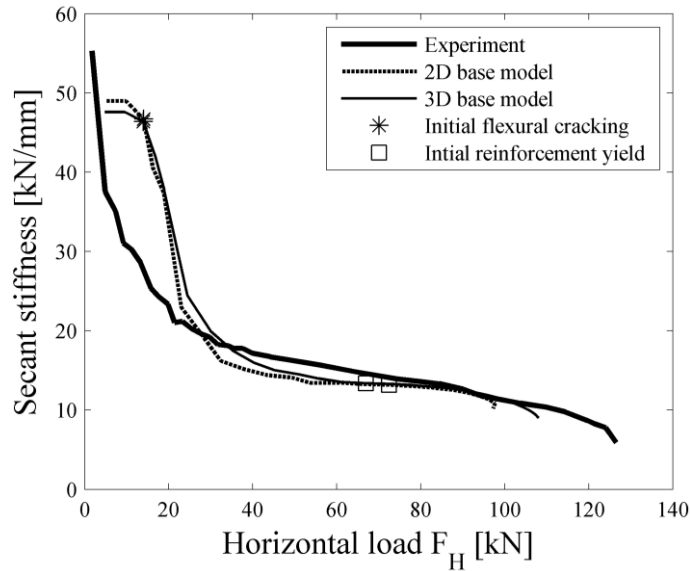
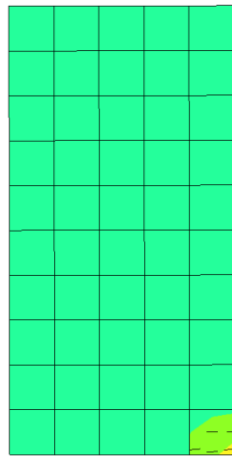
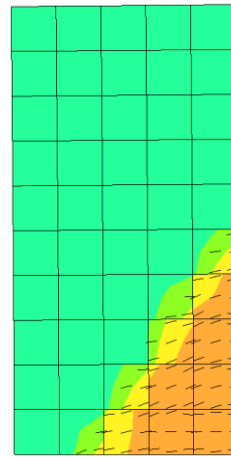


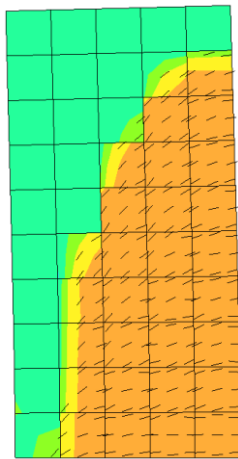
Figure 5.4: Secant stiffness to horizontal load level of both base models. Initial flexural cracking marked where first observed.



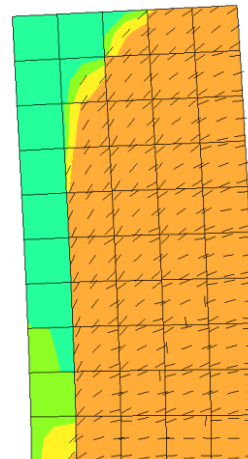
(a) LS 3: Initial flexural cracking



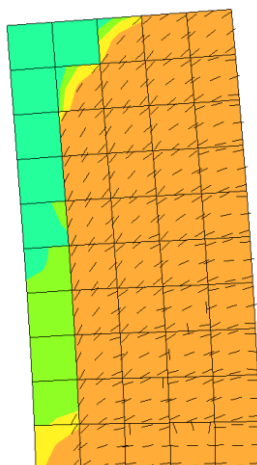
(b) LS 6



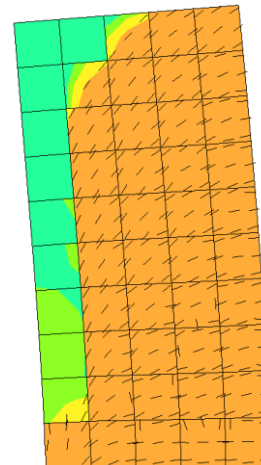
(c) LS 10



(d) LS 16: Initial reinforcement yielding

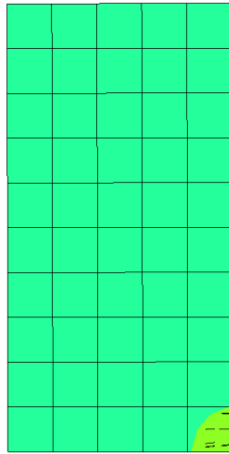


(e) LS 22: Peak load level

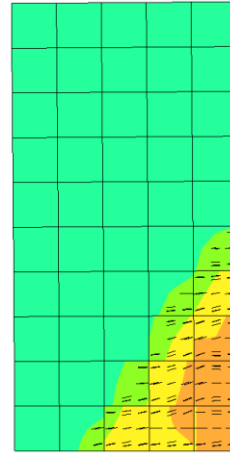


(f) LS 24: Post-peak

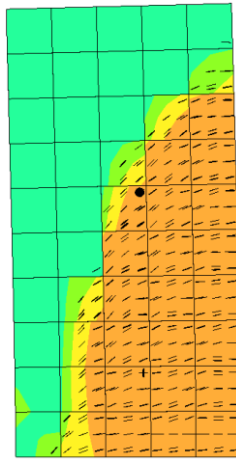
Figure 5.5: Propagating crack pattern and principle tensile strains in 2D base model, contour colour ranges are defined in Figure 5.1, deformation factor 10.



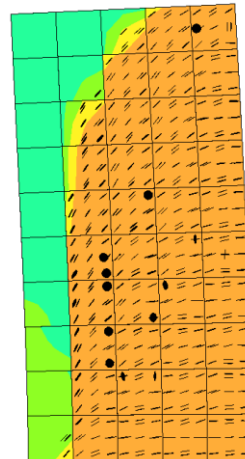
(a) LS 3: Initial flexural cracking



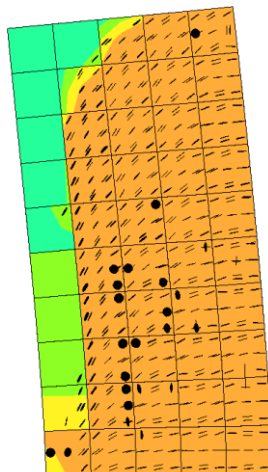
(b) LS 6



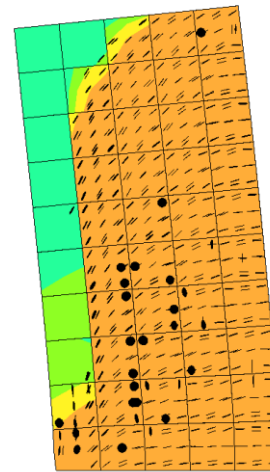
(c) LS 10



(d) LS 15: Initial reinforcement yielding.



(e) LS 28: Peak load level



(f) LS 30: Post-peak

Figure 5.6: Propagating crack pattern and principle tensile strains in 3D base model, contour colour ranges are defined in Figure 5.1, deformation factor 10. Believed small defect in DIANA visualization tool for deformed solids show internal cracks outside integration points.

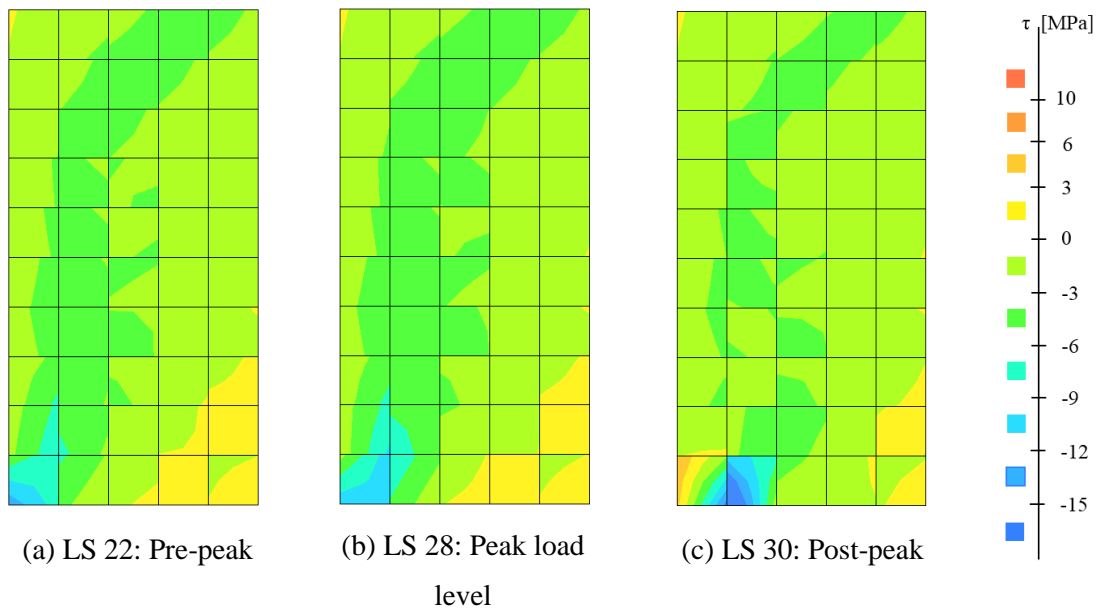


Figure 5.7: In-plane shear stress contour plot in 3D base model at high load levels.

5.1.4 Multiaxial stress state

Plane stress elements neglect the development of out-of-plane stresses. Prior to the observed failure, the critical compressive zone localizes within the outermost wall base element at the compressive edge in both base models, which is further referred to as the critical element and illustrated in Figure 5.8. P1 and P2 refer to the most critical compressive integration points observed before and after observed failure respectively. The effects observed and presented for this element were mainly or only observed here.

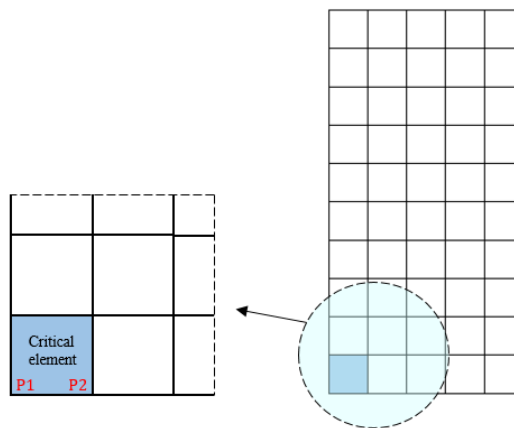


Figure 5.8: Defined critical element and integration points P1 and P2 illustrated.

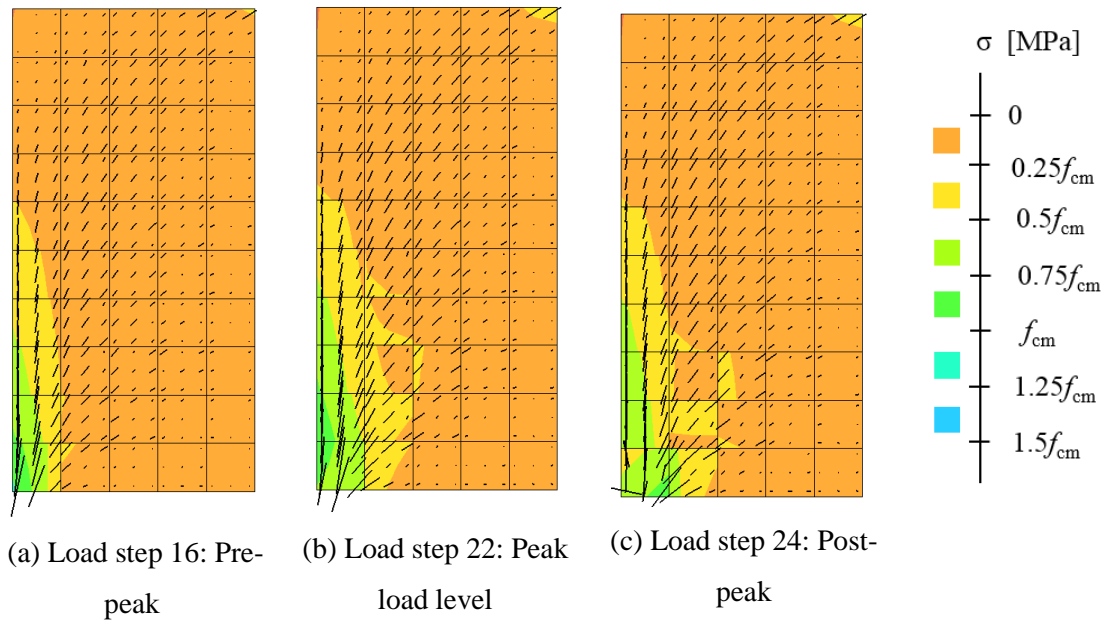


Figure 5.9: Principal compressive stress direction vector and contour plot in 2D base model at high load levels.

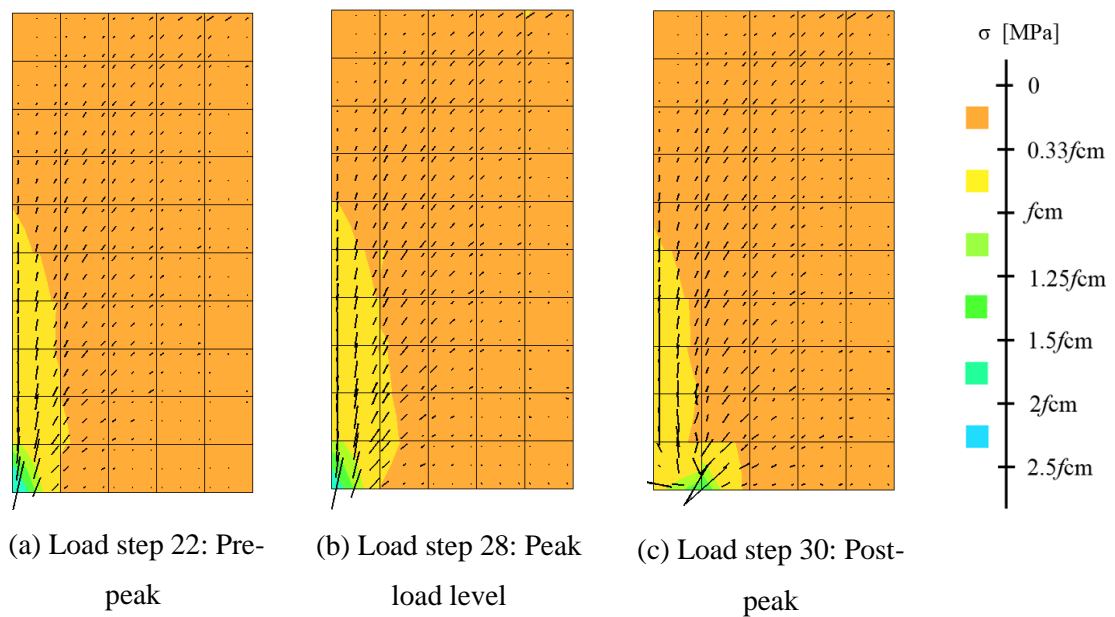


Figure 5.10: Principal compressive stress direction vector and contour plot in 3D base model at high load levels.

A substantial local triaxial compressive stress state occurs in the 3D base model, reaching a stress value of $2.16f_{cm}$ due to the confinement effects, see Figure 5.11(a) and Figure 5.10. Only some degree of confinement effects can be traced in the 2D base model, reaching $1.06f_{cm}$. A simultaneous rapid decrease of stress in P1 and increase in P2 occurs for both base models at peak load level, this illustrates the redistribution of the internal forces. The peak stresses in Figure 5.11(a) are reached almost simultaneously to yielding in compression of the vertical reinforcement, see Figure 5.3(b). Strain softening in compression is visualized in Figure 5.11(b), with decreasing stresses for increased strains after peak stress is exceeded.

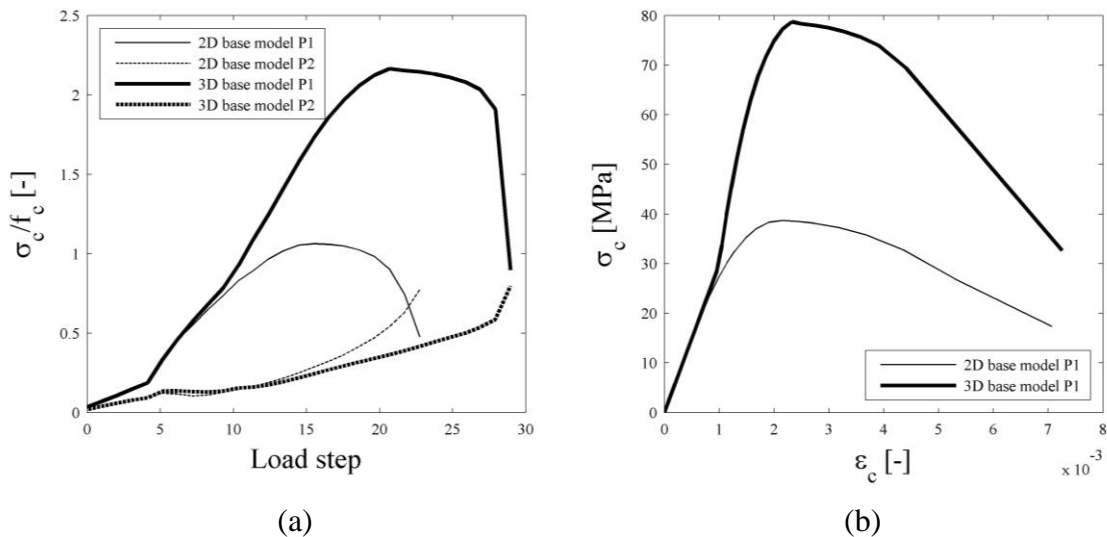


Figure 5.11: Principal compressive stress (a) before and after shift of compressive zone and (b) after shift against principal compressive strain. P1 and P2 defined in Figure 5.8.

5.1.5 Concrete expansion

The shear stirrups in the critical element are located as illustrated in Figure 5.12(a). Out-of-plane stresses at the upper and lower part of the critical element in both the concrete and shear stirrups are presented in Figure 5.12(b) to illustrate the distribution of stresses between the two components. Transverse concrete tensile stresses arise in the middle part of the critical element where no transverse reinforcement is located. This point coincides with the location where the first vertical cracks reach the compressive edge and initiates failure, referring to Figure 5.6(e).

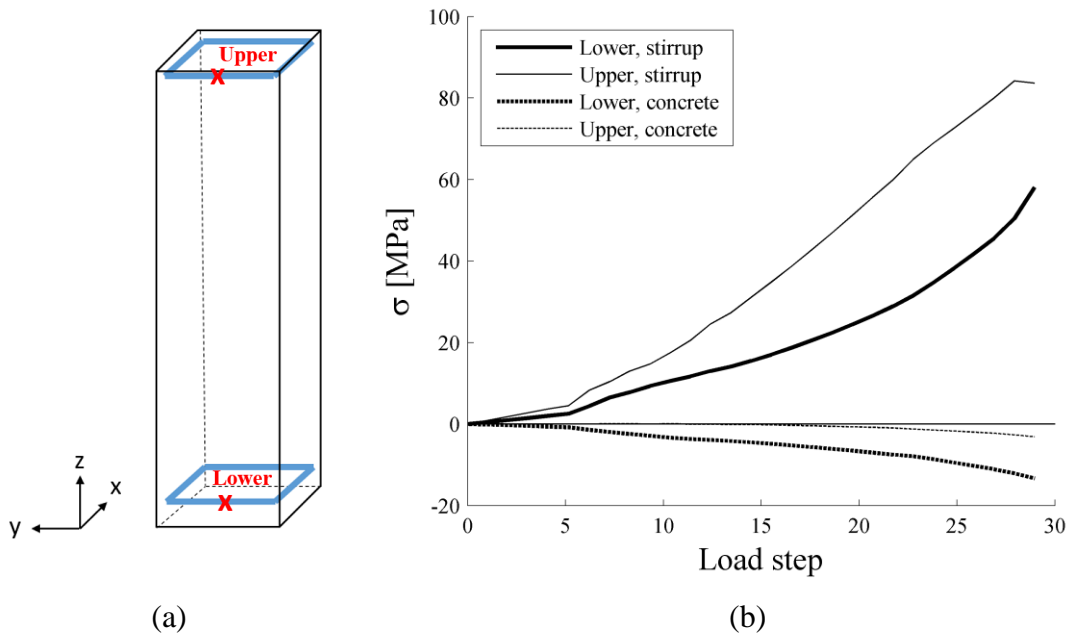


Figure 5.12: (a) Shear stirrups and interpretation points in the solid critical compressive element and (b) transverse stresses (y-direction) in the 3D base model.

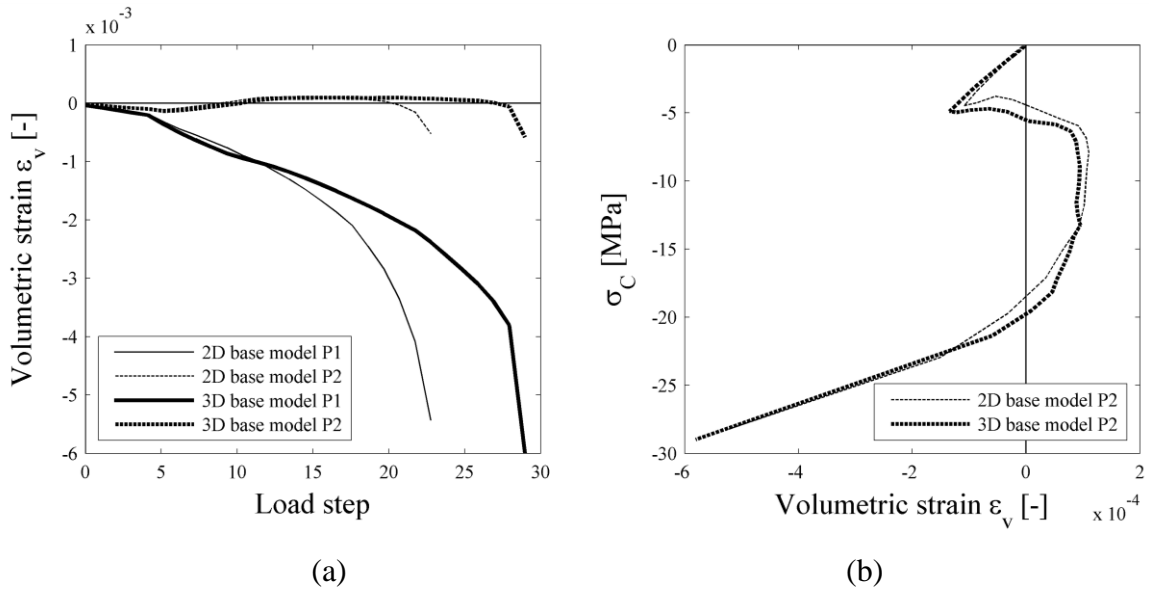


Figure 5.13: Volumetric strains (a) before and after shift of compressive zone and (b) after shift against principal compressive stress. P1 and P2 defined in Figure 5.8.

Lateral expansion is present in both base models, though out-of-plane displacements are only constrained in the 3D base model, by both restriction of the displacements along the wall base and by the closed shear stirrups. Volumetric strains ε_v can serve as a measure of volumetric compaction or dilatation of the concrete. Positive ε_v for concrete in compression

indicates a volumetric expansion. Mainly negative volumetric strains are apparent in the base models. Severe compaction in the critical element at high load is illustrated in Figure 5.13(a). Points of minimum volume, implying initiation of volumetric expansion, are not observed. Minor positive volumetric strains for compressive stresses are mostly observed in the integration points presented in Figure 5.13(b), though this may also be an inaccuracy due to the large finite element sizes supported by the large strain gradient within the critical element visualized in Figure 5.13(a). DIANA 9.6 provides an option for extracting volumetric shrinkage strains explicitly, which provided no results in any integration points for either base model, and hence confirms the shortage of volumetric concrete expansion.

5.1.6 Summary of the results from the base models

Both base models

- Prediction of a low ultimate load capacity compared with experimental results, reaching 76.9% and 85.0% of the experimentally tested load capacity for the 2D and 3D base model respectively.
- Strain softening in compression at critical regions and spitting failure in the compressive zone.
- Satisfactory initiation of flexural cracking and tensile reinforcement yielding. Yielding of vertical reinforcement in tension *and* compression prior to failure.
- Non-converged load steps only after reaching the peak load.
- Elevated stiffness, and delayed stiffness reduction, for low load levels.
- No volumetric expansion effects or clear points of minimum volume observed.

3D base model only

- Substantial triaxial compressive stress state, localized within a few critical integration points at the compressive toe of the wall specimen.
- Active transverse stirrups were of significance only in the critical compressive region.

5.2 Sensitivity study of the base models

Sensitivity analyses were performed to investigate the effect of certain input parameters in the solution strategies at hand, where the most relevant results are presented in the following.

5.2.1 Objective and results presentation

The material modelling indicates to be the main challenge for achieving good analysis results of the structural wall. Important material parameters and their effect on the global structural response are studied, to investigate the possible limitations in the solution strategy resulting in a low ultimate load capacity. Post-peak global response is presented for all analyses up to the experimental ultimate displacement of 20.6 mm, or until exceedance of the reinforcement ultimate strength f_{uk} . Non-converged load steps are not marked on the response curves. Note that several of the sensitivity analyses presented include unrealistically high values of certain concrete material parameters, and are purely to increase the understanding of the influence the parameters have to the current constitutive models.

5.2.2 Mesh sensitivity

The base models comprise five elements along the wall width. Quadratic finite element sizes of 65 mm and 32.5 mm implying ten and 20 elements along the wall width respectively predicted global responses presented in Figure 5.14. The material modelling is not altered despite a smaller scale of finite elements. The reduction in finite element size does not affect the ultimate load capacity significantly. The smaller finite element sizes result in a failure of the critical compressive vertical reinforcement bar directly after the peak load. The smallest finite elements increases the CPU time of a factor 8.7 and 11.1 compared the 2D and 3D base model respectively.

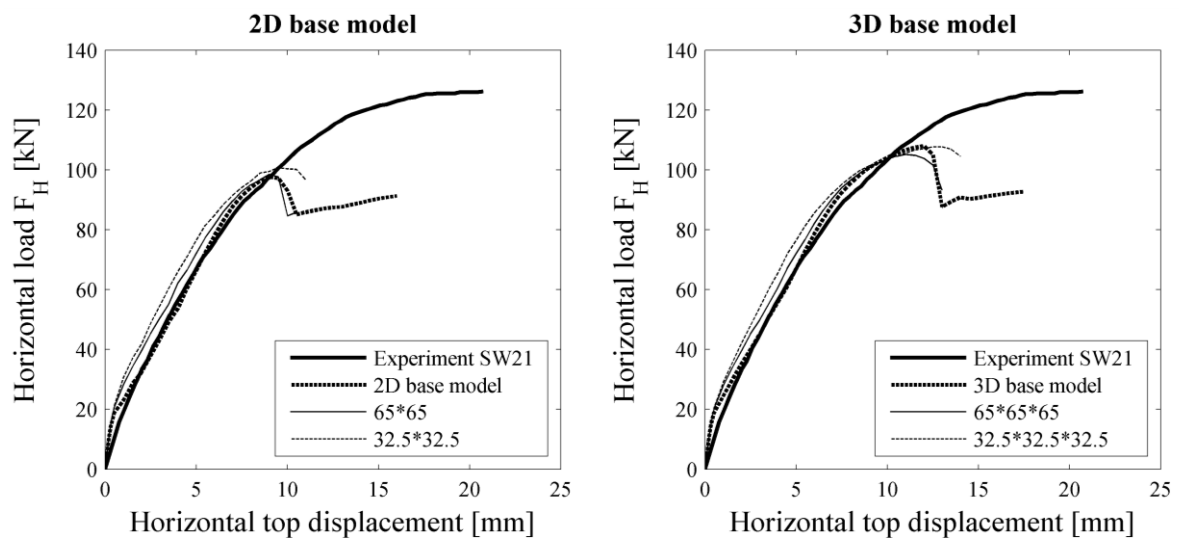


Figure 5.14: Mesh sensitivity analyses. Finite element dimensions in mm.

5.2.3 Tensile behaviour and crack models

DG recommend the use of a variable shear retention factor for a fixed crack model formulation, while the base models utilize a constant value of SRF of 0.1. The effect of a low constant value of SRF of 0.01 and the damage formulation provided by DIANA was studied, see Figure 5.15. A brittle tension model disregards any post-peak concrete tensile strength by reducing the strength to zero in cracked concrete. A rotating crack model predicts almost identical ultimate load capacity as the fixed crack model used in the base models.

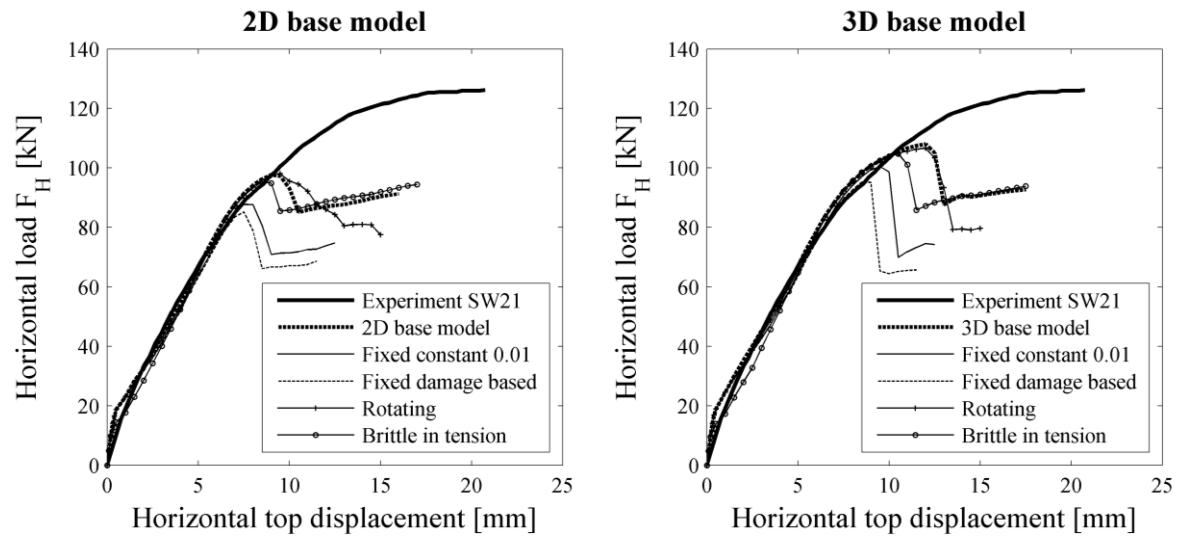


Figure 5.15: Sensitivity to concrete tension and crack modelling.

5.2.4 Compressive behaviour

Early analyses indicated the constitutive model for concrete compressive behaviour to be of great importance for failure at a low load level. The high values of the compressive fracture energy G_C in Figure 5.16 are for ad-hoc modelling only. The ideal compressive behaviour exerts a linear elastic behaviour until the concrete strength is reached, with a following perfect plasticity with no limit of the ultimate strain ϵ_{cu} . The concrete stress values does not exceed the values reported in section 5.1. The results in Figure 5.16 indicate that the compressive post-peak descending branch limits the global ductility.

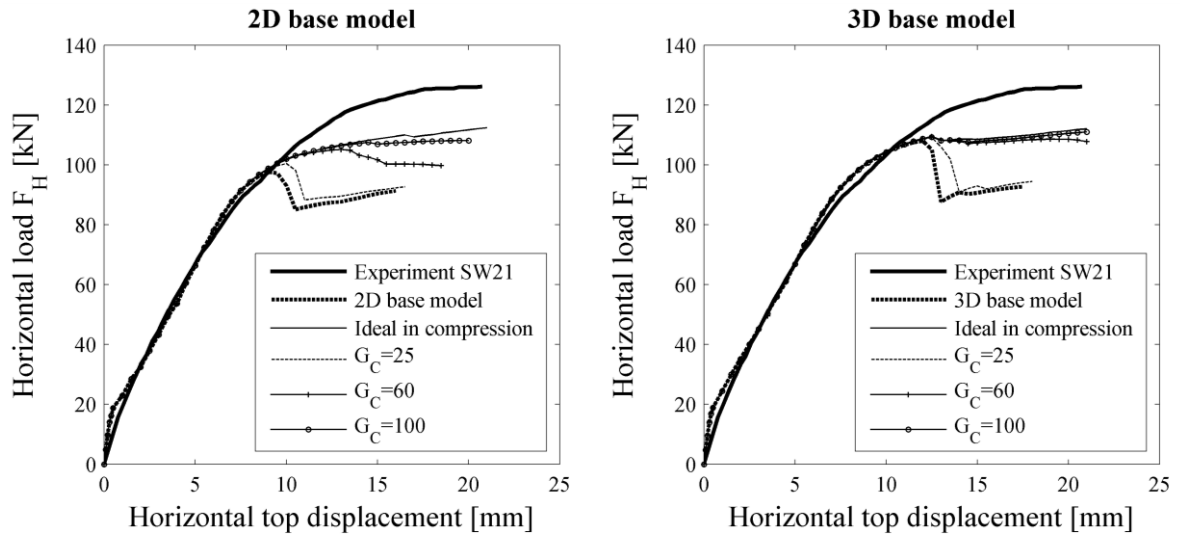


Figure 5.16: Sensitivity to concrete compressive modelling. Ad-hoc modelling with spurious high values of G_C .

5.2.5 Concrete expansion and passive confinement effect

Only small values of lateral expansion were apparent in the base models with a constant value of Poisson’s ratio of $\nu=0.15$. Increase of ν alone, up to a spurious high value of $\nu=0.4$, proves no significant increase of the ultimate ductility or load capacity, ref. Figure 5.17. $\nu=0.2$ in the 2D base model coincides with the base model result.

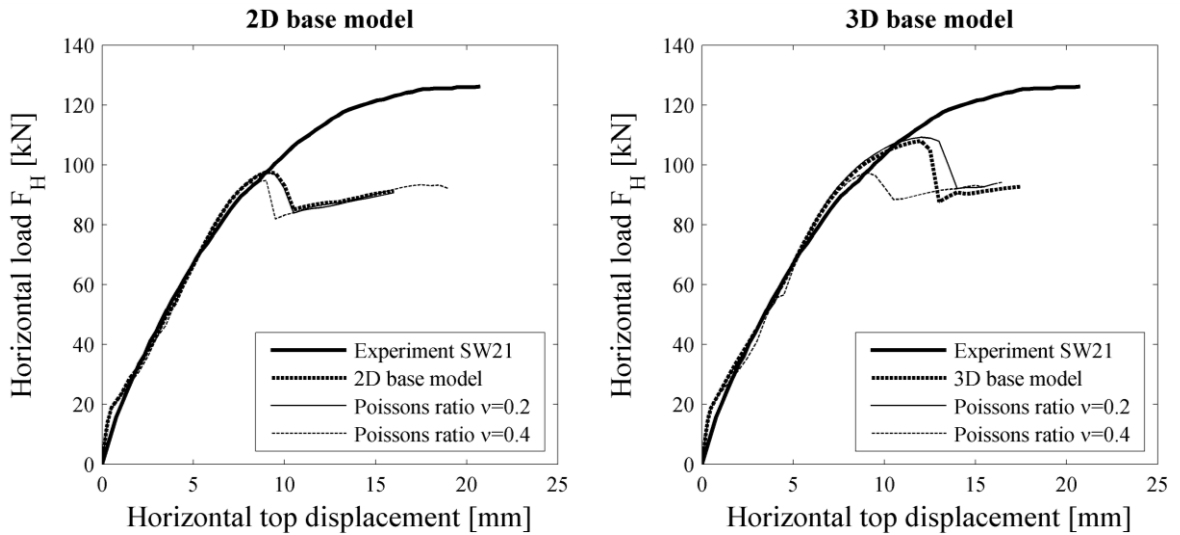


Figure 5.17: Sensitivity to Poisson’s ratio. Ad-hoc modelling with $\nu=0.4$.

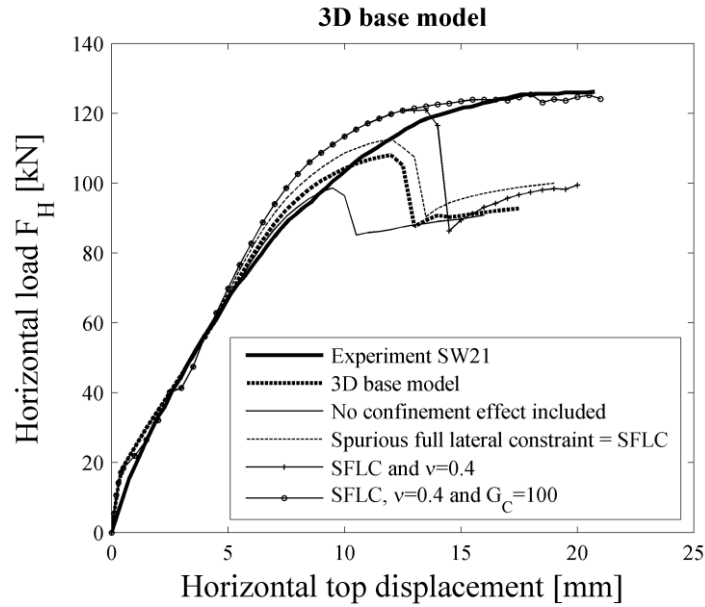


Figure 5.18: Sensitivity to confinement effects in the 3D base model. SFLC only for ad-hoc modelling.

Disregarding the lateral confinement effect in the 2D base model had no visible influence on the global response, though disregarding the same effect in the 3D base model results in a global response almost identical to the 2D base model response, presented in Figure 5.18. For ad-hoc modelling of passive confinement effects, all out-of-plane displacement of the walls surfaces were restrained, in attempt to imitate a spurious full lateral constraint (SFLC), and following increased passive lateral confinement where lateral concrete expansion is apparent. Simultaneous spurious high values of the parameters G_C and ν provides global response approaching the reported experimental ductility and load capacity. The two latter analyses result in high stress values up to 3-4 times f_{cm} , and only serve as an indication of the influence of large passive confinement effects.

5.2.6 Summary of the sensitivity analyses

The overall structural behaviour is interpreted as fairly mesh insensitive. In relation to the global behaviour of the rotating crack model that in provides a lower failure load [8], the shear retention value of 0.1 in the fixed crack model appears appropriate. The increased passive confinement effects due to a constrained large concrete expansion indicates that an actual volumetric expansion could have increased the strength, and the descending branch of the compressive curve indicates to govern the ductility of the structure.

6 Discussion of results from the case study

The structural response validation and mesh sensitivity study are important aspects of the model validation process. Two *base models* with respectively plane stress elements and solid brick elements both resulted in a low prediction of the load capacity and ductility, though with a satisfactory and similar global behaviour until failure initiated. The predictions of initial flexural cracking and reinforcement yielding were in good correlation with values reported from the experimental test and the study of the failure mode and stress state at failure indicated a satisfactorily reproduction compared to the described failure process in the experimental report, though for a lower applied horizontal load level.

The sensitivity study in section 5.2 strongly indicated that the constitutive modelling was the main source of limitations. A discussion of the observed effects and limitations from the base model study and the sensitivity study is presented, followed by a final selection of a solution strategy for structural walls based on the 2D or the 3D base model. The limitations may be coupled to the solution strategy, the used FEA software DIANA, or both.

6.1 Multiaxial stress effects

6.1.1 Concrete confinement effects

The increase of the ultimate load capacity from the 2D base model to the 3D base model was identified to be mainly from concrete confinement effects in the latter model, since ignoring these effects in the 3D base model gave a global response practically identical to the 2D base model, illustrated in Figure 5.18. Significant confined concrete stress values were observed in the outermost compressive integration points at the wall base, see Figure 5.10. Passive lateral confinement indicated to occur mainly due to the boundary conditions at the wall base, in addition to some effect from the active shear stirrup reinforcement within the critical compressive element only, ref. Figure 5.12. Vecchio reported a compressive principal stress magnitude at failure of $1.55f_{cm}$, at the compressive toe in a type I wall with additional axial loading [31]. This is not directly comparable with the

SW21 wall specimen, however the 3D base model results showed a maximum stress of $2.16f_{cm}$ at a load level of about 77.4% of the experimental ultimate load capacity. This indicates a possible spurious high stress state occurring at a low applied load level, and may have limited the load capacity by initiating a premature failure. The behaviour for confined concrete compressive behaviour is further discussed in section 6.2.

6.1.2 Volumetric concrete expansion

The volumetric expansion effect in concrete was discussed by researchers some decades ago [28, 31, 41], and was regarded as an essential aspect of realistic modelling of three-dimensional reinforced concrete behaviour. However, DG does not mention this effect and DIANA only provides a constant Poisson's ratio until cracking occurs [24, 32], which limits the desired volumetric concrete expansion and further possible increased passive confinement effects in the restrained regions. The global increase of v shown in Figure 5.17 leads to an increased concrete expansion in all material points and thus no restraining by the neighbouring concrete. A volumetric expansion of the concrete would presumably have increased the passive confinement effects exerted by both the neighbouring concrete, the boundary conditions and the shear stirrups [31].

In a recently published article by Engen, the same wall specimen was analysed with large elements, using the solution strategy based on DG and the DIANA software [5]. With a simplified reinforcement layout along the element edges, the solution strategy reached 71% of the experimental load capacity. Engen stated the low load capacity probably due to the constant Poisson's ratio prior to cracking [5]. This study also supports the observed behaviour in chapter 5 by a similar global response. Vecchio modelled the Lefas et.al wall specimens with inclusion of an elevated modelled concrete expansion by an increasing Poisson's ratio for increasing compressive strains [31], see Figure 3.5(b). The global response for the wall specimens were predicted in correlation with the experiment results. However, also with no expansion effects modelled, representative load capacities were predicted. The SW21 wall specimen in Vecchios study reached 91.3% of the experimental load capacity with no lateral concrete expansion modelled, and 97.6% with expansion modelled [31]. Another difference of significance in Vecchios model compared to the base models was the constitutive model for confined concrete, with increasing peak strain values for confined concrete and a lower limit of post-peak stress, ref. Figure 3.4(b). These results

in comparison with the case study results indicates that a volumetric expansion effect is not alone responsible for the low predicted ultimate load capacity of the structural wall predicted by the 2D and 3D base models.

6.2 Concrete compressive behaviour

To obtain mesh objectivity, the descending branch of the stress-strain curves were defined by an energy criterion using fracture mechanics. The compressive fracture energy G_C is estimated as a constant value based on the tensile fracture energy G_F . The sensitivity study revealed an increase of ductility for spurious high values of the compressive fracture energy, ref. Figure 5.16 and Figure 5.18. The cause of the increase may be explained by examining the parabolic compressive curve provided by DIANA 9.6. DG specifically suggest use of a parabolic compressive curve. A single-element finite element model was used to study the compressive behaviour in DIANA, as the user manual was some ambiguous regarding the increase of the peak strain in addition to peak stress under confining pressure. The single element study is explained further in Appendix D, with results presented in Figure 6.1. The area under the descending branch of the unconfined curve was confirmed equal to G_C/h_{eq} , defining the energy during the crushing process of concrete.

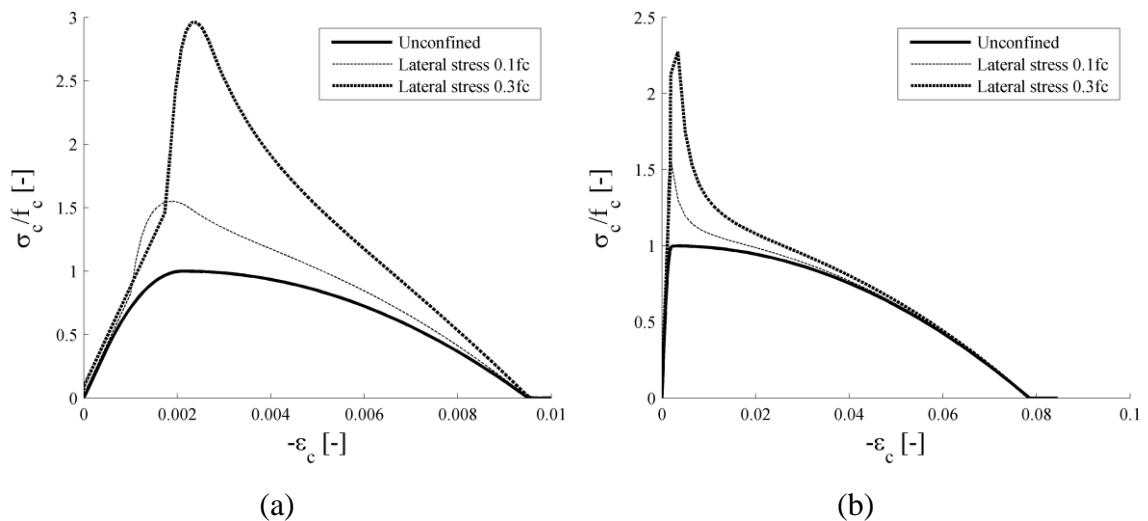


Figure 6.1: Parabolic compressive curve for a single solid finite element with size (a) 130*130*65 mm and (b) 10*10*10 mm. Vertical Gaussian concrete stresses and strains.

An inconsistency for varying lateral stress values are visible in Figure 6.1(a), by a peak strain both decreased and increased from the unconfined concrete value. The reason for this is unsettled. On basis of the results in Figure 6.1, the peak strain does not experience any increase of significance in the parabolic curve provided by DIANA for confined concrete, within these presented values of confinement stresses. A greater increase of the confined peak strain could perhaps have delayed the failure, though the same limited ductility was observed in the 2D base model where no confinement effects of significance occurred.

The compressive fracture energy shows a tendency to increase for confined concrete in this study, though not proportional with the stress increase. For a lateral stress value of $0.3f_c$, G_C increased by a factor 1.2 in Figure 6.1 (a) and 1.3 in Figure 6.1(b), compared to the stress increase factors of respectively 3.0 and 2.3. The default crushing bandwidth h_{eq} in DIANA is a constant value, and the compressive fracture energy observed to increase by a small factor only. That is, the energy of the crushing process is practically a constant value, and the descending branch becomes steep for a high degree of confinement as illustrated in Figure 6.1. The descending branch of the parabolic curve provided by DIANA 9.6 clearly decreases to zero stress and with no peak strain increase of significance for the confinement pressures presented. This may be questioned as too conservative, by not embracing the increased capacity in confined concrete adequately.

6.3 Concrete tensile behaviour and structural stiffness

The tensile material model in the solution strategy provided by *the Dutch guidelines* (DG) treats the concrete as a linear elastic material until initiated cracking, and a suitable failure criterion in tension is essential for accurate prediction of the structural stiffness reduction due to cracking of concrete. The small differences in the global response in the pre-peak region observed when using a rotating crack model, ref. Figure 5.15, could be explained by no significant rotation of the principal stress field until initiation of failure. This is also in agreement with results on the large-scale element model by Stene Pettersen [32], and Figure 5.10. A small value of SRF of 0.01 in the fixed crack model reduced the amount of visible stress locking, though resulted in a brittle structural behaviour and early failure. This may imply a too small shear stress transfer in the cracked regions, and supports the use of a SRF of 0.1.

The secant stiffness in Figure 5.4 revealed a high stiffness for low load levels that may have contributed to a possible premature development of a critical stress state at the compressive toe. The accuracy of the structural stiffness calculation has a significant influence to the global structural response [13]. The divergence in the stiffness may be a result of the orthogonal crack model, restraining new crack initiations orthogonal to the previous cracks. The modelled decreasing Poisson's ratio due to cracking and damage of the concrete follows the same rate of degradation as the secant modulus, which affects the apparent multiaxial stress state.

6.4 Other observed effects

Correct representation of the boundary conditions is crucial for a realistic reproduction of the structural behaviour. The model generations presented in Appendix B indicate that the boundary conditions applied in the base models are representative. The assumed perfect bond to the reinforcement may be unsuitable for structures where extensive cracking and the occurrence of strain softening in compression generates large concrete strains, affecting the structural stiffness. Prescribed load steps should be used with care in practical design as it limits structural changes to certain intervals, though it is a stable and useful method for research work such as this thesis. Variations within the solution procedure proved to have a low significance to the global response, also confirmed by the previous study by Stene Pettersen where load control, arc-length method and Quasi-Newton method generated similar results [32]. The accuracy of the coarse mesh is interpreted as sufficient from the results in the case study, supported by the mesh sensitivity study presented in Figure 5.14. Neither smaller initial load steps nor smaller finite element sizes affected the ultimate load capacity significantly in the two base models.

Uncertainties and inaccuracies in the experimental setup and report could affect the interpretation of the analysis results, since this is the only reference for comparison. Previous studies with nearly exact predictions of the wall specimens load capacities, using other solution strategies and FEA softwares, weakens this as a factor of importance [31]. User factors and human errors are also possible sources of limitations, although comparison to similar studies on structural walls modelled in DIANA confirms a comparable behaviour

[5, 32]. The use of the recommendations by DG for all the main input also limits the user factor.

6.5 Selection of solution strategy

The application of the solution strategy based on *the Dutch guidelines* (DG) to a structural wall using the DIANA software, indicated some deficiencies that caused a low predicted ultimate load capacity. The identified main possible limitations from the previous sections comprise the lack of volumetric concrete expansion, the post-peak concrete compressive behaviour and a poor prediction of the structural stiffness for low load levels. DG allows for a full three-dimensional solution strategy, though is to date only verified for beams and girders where multiaxial compressive stress states are less prominent.

The case study nevertheless revealed that a three-dimensional finite element model is necessary for reproduction of the observed multiaxial stress state occurring in this structural wall using the provided solution strategies. The simplification of the wall into a plane stress problem lead to conservative results, though the solution strategy with both element types generated too low load capacities. The selected solution strategy thus comprises the solution strategy defined for the 3D base model, with solid brick elements. The continuing study in Part III with estimation the modelling uncertainty and structural safety assessment of a structural wall utilizes this selected solution strategy. The remaining study also serves as a further assessment and model validation of the selected solution strategy's application to structural walls in general.

PART III: THE MODELLING
UNCERTAINTY AND
STRUCUTRAL SAFETY
ASSESSMENT

7 Estimation of the modelling uncertainty

7.1 Introduction

Section 2.5 presented an overview of the most relevant safety formats in *fib* Model Code 2010 and DG, where low and predefined values of the modelling uncertainty is provided for well-validated models [1, 8]. The *improved ECOV* by Schlune et.al allows for inclusion of the estimated modelling uncertainty by the mean ratio θ_m and the coefficient of variation of the modelling V_θ . To assess the applicability and validity of the selected solution strategy in part II to structural walls in general, before utilizing the model in a structural safety assessment, multiple wall specimens were analysed using the selected solution strategy, and the modelling uncertainty estimated by a statistical approach.

7.2 Application of the selected solution strategy to multiple structural walls

13 reinforced concrete structural walls with varying geometry, concrete strength and applied loading were tested to failure by Lefas et.al [9]. Six of these wall specimens have been modelled and analysed in DIANA, using the selected solution strategy from Part II. The axial load F_v on the top wall surface was applied as a uniform pressure over the walls cross section, and material parameters for all wall specimens calculated as presented in section 4.2.4. Table 6.1 presents an overview of the axial load F_v and mean concrete strengths for the six walls.

7.2.1 Revised results from the experiment by Lefas et.al

All the wall specimens experienced a similar failure process and resulting failure mode as described in section 4.1.1. High axial load levels applied to the type II walls resulted in uncracked concrete regions at the top third of the walls. Additional axial loading also resulted in a wider compressive zone at failure, an increased ultimate load capacity and structural stiffness to horizontal loading, and a smaller horizontal displacement at failure.

7.2.2 Revised solution strategy

The selected solution strategy, ref. section 4.2 and section 6.5, was applied directly to the three type II walls, and with small revisions for implementation of additional axial load and

to fit the type I walls geometry. Only items differing from the selected solution strategy will be commented in the following.

Geometry, boundary conditions and loading

The geometry of the two wall types are presented in Figure 7.1(a) and Figure 4.2(a). The displacement control method generates prescribed initial displacement values at these nodes, resulting in a physical constraint in the model. A phased analysis was introduced to allow for application of the axial loading to an unconstrained structure. The axial load F_V was applied prior to the horizontal loading, as a uniform pressure over the wall cross section area, and held constant during the monotonically increasing horizontal load F_H . The reinforcement layout is presented in Figure 7.1(b) and modelled as for the type II walls.

Finite element discretization

Preliminary linear FEAs of the type I walls was performed by the same approach as described in section 4.2.1, presented in Appendix A, which resulted in solid brick elements of 150*150*70 mm for the type I walls on same basis as presented in section 4.2.2, see Figure 7.1(b). This results in five elements along the wall base, similar as for the type II walls,

Numerical material modelling

The constitutive modelling is presented in section 4.2.4 and is equal for all the wall specimens, though with varying concrete strengths presented in Table 7.1 and with mean material parameters calculated as presented in section 4.2.4.

Load incrementation

The type I walls were reported with a significantly smaller ultimate displacement in the experiment compared to the type II walls, and a revised load incrementation sequence for the type I walls was implemented to initiate failure within 20-30 load steps for all the wall specimens. The load sequence of the type I walls comprised ten load steps of 0.05 mm for detection of initial cracking, followed by steps of 0.25 mm until failure or no convergence occurred.

Table 7.1: Six wall specimens tested experimentally by Lefas et.al [9]. b and t are the width and the thickness of the walls respectively.

Wall specimen	Wall type	Concrete mean cylinder strength f_{cm} [MPa]	Axial load F_v [kN]	Normalised axial load $v \approx \frac{F_v}{bt f_{cm}}$
SW11	I	44.5	0	0.0
SW12	I	45.6	230	0.1
SW13	I	34.5	355	0.2
SW21	II	36.4	0	0.0
SW22	II	43.0	182	0.1
SW23	II	40.6	343	0.2

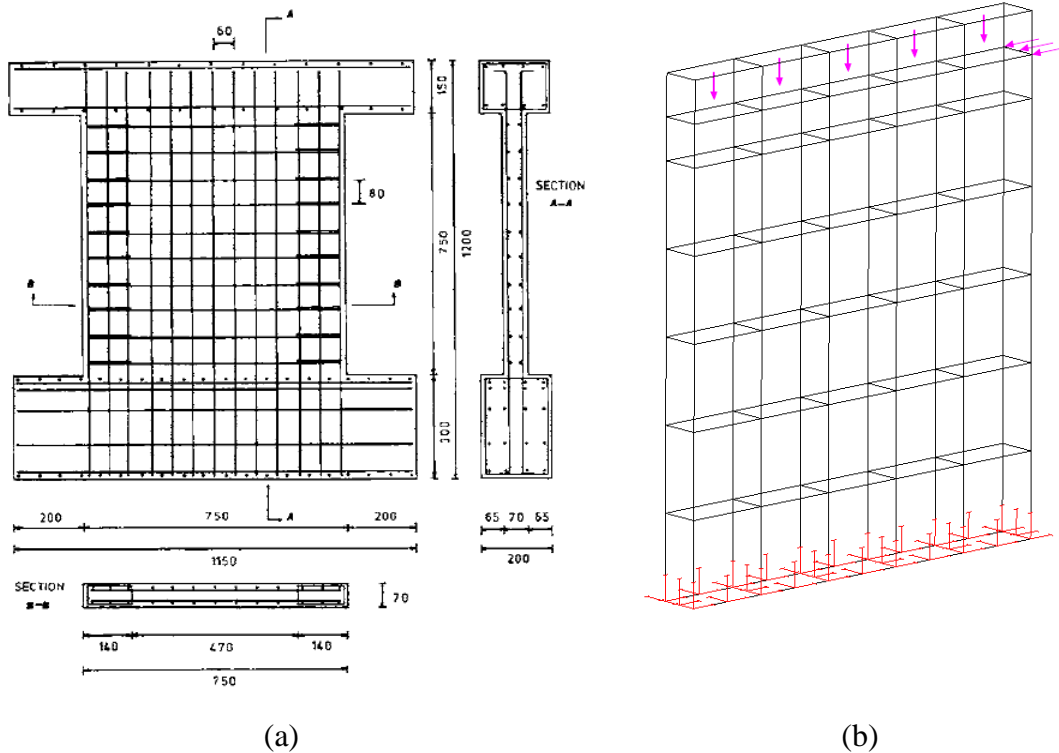


Figure 7.1: (a) Geometry and reinforcement details of type I wall specimen [9] and (b) mesh, boundary conditions and loading on type I wall with axial loading.

7.2.3 Results from NLFEA of multiple walls

The main results from NLFEA of the six wall specimens are summarized in Table 7.2 and the load-displacement response in Figure 7.2. The post-peak behaviour was similar as observed in the case study, with an initial drop and spurious high stress values due to stress locking. The load-displacement curves are hence presented up to the first non-converged load step, which was at or directly after initial peak load for all the analyses. A low ductility, an underestimation of the ultimate load capacity and a general too stiff global structural behaviour was common for all the analyses. Coarse initial load steps in the solution procedure for the type II walls resulted in an initial flexural cracking at a high load level. Smaller initial load steps proved more accurate, though had no influence on the ultimate load capacity that is the main objective. The secant stiffness in Figure 7.3 is estimated as presented in section 5.1.3. The delayed initiation of flexural cracking and high stiffness at low load levels is visible for all the analyses, though aggravated in the analyses with additional axial load, see Figure 7.3.

Table 7.2: NLFEA and experimental results for the six wall specimens [9].

Wall specimen	Initial flexural cracking				Initial tensile reinforcement yielding				Ultimate load capacity			
	δ		F_H		δ		F_H		δ		F_H	
	[mm]		[kN]		[mm]		[kN]		[mm]		[kN]	
	DG	EXP	DG	EXP	DG	EXP	DG	EXP	DG	EXP	DG	EXP
SW11	0.15	0.32	32.9	35	2.75	3.59	230.6	170	4.50	8.25	227.2	260
SW12	0.30	0.26	65.4	45	3.00	2.90	242.9	210	4.00	8.86	274.4	340
SW13	0.40	0.37	81.8	50	3.25	3.82	251.5	250	3.25	8.88	251.5	330
SW21	0.30	0.32	13.9	10	5.50	5.81	73.1	80	12.00	20.61	108.0	127
SW22	1.00	0.39	43.3	14	6.00	4.91	107.1	110	9.50	15.30	131.5	150
SW23	1.00	0.52	48.4	20	6.50	5.20	131.1	120	7.50	13.19	137.7	180

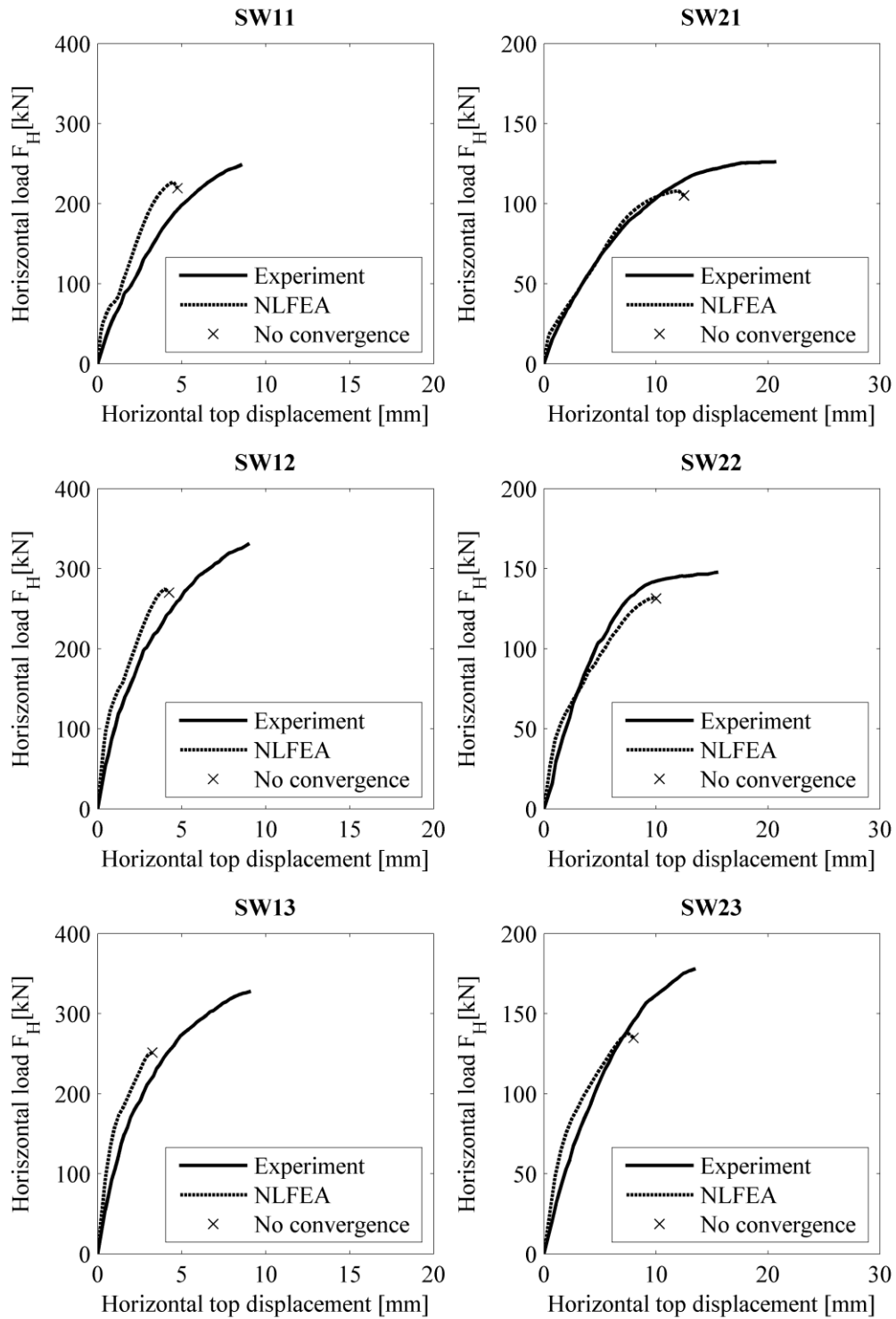


Figure 7.2: Load-displacement response. NLFEA and experimental results for the six wall specimens.

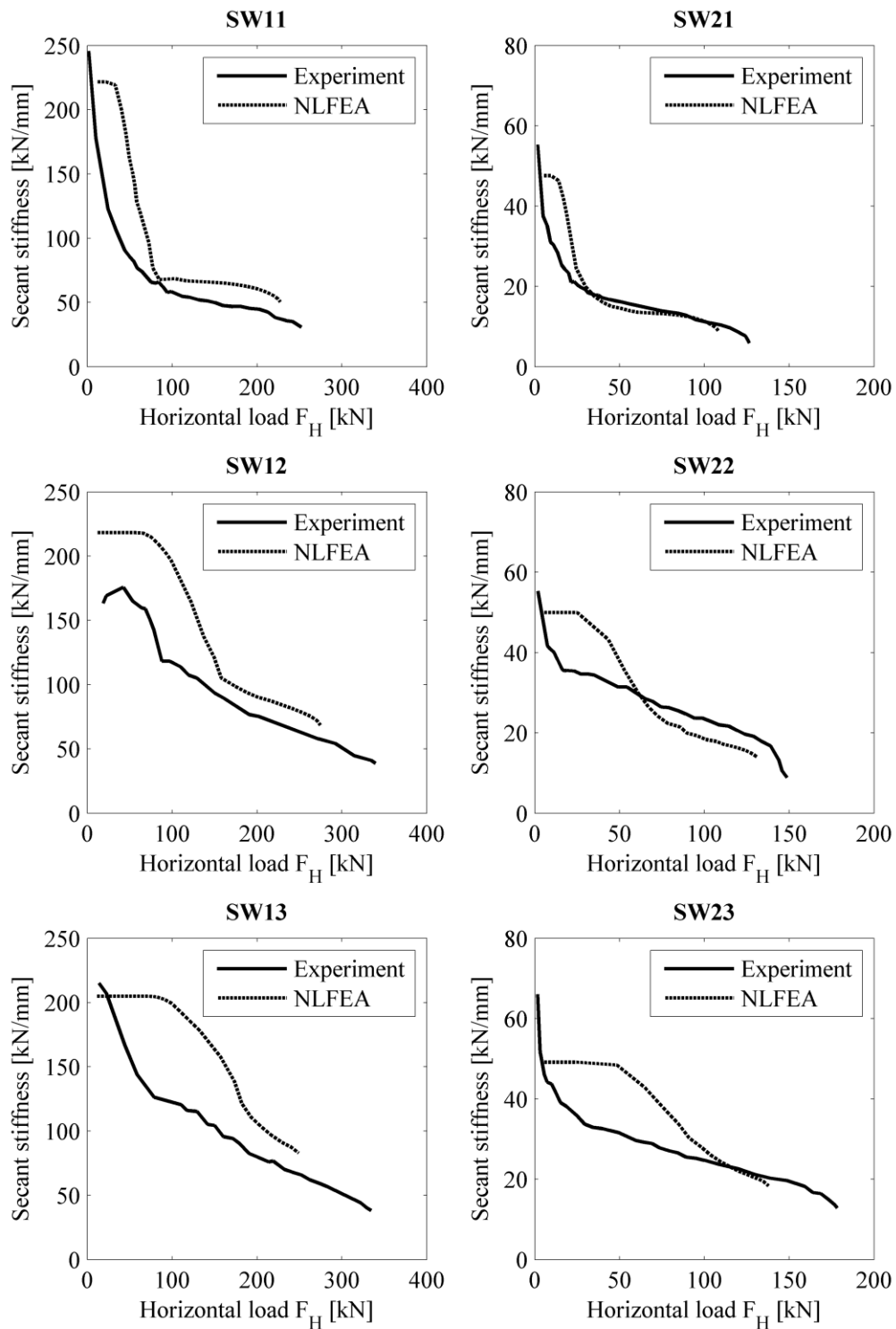


Figure 7.3: Secant stiffness. NLFEA and experimental values for the six wall specimens.

Failure modes

Figure 7.4 to 7.9 visualize the failure mode in the six wall specimens related to the description in section 5.1.2, Figure 5.1 defines the colour ranges for the tensile strain values. Initial yielding refer to the initial yielding of the vertical reinforcement bars at the tensile edge. Note that the load steps in the solution strategy for type I and II wall specimens differ, to generate failure within 20-30 load steps. Only behaviour diverging from the observed and interpreted behaviour in chapter 5.1 is commented.

SW11

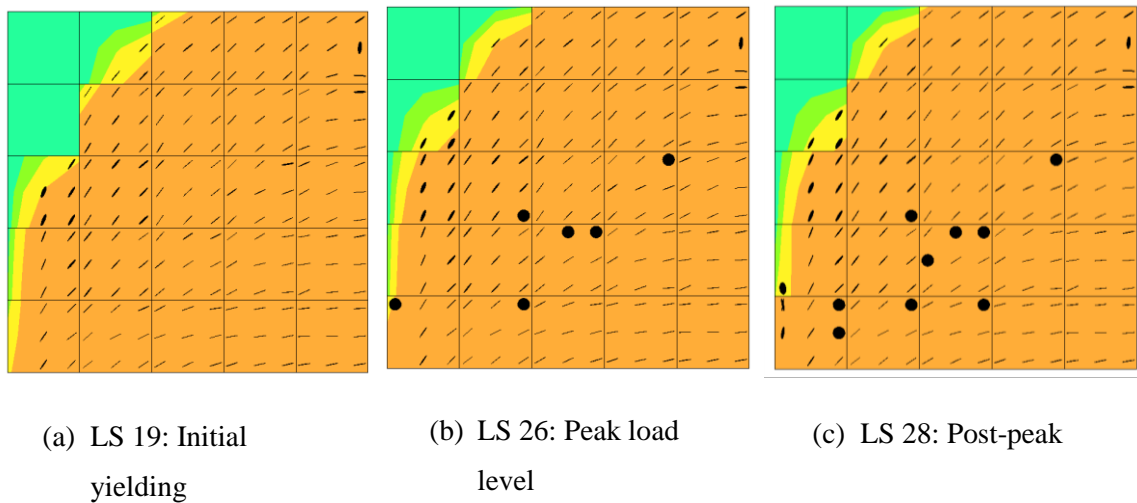


Figure 7.4: Wall specimen SW11. Propagating crack pattern and principle tensile strains at high load levels. Colour contour ranges are defined in Figure 5.1.

SW12

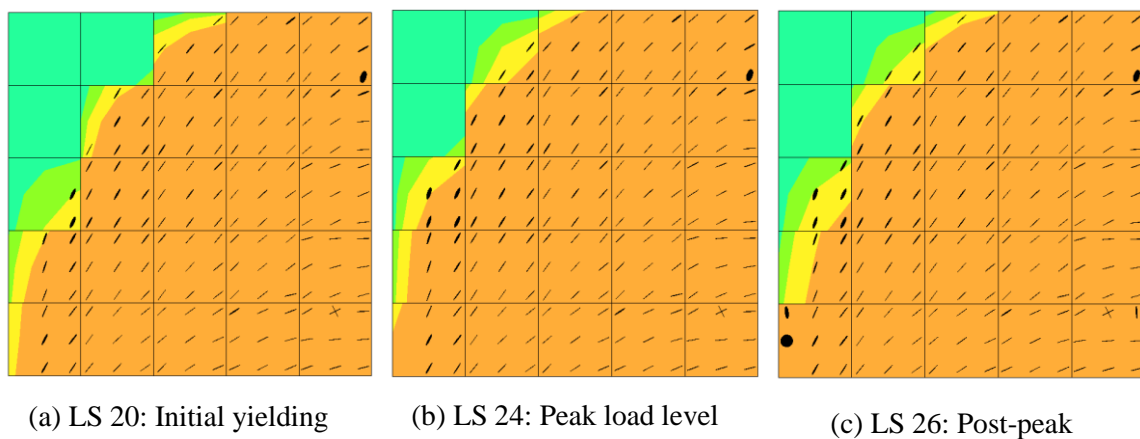
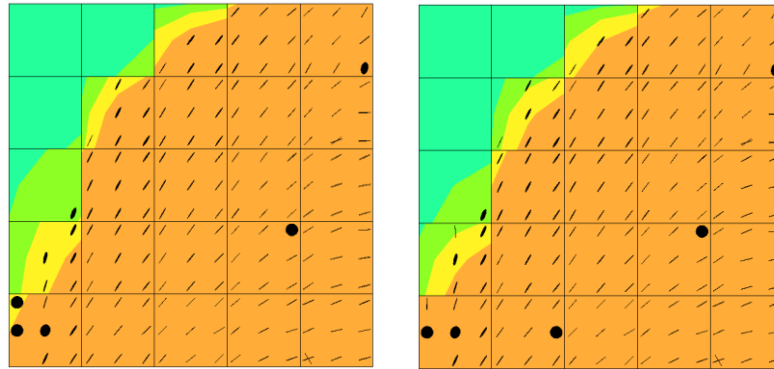


Figure 7.5: Wall specimen SW12. Propagating crack pattern and principle tensile strains at high load levels. Colour contour ranges are defined in Figure 5.1.

SW13

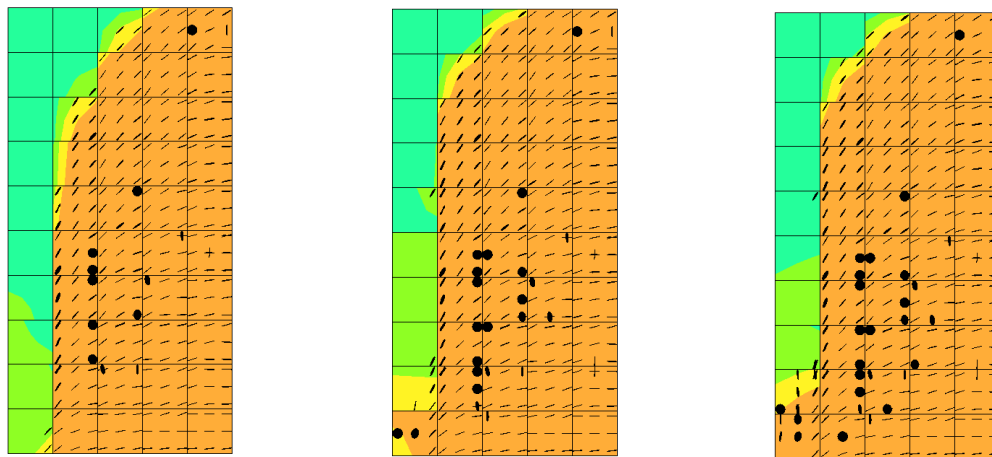
The wall specimen SW13 yields at the tensile edge and reaches the peak load level at the same load step. Yielding in the vertical reinforcement at the compressive edge occurs at load step 18.



(a) LS 21: Initial yielding
and peak load level

(b) LS 23: Post-peak

Figure 7.6: Wall specimen SW13. Propagating crack pattern and principle tensile strains at high load levels. Colour contour ranges are defined in Figure 5.1.

SW21

(c) LS 15: Initial yielding

(d) LS 28: Peak load

(e) LS 30: Post-peak

level

Figure 7.7: Wall specimen SW21. Propagating crack pattern and principle tensile strains at high load levels. Colour contour ranges are defined in Figure 5.1.

SW22

The crack localization at the peak load level varies some, compared to the previous four walls, visible in Figure 7.8. A smaller portion of the wall specimen is fully cracked at lower load levels compared to SW21 with no axial loading.

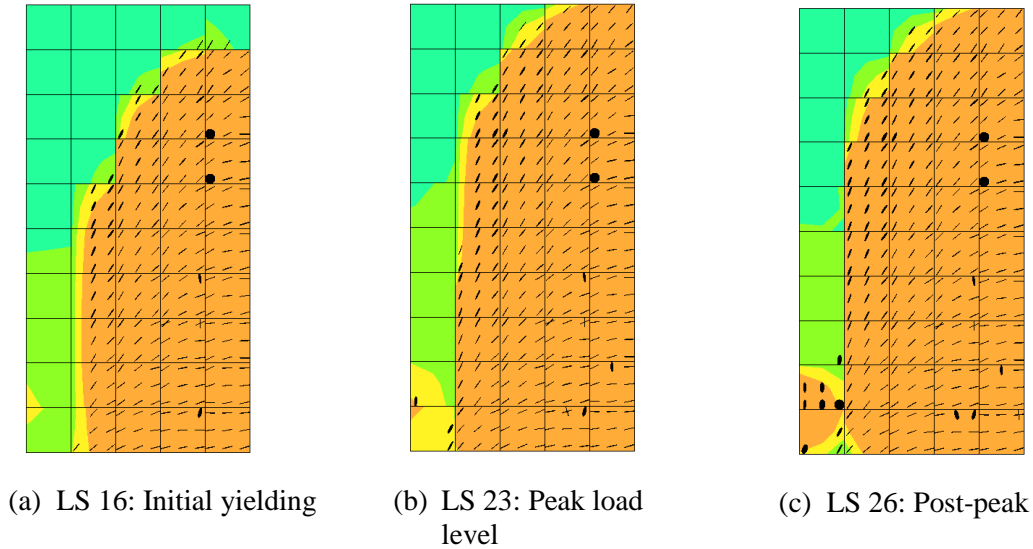


Figure 7.8: Wall specimen SW22. Propagating crack pattern and principle tensile strains at high load levels. Colour contour ranges are defined in Figure 5.1..

SW23

A similar behaviour as for SW22 is observed, as described above. Yielding in the vertical reinforcement bar at the compressive edge occurs at load step 15.

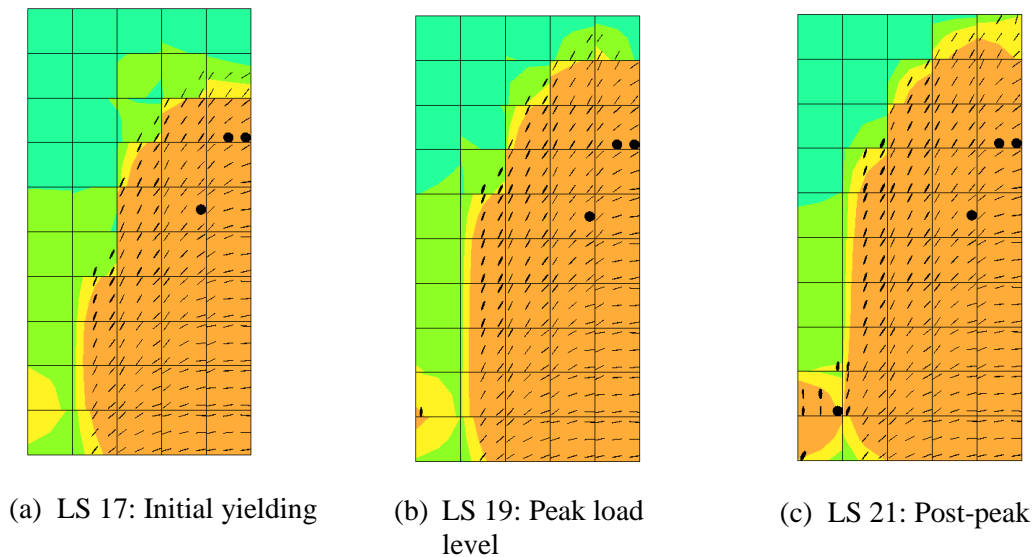


Figure 7.9: Wall specimen SW23. Propagating crack pattern and principle tensile strains at high load levels. Colour contour ranges are defined in Figure 5.1.

7.3 Estimation of the modelling uncertainty

The modelling uncertainty for structural walls with the selected solution strategy and FEA software is estimated on the basis of the predicted ultimate load capacities R_{um} for the multiple walls in the previous section, and the corresponding experimental load capacities R_{exp} . The modelling uncertainty is defined using the definition by JCSS [19] by the mean ratio of experimental to numerically predicted strength of all analyses θ_m and the corresponding coefficient of variation of modelling V_θ . The results are presented in Table 7.3. A systematic underestimation of the ultimate load capacity in all the wall specimens is visualized by a significant mean ratio of $\theta_m=1.21$. The coefficient of variation of modelling $V_\theta=6.6\%$ implies a small scatter of the results, also illustrated in Figure 7.10. The low coefficient of variation implies a stable solution strategy for use on structural walls in general, though the observed effects and limitations discussed in chapter 6 consequently leads to a large bias in the solution strategy.

Table 7.3: The estimated modelling uncertainty in terms of θ_m and V_θ .

Wall specimen	Normalised axial load $\nu \simeq \frac{F_v}{btf_{cm}}$	Ultimate load NLFEA R_{um} [kN]	Ultimate load experiment R_{exp} [kN]	Ratio $\theta = \frac{R_{exp}}{R_{um}}$
SW11	0.0	227.2	260	1.14
SW12	0.1	274.4	340	1.24
SW13	0.2	251.5	330	1.31
SW21	0.0	108.0	127	1.18
SW22	0.1	131.5	150	1.14
SW23	0.2	137.7	180	1.31
θ_m				1.21
V_θ				6.6 %
$\gamma_{Rd,log}$ (unbiased)				0.90 (1.08)
$\gamma_{Rd,student}$ (unbiased)				0.91 (1.10)

The safety formats ECOV and the safety format by Schlune et.al, are based on an assumption of a lognormal distribution of the resistance, where θ_m is the mean value. For small data sample sizes, an improved approach may be a student t-distribution. The modelling uncertainty factors γ_{Rd} are derived in Table 7.3 using the two statistical approaches by formulas provided by Kadlec and Cervenka [3]. This allows for an isolation of the modelling uncertainty into *one* factor, that can be directly compared with the modelling uncertainty factor provided in *fib* Model Code 2010 for ECOV. Note that the estimation of the modelling uncertainty factor γ_{Rd} admits a higher probability of failure than for material uncertainties due to the assumption of a non-dominant description of the model uncertainty by reducing the sensitivity factor of resistance to $\alpha_R=0.4*0.8=0.32$ [3]. The biased estimation of γ_{Rd} results in values less than 1.0 that indicates conservative analysis results that further indicates a poor-validated model, where a very large bias generates a non-conservative modelling factor.

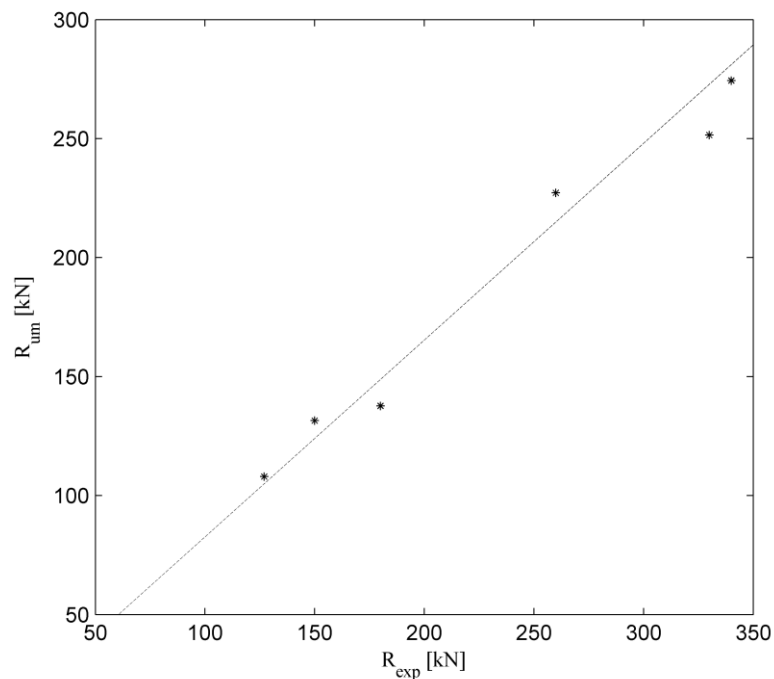


Figure 7.10: Experimental load R_{exp} to NLFEA R_{um} result from six walls, results summarized in Table 7.3. Mean ratio θ_m as dotted line.

8 Structural safety assessment of a structural wall

Redistribution of capacity within the structure might be inevitable to fulfil safety requirements for existing structures or to avoid conservative and expensive calculations of new structures. NLFEA in a design and safety assessment aspect requires incorporation of a suitable safety format to the ultimate load capacity R_{um} with mean material parameters, to predict the design load capacity R_d .

The wall specimens tested experimentally by Lefas et.al are scaled down in dimensions compared to realistic structure sizes [9]. Ideally, a full-scale experimental test on a structural wall would serve as the better approach for a structural safety assessment with NLFEA. Literature searches revealed that other relevant structural wall experiments were also either scaled with some factor, or were a part of larger structural systems. A continuation with a safety assessment of the wall specimen SW21 tested by Lefas et.al was reasonable, since the selected solution strategy for this specific structure is well interpreted and studied during the part II and chapter 7.

8.1 Assessment by an analytical method: Strut-and-tie modelling

Eurocode 1992-1-1 (EC2) suggests the use of a plastic analysis method for ultimate limit state design, based on a lower bound theorem of plasticity [13]. The standard formulas in EC2 for structural parts in shear does not apply for discontinuity regions, and a solution method by strut-and-tie models is recommended for design of such regions by EC2. Plane strain distribution according to Bernoulli's hypothesis is assumed not valid and a strong nonlinear distribution of strains is expected in discontinuity regions. Lateral strains are expected in structural walls, and were confirmed in the case study, and large discontinuities at the compressive toe were observed. The wall specimen SW21 was treated as a discontinuity region and a strut-and-tie model developed. The location and direction of the struts should follow linear theory of elasticity, while the ties follow the location and direction of the actual tensile reinforcement in the structure [13]. Sufficient anchorage of

the wall to the foundation was assumed fulfilled, and the tensile capacity was assumed provided by the reinforcement alone.

8.1.1 Strut-and-tie models

The design load capacity was evaluated by strut-and-tie modelling according to point 6.5 in EC2 [13]. In an attempt to assess the uncertainty in the analytical method, *two* strut-and-tie models were used for the calculation of the analytical design load capacity of SW21, presented in Figure 8.1 by STM1 and STM2. The strut-and-tie models were sensitive to assumptions regarding the distribution of the tensile zone, defined by the assumed number of reinforcement bars in pure tension, and the following location of F_T along the wall width. An increasing number of bars in tension reduces the internal moment arm z and increases the angle θ , which again limits the compression zone width x . For a correct moment arm to the critical compressive toe and for direct comparison to the numerical modelled SW21 wall specimen, the load was applied as a point load in the middle of a supplementary concrete area, similar to the upper beam in the finite element model. The reinforcement layout in Figure 4.2(a) provided the location and amount of reinforcement in the structure.

The design load capacity R_d is set equal to the applied horizontal load F_H , which is the unknown quantity, with use of design material parameters calculated according to EC2 with partial safety factors $\gamma_c=1.5$ and $\gamma_s=1.15$ [13]. The width of the struts between the joints are unknown, and likely to be larger than at the joints. In addition to a global capacity and equilibrium control, the STM capacity was checked at all joints with reduced concrete design strengths according to EC2 6.5.4, dependent on the connection of struts and ties in multiple directions. The compressive zone was assumed uniformly distributed over a width x , and F_c calculated with reduced concrete strength for joints connecting struts only. Detailed calculations of the two strut and tie models are enclosed in Appendix E.

8.1.2 Results from the strut-and-tie models

The global equilibrium was governed by F_T , which is dependent on the assumed number of vertical reinforcement bars in tension. This limited the design capacity for both the strut-and-tie models, with a maximum capacity with a number of six rows of vertical bars in pure tension, which implies 12 bars. The design load capacity was thus calculated to $R_{d, STM1} = R_{d, STM2} = R_{d, STM} = 62.2$ kN, with input variables summarized in Table 8.1 supported by

8.1 Assessment by an analytical method: Strut-and-tie modelling

Figure 8.1. Due to the governing global equilibrium, only the angle θ differs between the two STM in Table 8.1.

Table 8.1: Strut-and-tie model calculation summary for both STM, input variables defined in Figure 8.1.

	Value	Unit
$R_{d, STM} = F_H$	62.2	kN
$F_C = F_T$	246.5	kN
x	266.0	mm
z	347.0	mm
s	170.0	mm
θ_{STM1}	75.8	degrees
θ_{STM2}	63.2	degrees

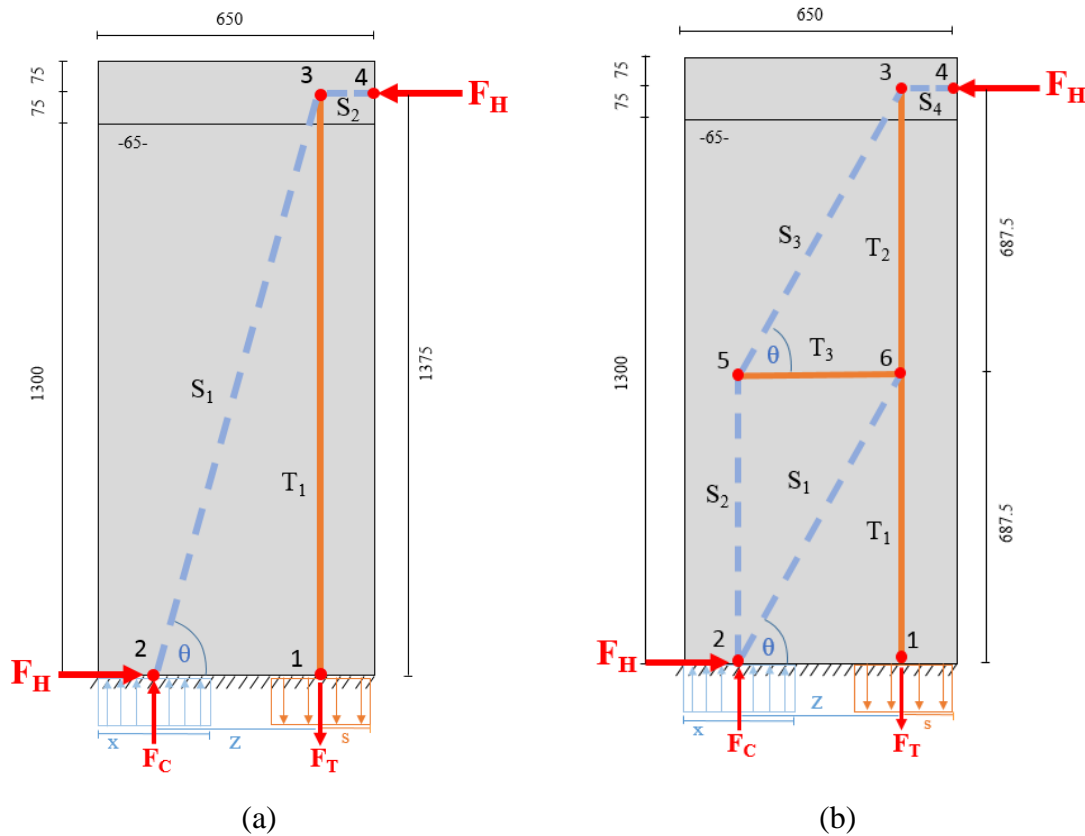


Figure 8.1: Strut-and-tie model for SW21, all measures in mm. (a) Single frame STM1 and (b) double frame STM2. Illustrative dimensions of x , s , z and θ , see Table 8.1.

8.2 Assessment with NLFEA with safety formats

The selected solution strategy used on the wall specimen SW21 defines the 3D base model examined in Part II, and is used throughout the structural safety assessment with NLFEA. The assessment is performed during an evaluation of the four safety formats presented in section 2.5 with focus on the inclusion of the modelling uncertainty and the resulting effect to the design load capacity. The estimated modelling uncertainty in section 7.3 is directly included into the new safety format by Schlune et.al. *fib* Model Code 2010 allows for a higher modelling uncertainty factor $\gamma_{Rd} \geq 1.06$ for low-level model validations in ECOV [1]. The used specified value $\gamma_{Rd} = 1.06$ implies a value of $V_{\theta} = 4.9\%$ for an unbiased approach, using the lognormal formula by Kadlec [3].

8.2.1 Material parameters in the safety formats

Estimated material parameters for the four safety formats are presented in Table 8.2 and Table 8.3. Except for the safety format by Schlune et.al, the material parameters were calculated by formulas in section 2.5 and DG [8]. *Mean DG* implies the mean material parameters used in the previous analyses. The updated hardening diagrams for the reinforcement for all the safety formats are based on the yield stress values in Table 8.3 and h_R defined in section 4.2.4 and Figure 4.11(b).

Material parameters in the new safety format by Schlune et.al

Schlune et.al suggest two additional nonlinear analyses to assess the material uncertainty V_f by use of a reduced concrete compressive strength $f_{\Delta c}$ and reduced steel yield strength $f_{\Delta y}$ respectively. The resulting material parameters are presented in Table 8.2 and Table 8.3. The provided concrete strength f_{cm} from the experimental report is interpreted as an in-situ value, and no further reduction was applied. For estimation of the reduction Δf_i by formula 2.7, the coefficients of variations $V_{fc} = 0.15$ for concrete, $V_{fs} = 0.04$ for steel and $V_g = 0.05$ for the geometrical uncertainty for both concrete and steel dimensions were used. These values are given by Schlune et.al, and referred to as underlying values for the partial safety factors in EC2 [4, 13]. The variances in formula 2.9 were calculated as $\sigma_{fc}^2 = (V_{fc} f_{cm})^2$ and $\sigma_{fy}^2 = (V_{fs} f_{ym})^2$, and the estimated $V_{\theta} = 0.066$ from Table 7.3 was used. Three different reinforcement bar diameters and yield strengths were used in the wall. The three reduced steel strengths in Table 8.3 were implemented into one NLFEA, and the final material uncertainty in formula 2.9 consisted of four components with resulting value $V_f = 0.066$. The

variation of material parameters used in the safety formats and for estimation of V_f is illustrated in Figure 8.2. The same values for the reliability index and sensitivity factor as for ECOV is used, by $\beta=3.8$ and $\alpha_R=0.8$ [1].

Table 8.2: Concrete material parameters for use in safety formats in section 2.5.

Concrete material parameter	Mean DG	Char.	GRF	PSF	Schlune et.al reduced $f_{\Delta c}$	Unit
Compressive strength f_c	36.38	28.38	24.12	17.85	26.35	MPa
Tensile strength f_t	2.81	2.25	1.93	1.42	2.10	MPa
Tensile fracture energy G_F	0.0741	0.0623	0.0556	0.0450	0.0591	Nmm/mm ²
Compressive fracture energy G_C	18.52	15.57	13.89	11.25	14.78	Nmm/mm ²
Reduced Young's modulus E_C	28761	26476	25079	22250	25829	MPa
Poisson's ratio ν	0.15	0.15	0.15	0.15	0.15	-

Table 8.3: Reinforcement steel yield stress for use in safety formats in section 2.5 in [MPa].

Reinforcement bar diameter	Mean DG f_{ym}	Char. f_{yk}	GRF $f_{ym,GRF}$	PSF f_{yd}	Schlune et.al reduced $f_{\Delta y}$
4 mm	430	420	462.0	344.5	394.6
6.25 mm	530	520	572.0	426.6	486.3
8 mm	480	470	517.0	385.6	440.4

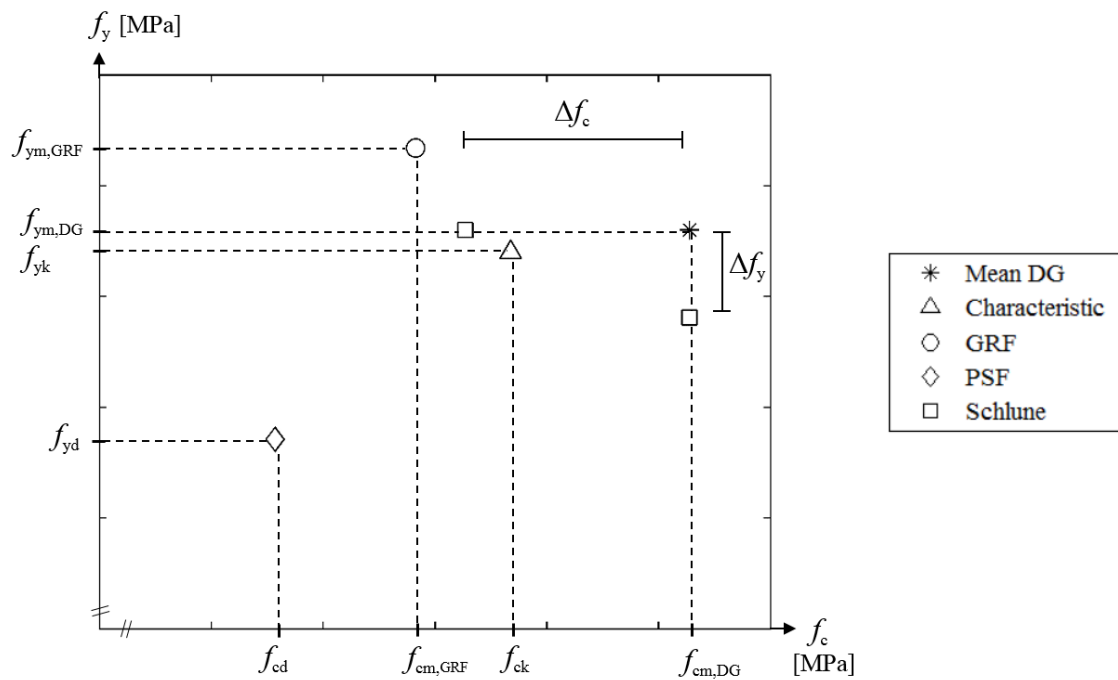


Figure 8.2: Material sampling points for the evaluated safety formats, values from Table 8.2 and Table 8.3.

8.2.2 Results from NLFEA with safety formats

The material parameters presented in Table 8.2 and Table 8.3 were applied to the SW21 wall specimen using the selected solution. The ultimate design load capacity of the structural wall was assessed with NLFEA using the presented safety formats with results presented in Table 8.4. For a better direct comparison, an additional unbiased approach of Schlune et.al was run with resulting $R_d=78.3$ kN with $\gamma=1.38$ referring to Table 8.4.

Table 8.4: Predicted design load capacity R_d for the four safety formats and global reduction compared to $R_{um}=108.0$ kN.

	Design load capacity R_d [kN]	$\gamma = \frac{R_{um}}{R_d}$
PSF	76.2	1.42
GRF	77.8	1.39
ECOV	88.0	1.23
Schlune et.al	94.7	1.14

8.2.3 Study of the effect of the modelling uncertainty

The new safety format by Schlune et.al is the only evaluated safety format that allows for an explicit inclusion of the estimated modelling uncertainty by V_θ and θ_m . The effect of these parameters to the design load capacity at hand is assessed in a small sensitivity study, summarized in Table 8.5 and Table 8.6 and visualized in Figure 8.3. Note that the presented study decouples two coupled parameters, to visualize the *effect* of these parameters to the design capacity. V_R and γ_R are defined in section 2.5.4. A smaller bias would probably also imply a larger R_{um} and hence increased design load capacity compared to the values illustrated in Figure 8.3.

Table 8.5: Schlune et.al new safety format sensitivity to V_θ , with constant $\theta_m=1.21$.

	V_θ	V_R	γ_R	R_d
	[%]	[%]		[kN]
	0	8.28	1.06	101.6
<i>Actual -</i>	6.6	10.6	1.14	94.7
	15	17.1	1.39	77.6
	20	21.6	1.60	67.6
	30	31.1	2.13	50.7

Table 8.6: Schlune et.al new safety format sensitivity to θ_m , with constant $V_\theta=6.6\%$.

	θ_m	γ_R	R_d
	[%]		[kN]
	1.30	1.06	101.8
<i>Actual -</i>	1.21	1.14	94.7
	1.00	1.38	78.3
	0.85	1.62	66.6
	0.70	1.97	54.8

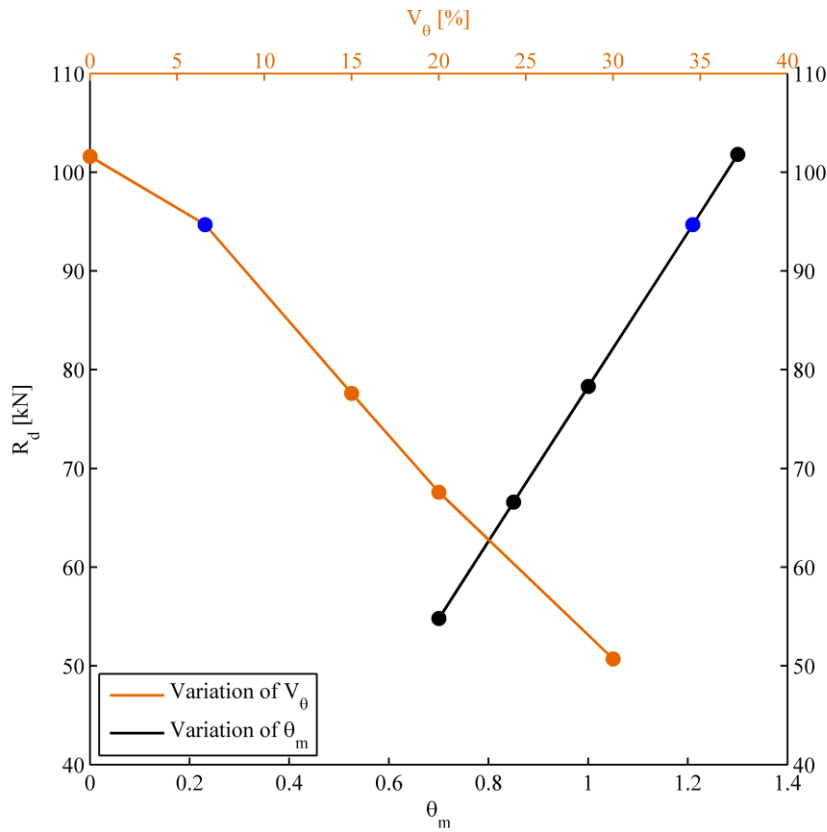


Figure 8.3: Sensitivity to the modelling uncertainty in the new safety format by Schlune et.al. Uncoupled curves, actual value marked blue. Results from Table 8.5 and Table 8.6.

8.3 Summary of results from the structural safety assessment

The estimated design load capacities in relation to the experimental load capacity are visualized in Figure 8.4. *DG* equals the solution strategy with no safety format included, and *STM* is the design capacity found in section 8.1 by the strut-and-tie modelling. All the safety formats provide design load capacities greater than the analytical method, though still conservative if compared to the experimental load capacity. The biased modelling approach in the new safety format by Schlune et.al results in a high design load capacity compared to the other safety formats evaluated. The two safety formats providing the highest design capacity, ECOV and Schlune et.al, both assesses the material uncertainty V_f by one or two additional nonlinear analyses with altered material parameters, and the latter format in addition corrects for an estimated bias. PSF, GRF and an unbiased Schlune et.al method show similar results, indicating the same uncertainty level is included. The low material parameter values in PSF in this case provides the same failure mode as observed

in section 5.1. The new safety format by Schlune et.al indicates to be non-conservative in this case, due to the substantial bias correction that increases the unbiased capacity by 21%. The high design load capacity by ECOV compared to the other safety formats could indicate a low uncertainty level, if disregarding the bias correction in Schlune et.al.

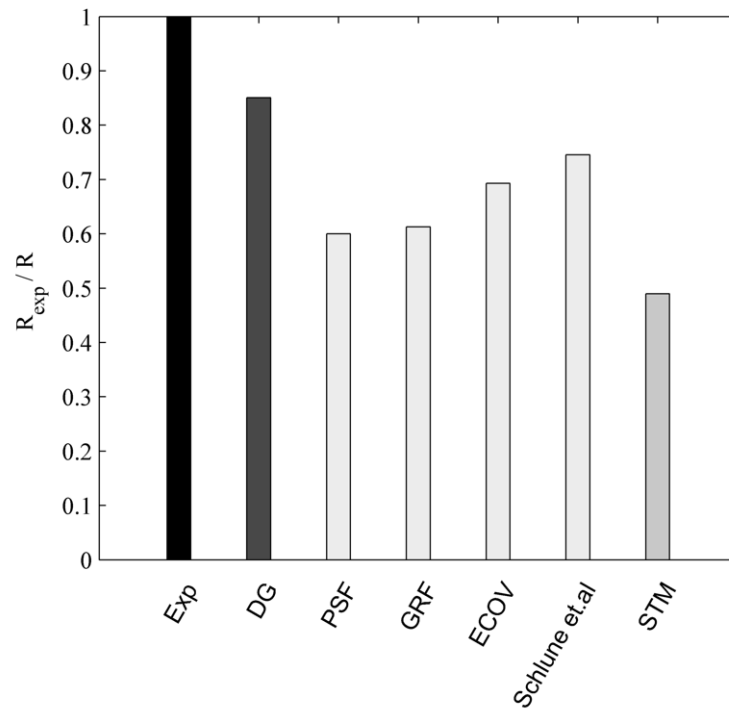


Figure 8.4: Experimental load capacity R_{exp} as ratios of the mean ultimate load capacity R_{um} and the design load capacities R_d . Results from Table 8.1 and Table 8.4.

9 Discussion of results – the modelling uncertainty and structural safety assessment

9.1 Estimation of the modelling uncertainty

9.1.1 General results and model validation

The six wall specimens analysed in chapter 7 showed a similar behaviour as observed for the 3D base model in PART II. The selected solution strategy resulted in a similar underestimation of the ultimate load capacity in the wall specimens with varying geometry, concrete material strengths and applied loading, illustrated by the low coefficient of variation of modelling $V_{\theta}=6.6\%$. The structural stiffness prediction at low load levels was worsened with additional axial loading, illustrated in Figure 7.3. The estimated mean ratio of $\theta_m=1.21$ implies a systematic error in the model, and confirms the deficiencies observed in section 5.1.

Schlune et.al provide values of the modelling uncertainty from experiments on shear panels by mean ratios $\theta_m \approx 0.73-1.05$ and coefficient of variations of the modelling $V_{\theta} \approx 16-39\%$ [4]. Kadlec and Cervenka state that a mean ratio far from a unit value implies a non-validated model, and should be dismissed or at least used with care [3]. The estimated low coefficient of variation of the modelling in section 7.3 may be explained by similar structures analysed in the same FEA software and with minimal variations within the used solution strategy.

The estimated modelling uncertainty implies a conservative and stable application to multiple structural walls, though confirms the poor prediction of the ultimate load capacity. Supported by the observed effects and limitations in chapter 6 caused by the solution strategy, the FEA software, or both, the solution strategy based on the recommendations by DG should not be considered validated for use on structural walls in general, built on the results from this study solely.

9.1.2 Similar studies

The selected solution strategy is evaluated only for structural walls, and the resulting modelling uncertainty can only be compared with similar studies. Vecchio investigated the effect of the concrete expansion modelling with use of the 13 wall specimens tested by Lefas et.al, modelled with smeared reinforcement and by another FEA software [31]. Extracting Vecchios results for the same wall specimens as tested in section 7.2 resulted in $\theta_m=1.02$ and $V_\theta =6.5\%$ with concrete expansion modelled and $\theta_m=1.14$ and $V_\theta=7.3\%$ without expansion modelled. The latter is in quite good correlation with the results in this present study, also indicating a low-validated model with a great improvement after inclusion of the concrete expansion effects illustrated in Figure 3.5(b). These results also support the presumed limitation discussed in section 6.1.2 regarding the lacking volumetric concrete expansion modelling.

9.1.3 Sample size and the modelling uncertainty factor

The dataset provided by the six structural wall specimens is small, and any general conclusions may therefore not be drawn solely based on these results. The difference between γ_{Rd} estimated by the two methods in Table 7.3 indicates a somewhat small data set. Kadlec and Cervenka denotes a dataset of ten or less samples as small, and further recommend the use of t-student distribution [3]. Hence, the method of estimating γ_{Rd} in Table 7.3 by student t-distribution is the most correct value by this definition, resulting in an unbiased value of $\gamma_{Rd}=1.10$. The modelling uncertainty factor included in the structural safety assessment with the safety format by Schlune et.al are assumes a lognormal distribution and thus the unbiased value $\gamma_{Rd}=1.08$.

9.2 Structural safety assessment

9.2.1 General results

All the evaluated safety formats provided design load capacities greater than the analytical method by strut-and-tie modelling, confirming a capacity enhancement utilizing NLFEA. Confinement effects and redistributions of internal stresses during loading is likely to be main contributors to the difference, as these effects are not included in a strut-and-tie model. PSF is referred to as a safe approach [1], which is confirmed as the lowest estimate of R_d in Figure 8.4. PSF, GRF and Schlune et.al without bias correction generated similar design capacities, indicating a comparable amount of global uncertainty included for this case.

Comparison of the unbiased design capacities from the four safety formats identifies a significant elevated capacity estimated by ECOV that may indicate a low level of included uncertainties, or too conservative approaches by the other formats.

9.2.2 Reliability level and inclusion of the modelling uncertainty

The three safety formats in *fib* Model Code 2010 include a predefined value of $\gamma_{Rd}=1.06$ and do not account for bias on the results from NLFEA. This value is smaller than the estimated unbiased values of γ_{Rd} in Table 7.3, and the recommendation by *fib* Model Code 2010 regarding an increased value in ECOV for poor-validated models should be succeeded for this case. Schlune et.al state that safety formats that do not account for bias, and in addition overestimates the design capacity, will result in a reliability level lower than intended [4]. The new safety format by Schlune and ECOV should provide the same reliability level, based on the assumed lognormal distribution and same input values of the reliability index and sensitivity factor. The results in Figure 8.4 however reveal unequal design capacities. Schlune et.al report good conformity to the target reliability for beams in bending with the new safety format [4] and Pimentel et.al recommend use of the new safety format by Schlune et.al prior to ECOV by based on a reliability level closer to the target reliability level [12]. The attained reliability index β should be assessed for the various safety formats prior to drawing conclusions and making recommendations regarding a preferred general application, e.g. by Monte-Carlo simulations to estimate the probability of exceedance of the predicted design capacity.

9.2.3 The influence of the modelling uncertainty

The illustrative design capacities in Figure 8.3 visualize the importance of including correct values for the modelling uncertainty when performing a structural safety assessment with NLFEA, to avoid design capacities with reliability level far from the intended. The coefficient of variation V_R is independent of the bias, and Table 8.5 illustrates the large influence of V_θ to this parameter. A coefficient of variation of the modelling $V_\theta=20\%$ is stated by Pimentel et.al to be an upper limit value for modelling uncertainty to be accepted in any solution strategy for NLFEA on concrete structures, and that a value above this violates of the model validation process [12]. Correction of bias may overcome else conservative design capacities, or non-conservative capacities for $\theta_m \leq 1.0$, though only within limits of a well-validated model. When utilizing safety formats that allow for direct inclusion of estimated values of the modelling uncertainty, bounds should be defined for

9 DISCUSSION OF RESULTS – THE MODELLING UNCERTAINTY AND STRUCTURAL SAFETY ASSESSMENT

θ_m and V_θ to secure reliable design capacities. Such boundaries should be based on a study of the actual achieved reliability level.

PART IV: CONCLUSIONS AND
RECOMMENDATIONS FOR
FURTHER WORK

10 Conclusions

The thesis reveals an occurrence of a prominent modelling uncertainty, quantified by a mean ratio of the experimental to predicted strength $\theta_m=1.21$ and the coefficient of variation of the modelling $V_\theta=6.6\%$, that limits the benefit of the use of NLFEA in structural safety assessment greatly, and implies a poor validated model.

Indicated shortages within the constitutive modelling result in a low prediction of the ultimate load capacity of the structural walls. The volumetric concrete expansion effect, the post-peak concrete compressive behaviour and the poor observed structural stiffness prediction are designated as likely limitations in the selected solution strategy applied to structural walls in DIANA 9.6. Use of solid elements were necessary in this case, for reproduction of a critical triaxial stress state. The modelling uncertainty's dependency on the selected solution strategy and FEA software is underlined during this evaluation.

The evaluated global safety formats provide design capacities exceeding the analytical design capacity, though they are conservative approaches compared to the experimentally tested load capacity. ECOV and the new safety format by Schlune et.al provide the highest design load capacities, where the importance and difficulty of handling bias in the results is draw attention to in the latter format. Bias correction in this case proves effective to outweigh inaccuracies generated by the selected solution strategy, though providing an unclear reliability level that needs further assessment. The safety formats in *fib* Model Code 2010 include a prescribed low modelling uncertainty factor, and do not account for bias in the results that proves to have a significant effect on the design capacity in this study. A standardized value of the modelling uncertainty based only unbiased results will only be accurate for certain cases, and may not appraise a well-validated model nor a poor-validated model sufficiently. The observed occurrence of the modelling uncertainty in this study supports the inclusion of bias correction to the safety formats, this is especially important for cases where the experimentally tested capacities are overestimated. Clear boundaries for acceptable values of the modelling uncertainty in a design aspect need to be defined to ensure reliability.

The evaluated set of analyses in this thesis is limited, and the validity of the results in a broader application should be examined and supported by additional research. This study however emphasizes the importance of model validation, with a critical approach to the development of a solution strategy, and choice of FEA software, to limit the modelling uncertainty introduced to the structural safety assessment procedure. Recommendations for further work are provided in the following chapter.

11 Recommendations for further work

The indicated limitations within the constitutive modelling observed in the case study should be addressed before the selected solution strategy can be validated for structural walls in general. Inclusion of the selected solution strategy in an alternative FEA software that provides volumetric expansion modelling of concrete can directly settle the probable importance of this effect, and can serve as a point of departure for the further model validation process. Further studies to the parabolic compressive curve in DIANA should be performed to assess if improvements are necessary. A lower bound for the post-peak stress level and increase of the peak strain and the compressive fracture energy G_C in confined concrete are relevant effects to assess on basis of the observations in this study. A non-orthogonal crack model such as the multi-directional crack model can assess the influence of the orthogonal crack models to the structural walls stiffness. A full three-dimensional material model for the concrete behaviour could reproduce an enhanced structural behaviour with a more suitable approach to the triaxial stress behaviour in concrete.

The acquired reliability index should be examined for all the safety formats, also to assess if the additional analysis costs by ECOV and Schlune et.al provide the anticipated profit related to the structural safety assessment. A biased approach in the safety formats is recommend based on this study, and for a reliable use, boundary conditions based on a study of the actual achieved reliability level should be defined. Clearer limits for what are acceptable values of the modelling uncertainty and how to manage it in a design procedure should be attempted generalized and provided for guiding of future users. Instructive boundaries of acceptable values for the modelling uncertainty based on further studies similar to this study on various structural types, failure modes, solution strategies and FEA softwares, would increase the ability to understand and handling the modelling uncertainty. Specified guidelines validated for certain structural types, and verified as software-independent, could ideally include instructive values of the expected modelling uncertainty.

References

1. *fib. fib Model Code for Concrete Structures 2010*. Ernst & Sohn. 2013.
2. Allaix D.L., Carbone V.I., Mancini G. Global safety format for non-linear analysis of reinforced concrete structures. *Structural Concrete*. 2013;14(1):29-42.
3. Kadlec L., Cervenka V. Uncertainty of numerical models for punching resistance of RC slabs *fib Symposium Copenhagen; 2015*
4. Schlune H., Plos M., Gylltoft K. Safety formats for non-linear analysis of concrete structures. *Magazine of Concrete Research*. 2012;64(7):563-74.
5. Engen M., Hendriks M.A.N., Øverli J.A., Åldstedt E. Solution strategy for non-linear Finite Element Analyses of large reinforced concrete structures. *Structural Concrete 2015*.
6. Cervenka V. Reliability-based non-linear analysis according to *fib Model Code 2010* *Structural Concrete 2013*;14(1):19-28.
7. Schlune H., Plos M., Gylltoft K. Safety formats for nonlinear analysis tested on concrete beams subjected to shear forces and bending moments. *Engineering Structures*. 2011;33(8):2350-6.
8. Hendriks M.A.N., den Uijl J.A., de Boer A., Feenstra P.H., Belletti B., Damoni C. Guidelines for Nonlinear Finite Element Analysis of Concrete Structures. RTD 1016:2012, Technical report: Rijkswaterstaat – Ministerie van Infrastructuur en Milieu, 2012.
9. Lefas I.D., Kotsovos M.D., Ambraseys N.N. Behavior of reinforced concrete structural walls. Strength, deformation characteristics, and failure mechanism. *ACI Structural Journal*. 1990;87(1):23-31.
10. Mathisen K.M. Lecture 1: Introduction to nonlinear FEA. Lecture notes TKT4197 Nonlinear FEM. Trondheim: NTNU, Department of Structural Engineering; 2014.
11. Engen M., Hendriks M.A.N., Øverli J.A., Åldstedt E. Application of NLFEA in the Design of Large Concrete Structures. *Proceedings of the XXII Nordic Concrete Research Symposium; Reykjavik, Iceland. 2014*.
12. Pimentel M., Brühwiler E., Figueiras J. Safety examination of existing concrete structures using the global resistance safety factor concept. *Engineering Structures*. 2014;70:130-43.
13. Standard Norge. NS-EN 1992-1-1:2004+NA 2008: Eurocode 2: Design of concrete structures Part 1-1: General rules and rules for buildings. CEN; 2008.

14. Vecchio F.J. Non-linear finite element analysis of reinforced concrete: At the crossroads? *Structural Concrete*. 2001;2(4):201-12.
15. *fib*. Bulletin 45: Practitioners' guide to finite element modelling of reinforced concrete structures. International Federation for Structural Concrete (*fib*). 2008.
16. Standard Norge. NS-EN 1992-2:2005+NA 2010: Eurocode 2: Design of concrete structures Part 2: Concrete bridges. Design and detailing rules. CEN; 2008.
17. *fib*. Bulletin 70: Code-type models for structural behaviour of concrete. Background of the constitutive relations and material models in the *fib* Model Code for Concrete Structures 2010. International Federation for Structural Concrete (*fib*). 2013.
18. Broo H., Lundgren K., Plos M. Guide to non-linear finite element modelling of shear and torsion in concrete bridges. Göteborg, Sweden: Department of Civil and Environmental Engineering, Division of Structural Engineering, Concrete Structures, Chalmers University of Technology, 2008.
19. JCSS. Probabilistic Model Code. Zurich: Joint Committee on Structural Safety,; 2001.
20. Bažant Z.P., Planas J. Fracture and size effect in concrete and other quasibrittle materials: CRC Press LLC; 1998.
21. Mier J.G.M.v. Concrete fracture: a multiscale approach. Boca Raton, Fla.: CRC Press; 2013.
22. Bažant Z.P., Oh B.H. Crack band theory for fracture of concrete. *Matériaux et Constructions*. 1983;16(3):155-77.
23. Rots J.G., Blaauwendraad J. Crack models for concrete: discrete or smeared? Fixed multi-directional or rotating? *Heron*. 1989;34(1):3-59.
24. TNO DIANA. DIANA User's Manual Material Library Release 9.6. 2015.
25. Vecchio F.J., Collins M.P. Modified compression-field theory for reinforced concrete elements subjected to shear. *Journal of the American Concrete Institute*. 1986;83(2):219-31.
26. Slobbe A.T., Hendriks M.A.N., Rots J.G. Sequentially linear analysis of shear critical reinforced concrete beams without shear reinforcement. *Finite Elements in Analysis and Design*. 2012;50:108-24.
27. González-Vidoso F., M.D. K., M.N. P. On the numerical instability of the smeared-crack approach in the non-linear modelling of concrete structures. *Communications in Applied Numerical Methods*. 1988;6(4):799-806.
28. Selby R.G., Vecchio F.J. Three-dimensional constitutive relations for reinforced concrete. Toronto: University of Toronto, Department of Civil Engineering; 1993.

29. Kotsovos M.D. Consideration of Triaxial Stress Conditions in Design: A Necessity. *Structural Journal ACI*. 1987;84(3).
30. Hanjari K., Kettil P., Lundgren K. Modelling the structural behaviour of frost-damaged reinforced concrete structures. *Structure and Infrastructure Engineering: Maintenance, Management, Life-Cycle, Design and Performance*. 2013;9(5):416-31.
31. Vecchio F.J. Finite element modeling of concrete expansion and confinement. *Journal of structural engineering* New York, NY. 1992;118(9):2390-406.
32. Stene Pettersen J. Non-Linear Finite Element Analyses of Reinforced Concrete with Large Scale Elements [Master's Thesis]. Trondheim: Norwegian University of Science and Technology, Department of Structural Engineering; 2014.
33. TNO DIANA. DIANA User's Manual Theory Release 9.6 2015.
34. Lackner R., H.A. M. Scale transition in steel-concrete interaction I: Model. *Journal of Engineering Mechanics*. 2003;129(4):393-402.
35. TNO DIANA. DIANA User's Manual Element Library Release 9.6. 2015.
36. Øverli J.A. TKT4222 Concrete Structures 3. Trondheim: Department of Structural Engineering, NTNU; 2014.
37. Hopperstad O.S., Børvik T. Lecture Notes Material Mechanics Part 1 Trondheim: Structural IMPact Laboratory; 2013.
38. Mathisen K.M. Lecture 3: Adaptive solution algorithms. Lecture notes TKT4197 Nonlinear FEM. Trondheim: NTNU, Department of Structural Engineering; 2014.
39. Mathisen K.M. Lecture 2: Solution of nonlinear equilibrium equations. Lecture notes TKT4197 Nonlinear FEM. Trondheim: NTNU, Department of Structural Engineering; 2014.
40. TNO DIANA. DIANA User's Manual Analysis Procedures Release 9.6. 2015.
41. Kotsovos M.D., Newman J.B. Behavior of Concrete Under Multiaxial Stress. *Journal Proceedings*. 1977;74(9):443-6.

APPENDICES

Contents Appendices

A.	Preliminary analyses	A-1
A.1	Type II wall	A-1
A.2	Type I wall	A-3
B.	Model geometry	B-1
B.1	Lower beam in 2D model	B-1
B.2	Lower beam in 3D model	B-2
C.	Crack spacing calculations	C-1
C.1	Type I wall	C-1
C.2	Type II wall	C-3
D.	Parabolic compression curve in DIANA	D-1
E.	Strut-and-tie modelling of SW21	E-1
E.1	Design capacity of STM1	E-3
E.2	Design capacity of STM2	E-4
F.	Analysis files from DIANA 9.6	F-1
F.1	Data input file for SW22	F-1
F.2	Analysis command file with phased analysis for SW22	F-5
F.3	Analysis command file for SW21: 3D base model	F-7
	References in appendices	G-1

A. Preliminary analyses

An estimate of the horizontal displacement of an unreinforced concrete wall with modulus of elasticity $E=30\,000$ MPa and Poisson's ratio $\nu=0.15$ was calculated by unit load method, with shear and flexural deformation included. The walls were simplified as clamped beams subjected to a point load as illustrated in Figure A.1. The formulas and theory used for the unit load method calculations are from [A1]. The simplification includes Bernoulli beam theory that states that plane cross sections remain plane. Inclusion of shear deformation should regard these effects. Illustration of the internal stress distribution is given in Figure A.2 for the three analyses with the selected finite element sizes.

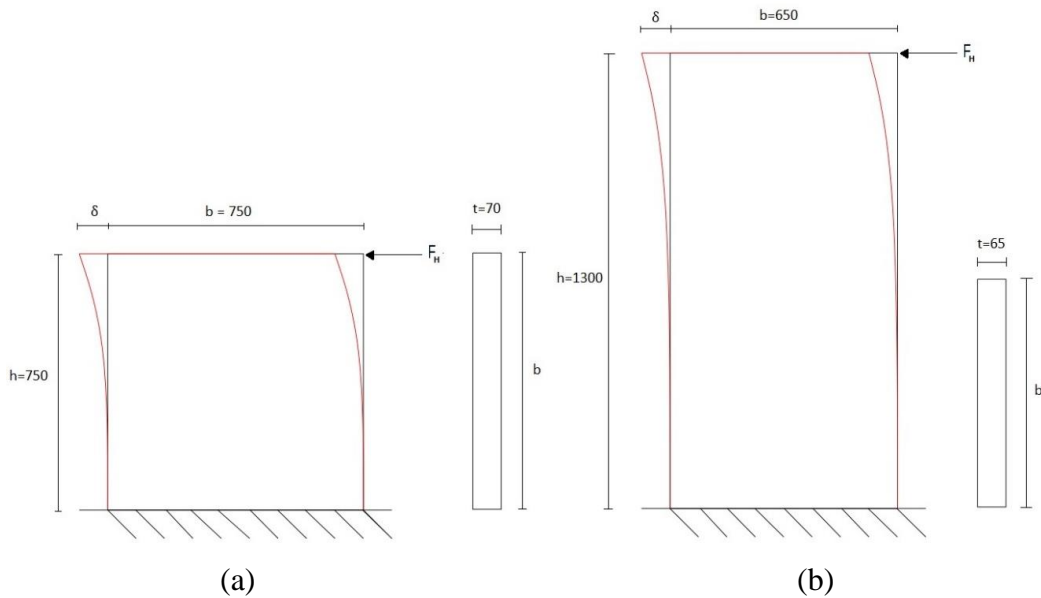


Figure A.1: Simplification of (a) type I and (b) type II wall for use in analytical calculations. Dimensions in mm.

A.1 Type II wall

A type II wall with no axial loading analysed using LFEA. A horizontal load $F_H = 80$ kN was applied, and results from the analytical method and LFEA compared in Table A.1 for plane stress elements and Table A.2 for solid brick elements.

Analytical calculation by unit load method

The unit load method with flexural and shear deformation was used with $k_y = \frac{6}{5}$ for a rectangular cross section, elastic shear modulus $G = \frac{E}{2(1+\nu)}$, Poisson's ratio $\nu=0.15$ for concrete and second moment of area $I = \frac{tb^3}{12}$. The predefined formulas for moment and shear effects are defined for ultimate limit effects. The simplified wall geometry is presented in Figure A.1(b) and the total horizontal deformation δ_A at the given load level is derived below.

$$\begin{aligned}\delta_A = \Delta_M + \Delta_V &= \int_0^h \tilde{M} \frac{M}{EI_x} dy + \int_0^h \tilde{V} k_x \frac{V}{GA} dy \\ &\approx F_H \left(\frac{1}{3} h h h \frac{1}{EI} + \frac{6}{5} \frac{h}{GA} \right) = F_H \left(\frac{h^3}{3EI} + \frac{2.76h}{EA} \right) = 1.5390mm\end{aligned}\tag{A.1}$$

Linear static FEA with plane stress elements CQ16M

The horizontal load was applied as a horizontal line load along the upper wall edge. The element type was a plane stress element CQ16M with full Gauss integration. From the results in Table A.1 the model tended to converge towards a solution when applying smaller element sizes that softens the behaviour. The ratio of the linear FEA compared to the hand calculation revealed the simplification of the wall as a beam by prediction both lower and higher results to the analytical calculation.

Linear static FEA with solid brick elements CHX60

The horizontal load was applied as a horizontal surface load directly along the upper wall edge. The finite element type was solid brick elements CHX60 with full Gauss integration. Table A.2 proved a convergence towards a solution when applying smaller element sizes that softened the behaviour. The solid elements showed a stiffer behaviour than the plane stress elements, and underestimated the deflection for all element sizes.

Table A.1: LFEA with plane stress elements of unreinforced concrete wall SW21 subjected to horizontal point load.

Global finite element size [mm*mm]	Horizontal displacement δ_{LFEA} [mm]	δ_{LFEA} / δ_A
32.5*32.5	1.5492	1.0066
65*65	1.5483	1.0060
130*130	1.5462	1.0047
325*325	1.5351	0.9975
650*650	1.4828	0.9635

Table A.2: LFEA with solid elements of unreinforced concrete wall SW21 subjected to horizontal point load.

Global finite element size [mm*mm]	Horizontal displacement δ_{LFEA} [mm]	δ_{LFEA} / δ_A
32.5*32.5*32.5	1.5336	0.9965
65*65*65	1.5329	0.9960
130*130*65	1.5311	0.9949
325*325*65	1.5214	0.9886
650*650*65	1.4756	0.9588

A.2 Type I wall

A type I wall with no axial loading was analysed using LFEA. A horizontal load $F_H = 100$ kN was applied, and results from the analytical method and LFEA are compared in Table A.3 for solid brick elements.

Analytical calculation by unit load method

The same procedure as described in for the Type II wall was used for an analytical calculation of δ_A .

$$\delta_A = \Delta_M + \Delta_V = \int_0^h \tilde{M} \frac{M}{EI_x} dy + \int_0^h \tilde{V} k_x \frac{V}{GA} dy \quad (\text{A.2})$$

$$\approx F_H \left(\frac{1}{3} h h h \frac{1}{EI} + \frac{6}{5} \frac{h}{GA} \right) = F_H \left(\frac{h^3}{3EI} + \frac{2.76h}{EA} \right) = 0.3219 \text{ mm}$$

LFEA of type I wall with solid brick elements

A less stiff behaviour compared to the analytical calculation is observed, with increasing tendency for smaller element sizes. The analytical calculations applicability to a wall with low height to width ratio might be discussable. A convergence towards a stable solution is however visible for smaller finite element sizes.

Table A.3: LFEA with solid elements of unreinforced concrete wall SW11 subjected to horizontal point load.

Global element size [mm*mm*mm]	Horizontal displacement δ_{LFEA} [mm]	δ_{LFEA} / δ_A
37.5*37.5*35	0.3369	1.0466
75*75*70	0.3360	1.0438
150*150*70	0.3340	1.0376
375*375*70	0.3237	1.0056

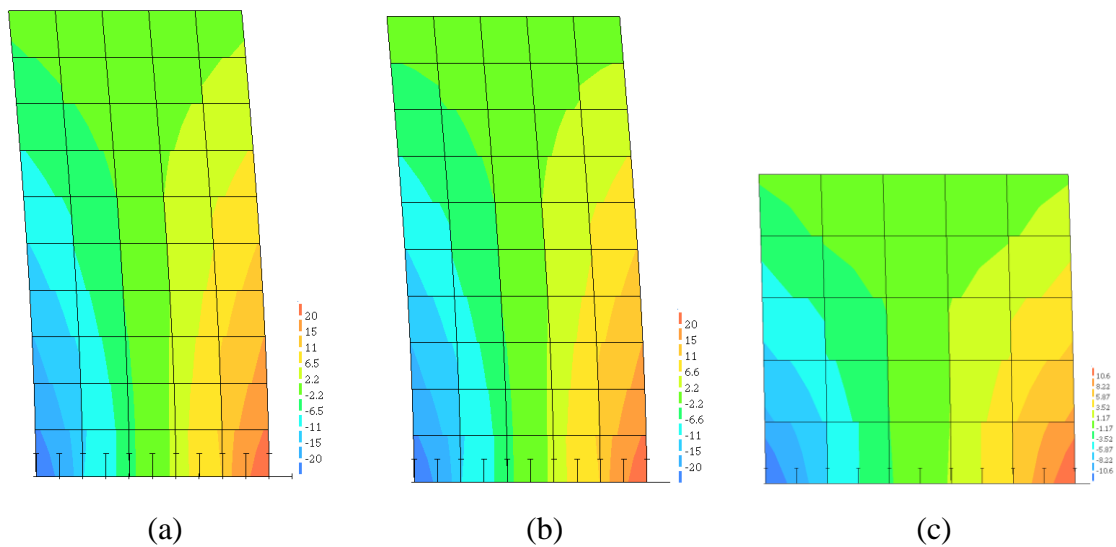


Figure A.2: Vertical stress values with (a) plane stress Type II and (b) solid brick elements Type II and (c) solid brick elements Type I. Deformation factor 50. Linear elastic analyses, illustrates load distribution.

B. Model geometry

The effect of the lower beam implementation to the finite element model was studied. Both linear elastic concrete for pure load transfer and fully reinforced lower beam was examined. The effect was small in both models, with some reduction of ultimate load capacity. The lower beam was thus not included in the base models. The same localization and high values of concrete stresses at the compressive tow as observed in the base models in chapter 5, was observed with the lower beam included.

B.1 Lower beam in 2D model

A full model in 2D with reinforced upper and lower beam was initially tested. The boundary conditions of the lower beam initiating a fixed wall base is illustrated in Figure B.1(a). This lead to lower ultimate load capacity, possibly due to severe cracking of the lower beam. The concrete material in the upper beam needed required modelling with linear elastic concrete for a proper load transfer of the concentrated load and for exerting the documented high stiffness of the beam from the experimental report.

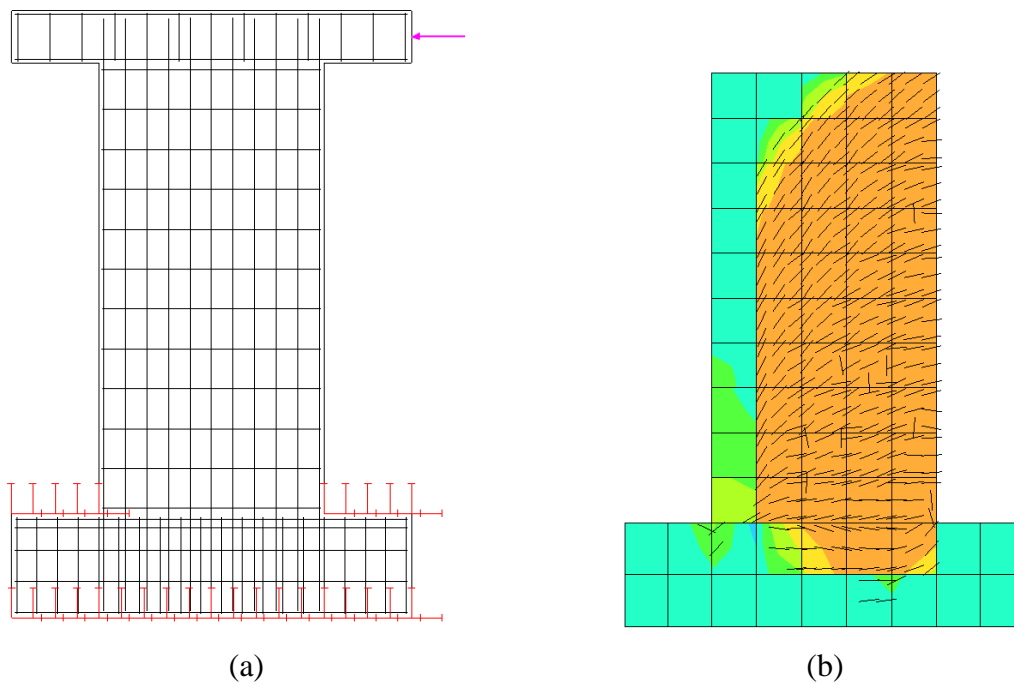


Figure B.1: (a) Fully reinforced lower beam and (b) crack pattern at the first post-peak load step.

The same failure mode and localization of stresses at the compression toe of the wall was observed in all the models.

Table B.1: Ultimate load capacity with various modelling of lower beam in 2D model.

Lower beam	Ultimate load capacity	Displacement at ultimate
	R_{um} [kN]	load capacity [mm]
None, base model	97.70	9.00
Linear elastic	96.90	9.00
Fully reinforced	96.80	9.00

B.2 Lower beam in 3D model

Experiences made in the 2D base model lead to linear elastic upper beam without cantilevers that proved not to affect the global response of the wall. The effect of the same properties of the lower beam was studied in the 3D model.

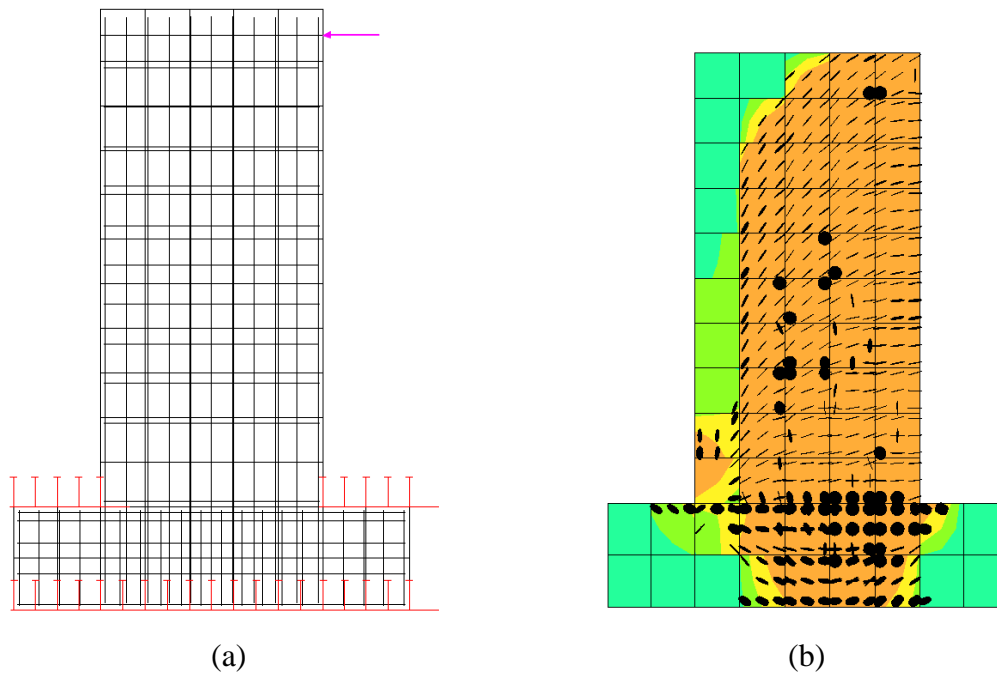


Figure B.2: (a) Fully reinforced lower beam and (b) crack pattern at the first post-peak load step.

A similar localization of stresses and confined concrete stresses was observed with inclusion of the lower beam in the 3D model.

Table B.2: Ultimate load capacity with various modelling of lower beam in 3D model.

Lower beam	Ultimate load capacity R_{um} [kN]	Displacement at ultimate load capacity [mm]
None, base model	108.00	12.00
Linear elastic	107.60	12.00
Fully reinforced	105.10	13.00

C. Crack spacing calculations

The following calculations are in relation with the method and formulas described in section 4.2.4. The resulting modification factors are calculated by a conservative approach of including the shear stirrup reinforcement in the horizontal reinforcement area, which reduces l_{av} and hence increases n_{cr} .

Formulas used in the average crack spacing calculations, presented in section 4.2.4.

- Formula 7.6-4 and Figure 7.6-4(c) in *fib Model Code 2010* [A2].
- Formulas (2.2.4) and (2.2.5) from the compendium in the subject TKT4222 Concrete Structures 3 at NTNU [A3]. A simplification of application of pure shear was used by $N_x=N_y=0$.

Vertical bar diameter $\phi_v := 8 \text{ mm}$

Horizontal bar diameter $\phi_h := 6.25 \text{ mm}$

Shear stirrup bar diameter $\phi_s := 4 \text{ mm}$

Mean horizontal diameter $\phi_m := \frac{(\phi_h + \phi_s)}{2} = 5.13 \text{ mm}$

Assumed concrete cover

$cv := 14 \text{ mm}$

$ch := 10 \text{ mm}$

C.1 Type I wall

Wall thickness $t := 70 \text{ mm}$

Wall width $b := 750 \text{ mm}$

Wall height $h := 750 \text{ mm}$

By *fib Model Code 2010*

Empirical parameter $k := 1.0$

Mean bond strength $\tau_{bms} := 1.8 \text{ MPa} \cdot f_{ctm}$

x-direction

Number of bars over height $n_y := 10$

Number of bars over width $n_x := 13$

Reinforcement per unit length wall

$$A_{sx} := \frac{n_y}{h} \cdot (\pi \cdot 0.25 \cdot \phi_h^2 + \pi \cdot 0.25 \cdot \phi_s^2) = 0.577 \frac{\text{mm}^2}{\text{mm}}$$

Effective concrete area in tension per unit length of wall

$$A_{ceffx} := \min\left(2.5 \cdot (ch + 0.5 \cdot \phi m), \frac{t}{2}\right) = 31.4 \frac{mm^2}{mm}$$

$$\text{Ratio reinforcement to effective concrete area } \rho_{sefx} := \frac{A_{sx}}{A_{ceffx}} = 0.018$$

Average crack spacing in x-direction

$$s_{rmaxxI} := 2 \cdot \left(k \cdot ch + \frac{0.25}{1.8} \cdot \frac{\phi m}{\rho_{sefx}}\right) = 97.5 \text{ mm}$$

y-direction

$$\text{Reinforcement per unit length wall } A_{sy} := \pi \cdot 0.25 \cdot \phi v^2 \cdot \frac{nx}{h} = 0.871 \frac{mm^2}{mm}$$

Effective concrete area in tension per unit length of wall

$$A_{ceffy} := \min\left(2.5 \cdot (cv + 0.5 \cdot \phi v), \frac{t}{2}\right) = 35 \frac{mm^2}{mm}$$

$$\text{Ratio reinforcement to effective concrete area } \rho_{sefy} := \frac{A_{sy}}{A_{ceffy}} = 0.025$$

Average crack spacing in y-direction

$$s_{rmaxyI} := 2 \cdot \left(k \cdot 1 \cdot cv + \frac{0.25}{1.8} \cdot \frac{\phi v}{\rho_{sefy}}\right) = 117.3 \text{ mm}$$

By TKT4222 Concrete Structures 3

Total reinforcement area in x-direction, one side of the wall width. Including horizontal shear reinforcement.

$$A_{sxtot} := nx \cdot \frac{(\pi \cdot 0.25 \cdot \phi h^2 + \pi \cdot 0.25 \cdot \phi s^2)}{h} = 576.6 \frac{1}{m} \cdot mm^2$$

$$A_{sytot} := nx \cdot \pi \cdot 0.25 \cdot \frac{\phi v^2}{b} = 871.3 \frac{1}{m} \cdot mm^2$$

Alternative 2

Crack angle at pure shear

$$\theta 2 := \text{atan}\left(\frac{A_{sxtot}}{A_{sytot}}\right)^{0.5} = 0.76 \text{ rad}$$

$$\text{Crack spacing } l_{smax\theta 2I} := \frac{1}{\frac{\cos(\theta 2)}{s_{rmaxxI}} + \frac{\sin(\theta 2)}{s_{rmaxyI}}} = 75.2 \text{ mm}$$

Alternative 3

Crack angle at pure shear

$$\theta 3 := \text{atan}\left(\frac{A_{sxtot}}{A_{sytot}}\right)^{0.25} = 0.87 \text{ rad}$$

$$\text{Crack spacing } l_{smax\theta 3I} := \frac{1}{\frac{\cos(\theta 3)}{s_{rmaxxI}} + \frac{\sin(\theta 3)}{s_{rmaxyI}}} = 76.2 \text{ mm}$$

Average crack spacing type I wall

$$l_{avI} := \frac{(l_{smax\theta 2I} + l_{smax\theta 3I})}{2} = 75.7 \text{ mm}$$

$$\text{Equivalent length type I wall 3D } heqI := (150 \text{ mm} \cdot 150 \text{ mm} \cdot 70 \text{ mm})^{\frac{1}{3}} = 116.3 \text{ mm}$$

$$\text{Resulting modification factor in 3D for type I wall } ncrI := \frac{heqI}{l_{avI}} = 1.54$$

C.2 Type II wall

Wall thickness $t := 65 \text{ mm}$

Wall width $b := 650 \text{ mm}$

Wall height $h := 1300 \text{ mm}$

By fib Model Code 2010

Empirical parameter $k := 1.0$

Mean bond strength $\tau_{bms} := 1.8 \text{ MPa} \cdot f_{ctm}$

x-direction

Including horizontal shear stirrups in A_{sx}

$$\phi_{sx} := \phi_s + \phi_h = 10.25 \text{ mm}$$

Number of bars over height $n_y := 12$

Number of bars over width $n_x := 11$

Reinforcement per unit length wall

$$A_{sx} := \frac{n_y}{h} \cdot (\pi \cdot 0.25 \cdot \phi_h^2 + \pi \cdot 0.25 \cdot \phi_s^2) = 0.399 \frac{\text{mm}^2}{\text{mm}}$$

Effective concrete area in tension per unit length of wall

$$A_{ceffx} := \min\left(2.5 \cdot (ch + 0.5 \phi_m), \frac{t}{2}\right) = 31.4 \frac{\text{mm}^2}{\text{mm}}$$

$$\text{Ratio reinforcement to effective concrete area } \rho_{sefx} := \frac{A_{sx}}{A_{ceffx}} = 0.013$$

Average crack spacing in x-direction

$$s_{rmaxxII} := 2 \cdot \left(k \cdot ch + \frac{0.25}{1.8} \cdot \frac{\phi_m}{\rho_{sefx}} \right) = 132 \text{ mm}$$

y-direction

$$\text{Reinforcement per unit length wall } A_{sy} := \pi \cdot 0.25 \cdot \phi_v^2 \cdot \frac{n_x}{b} = 0.851 \frac{\text{mm}^2}{\text{mm}}$$

Effective concrete area in tension per unit length of wall

$$A_{ceffy} := \min\left(2.5 \cdot (cv + 0.5 \phi_v), \frac{t}{2}\right) = 32.5 \frac{\text{mm}^2}{\text{mm}}$$

$$\text{Ratio reinforcement to effective concrete area } \rho_{sefy} := \frac{A_{sy}}{A_{ceffy}} = 0.026$$

Average crack spacing in y-direction

$$srmaxyII := 2 \cdot \left(k \cdot 1 \cdot cv + \frac{0.25}{1.8} \cdot \frac{\phi v}{\rho sefy} \right) = 112.9 \text{ mm}$$

By TKT4222 Concrete Structures 3

Total reinforcement area in x-direction, one side of the wall width. Including horizontal shear reinforcement.

$$Asxtot := ny \cdot \frac{(\pi \cdot 0.25 \cdot \phi h^2 + \pi \cdot 0.25 \cdot \phi s^2)}{h} = 399.2 \frac{1}{m} \cdot mm^2$$

$$Asytot := nx \cdot \pi \cdot 0.25 \cdot \frac{\phi v^2}{b} = 850.6 \frac{1}{m} \cdot mm^2$$

Alternative 2

Crack angle at pure shear

$$\theta 2 := \text{atan} \left(\frac{Asxtot}{Asytot} \right)^{0.5} = 0.66 \text{ rad}$$

$$\text{Crack spacing } lsmax\theta 2II := \frac{1}{\frac{\cos(\theta 2)}{srmaxxII} + \frac{\sin(\theta 2)}{srmaxyII}} = 87.6 \text{ mm}$$

Alternative 3

Crack angle at pure shear

$$\theta 3 := \text{atan} \left(\frac{Asxtot}{Asytot} \right)^{0.25} = 0.81 \text{ rad}$$

$$\text{Crack spacing } lsmax\theta 3II := \frac{1}{\frac{\cos(\theta 3)}{srmaxxII} + \frac{\sin(\theta 3)}{srmaxyII}} = 85.9 \text{ mm}$$

Average crack spacing type I wall

$$lavII := \frac{(lsmax\theta 2II + lsmax\theta 3II)}{2} = 86.7 \text{ mm}$$

Equivalent length type II wall 2D

$$heqII2D := (130 \text{ mm} \cdot 130 \text{ mm})^{\frac{1}{2}} = 130 \text{ mm}$$

Equivalent length type II wall 3D

$$heqII3D := (130 \text{ mm} \cdot 130 \text{ mm} \cdot 65 \text{ mm})^{\frac{1}{3}} = 103.2 \text{ mm}$$

$$\text{Resulting modification factor in 2D for type II wall } ncrII2D := \frac{heqII2D}{lavII} = 1.5$$

$$\text{Resulting modification factor in 3D for type II wall } ncrII3D := \frac{heqII3D}{lavII} = 1.19$$

D. Parabolic compression curve in DIANA

A single-element finite element model was used to study the behaviour of the parabolic compression curve in DIANA 9.6, as the user manual was some ambiguous regarding increase of peak strain in addition to peak stress [A4]. The stress and strains presented are global vertical Gaussian values σ_{zz} and ϵ_{zz} extracted from the base surface mid integration point. The results are presented in section 6.2.

The concrete material data from Table 4.2 was used. Three orthogonal surfaces of the element was constrained for lateral displacements. Hydrostatic pressure was applied in an initial phase on two surfaces, while the last free surface was subjected to a compressive displacement load using phased analysis. Due to difficulties in obtaining a consistent behaviour for low hydrostatic stresses, several geometry definitions of the single element was attempted. The initial single-element model was the actual size of the solid elements in the 3D base model presented in Figure D.1(a). The inconsistency of the peak strain discussed in section 6.2 was suspected to be a size dependency, resulting in a snap-back effect in the response. A cube of 10 mm edges was analysed, with similar results. The results are presented in Figure 6.1. The study proved only the descending branch to be governed by G_c , and indicated no significant increase of peak strain in confined concrete.

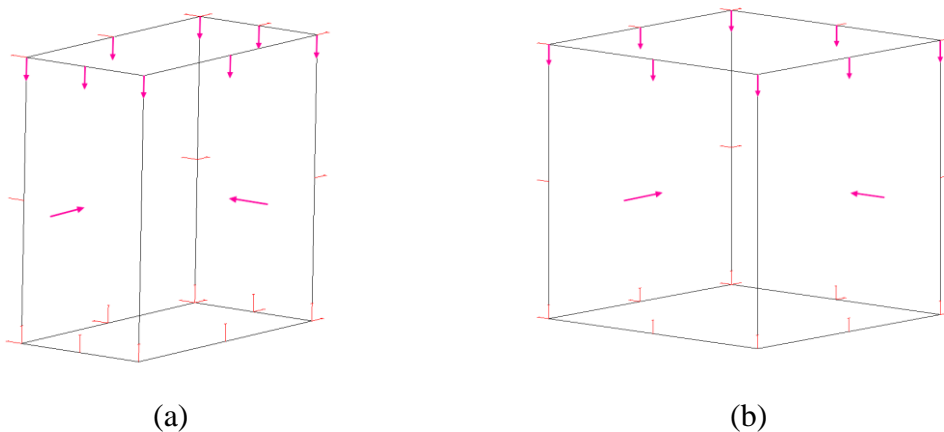


Figure D.1: Finite element size used in one-element study. (a) 3D base model solid element and (b) 10 mm cube.

E. Strut-and-tie modelling of SW21

The parameters used in these calculations are illustrated in Figure 8.1. The global equilibrium was solved iteratively by changing the number of bars in tension n to gain maximum capacity within limitation of maximum geometrical width b . Capacity controls at the joints in STM afterwards against this global force F_H . The highest possible design capacity for these strut-and-tie models was found for $n=6$, implying six vertical reinforcement bar rows in tension, that is 12 bars. The calculation for $n=6$ is presented below for both STM1 and STM2, though generating the same design capacity $R_{dSTM}=62.2$ kN.

Wall geometry properties

Width $b := 650$ mm

Height $h := 1300$ mm

Thickness $t := 65$ mm

The number of reinforcement bars in tension, the width of the compression zone x and the following internal moment arm z and angle θ are all unknowns.

Reinforcement geometry properties

Vertical bar diameter $\phi_v := 8$ mm

Horizontal bar diameter $\phi_h := 6.25$ mm

Spacing vertical bars $sv := 62$ mm

Spacing horizontal bars $sh := 115$ mm

Assumed distance center outer tensile bar to tensile edge $st := 15$ mm

The tensile reinforcement area was assumed, and used to solve the unknowns.

Assumed number of rows of vertical reinforcement bars in pure tension $n := 6$

Reinforcement area in pure tension $A_s := (\pi \cdot 0.25 \cdot \phi_v^2 \cdot 2 \cdot n) = 603.19$ mm²

Material properties

Partial safety factor concrete $\gamma_c := 1.5$

Partial safety factor steel $\gamma_s := 1.15$

Concrete characteristic strength $f_{ck} := 28.4$ MPa

Concrete design strength $f_{cd} := 0.85 \cdot \frac{f_{ck}}{\gamma_c} = 16.1$ MPa

Steel characteristic yield strength vertical $f_{yk} := 470$ MPa

Steel design yield strength vertical $f_{yd} := \frac{f_{yk}}{\gamma_s} = 408.7$ MPa

Steel characteristic yield strength horizontal $f_{ykh} := 520$ MPa

Steel design yield strength horizontal $f_{ydh} := \frac{f_{ykh}}{\gamma_s} = 452.2$ MPa

Capacity check of STM after Eurocode 1992-1-1, 6.5. Reduced concrete strengths:

$$6.5.2(2): \nu' := 1 - \frac{28.38}{250} = 0.886 \quad \text{where } f_{ck} = 28.4 \text{ MPa}$$

Reduced concrete design strength in joints after EC2, 6.5.4(4):

a) joints connecting only struts

$$\sigma_{ja} := 1 \cdot \nu' \cdot f_{cd} = 14.3 \text{ MPa}$$

b) joints connecting struts, and ties in one direction

$$\sigma_{jb} := 0.85 \cdot \nu' \cdot f_{cd} = 12.1 \text{ MPa}$$

c) joints connecting struts and ties in multiple directions

$$\sigma_{jc} := 0.75 \cdot \nu' \cdot f_{cd} = 10.7 \text{ MPa}$$

A reduced value for a pure compressive field after EC2, 6.5.2(2) was not used in dimensioning of the struts as the width and distribution of the struts are not known. Strut capacity is checked at joints limited by the physical geometry of the wall and with reduced strengths as defined above. A rectangular distribution of the struts at the joints is assumed, and the minimum distance perpendicular to the struts axis to the wall edge is limiting.

Global equilibrium

$$\text{Global tensile force } FT := f_{yd} \cdot A_s = 246.5 \text{ kN}$$

Assume uniform distribution of the tensile force on all bars.

$$\text{Horizontal location of FT from tensile edge } s := \frac{(n-1) \cdot sv}{2} + st = 170 \text{ mm}$$

$$\text{Distance from FT to maximum compressive fibre } d := b - s = 480 \text{ mm}$$

Calculates the compression zone as uniformly distributed with width x by use of a reduced concrete design strength after EC2 for joint only connecting struts:

$$\text{Width of compression zone } x := \frac{FT}{\sigma_{ja} \cdot t} = 265.8 \text{ mm}$$

$$\text{Internal moment arm } z := d - \frac{x}{2} = 347.1 \text{ mm}$$

$$\text{Total width used } bt := 2 \cdot s + x = 605.8 \text{ mm}$$

Can not allow for $bt > b = 650 \text{ mm}$ **CHECK**

$$\text{Vertical global force equilibrium } FC := FT = 246.5 \text{ kN}$$

$$\text{Global moment about point 1 } FH := FC \cdot \frac{z}{hl} = 62.2 \text{ kN}$$

FH = Rd for the wall as long the capacity at the joints is verified, following check at the joints.

E.1 Design capacity of STM1

Distance from base to load point $hl := 1375 \text{ mm}$

Number of frames $nf := 1$

1=STM1, 2=STM2

Height of tie T1 $hf := \frac{hl}{nf} = 1375 \text{ mm}$

Angle of frame $\theta := \text{atan}\left(\frac{hf}{z}\right) = 1.32 \text{ rad}$

Angle of frame in degrees $\theta d := \theta = 75.8 \text{ deg}$

Equilibrium in joint 4

Horizontal force

$$S2 := FH = 62.2 \text{ kN}$$

Equilibrium in joint 3

Horizontal force

$$S1 := \frac{S2}{\cos(\theta)} = 254.3 \text{ kN}$$

Vertical force

$$T1 := S1 \cdot \sin(\theta) = 246.5 \text{ kN}$$

Equilibrium in joint 2

Horizontal force control

$$FH := S1 \cdot \cos(\theta) = 62.2 \text{ kN}$$

Vertical force control

$$FC := S1 \cdot \sin(\theta) = 246.5 \text{ kN}$$

Equilibrium in joint 1

$$FT := T1 = 246.5 \text{ kN}$$

Equilibrium globally and in joints confirmed. Need to check capacity of the struts and ties, look at the joints.

Capacity check of STM1

Joint 2

Width of strut based on force S1 $tS1 := \frac{S1}{\sigma_{ja} \cdot t} = 274.2 \text{ mm}$

Geometrical limitation of strut S1 at joint 2 $tg12 := 2 \cdot \left(\frac{0.5 \cdot x}{\cos\left(\frac{\pi}{2} - \theta\right)} \right) = 274.2 \text{ mm}$

$tg12 > tS1$? **CHECK**

Same dimension of the widths due to global equilibrium and use of same reduction in calculation of x.FH assumed unlimited width the wall and foundation.

Joint 3

Geometrical limitation of strut S1 at joint 3 $tg13 := 2 \cdot \left(\frac{s}{\cos\left(\frac{\pi}{2} - \theta\right)} \right) = 350.7 \text{ mm}$

$tg13 > tS1$? **CHECK**

Joint 4

Width of strut based on force S2 $tS2 := \frac{S2}{\sigma_{ja} \cdot t} = 67.1 \text{ mm}$ Linear elastic top beam.

Geometrical limitation of S2 at joint 3 $tg24 := 2 \cdot 75 \text{ mm} = 150 \text{ mm}$

$tg24 > tS2$? **CHECK**

E.2 Design capacity of STM2

The same wall geometry properties, reinforcement properties and strength reduction formulas applies for STM2, only height of tie hf and angle θ differs.

Distance from base to load point $hl := 1375 \text{ mm}$

Number of frames $nf := 2$

1=STM1, 2=STM2

Height of tie T1 $hf := \frac{hl}{nf} = 687.5 \text{ mm}$

Angle of frame $\theta := \text{atan}\left(\frac{hf}{z}\right) = 1.1 \text{ rad}$

Angle of frame in degrees $\theta d := \theta = 63.2 \text{ deg}$

Equilibrium in joint 4

Horizontal force

$$S4 := FH = 62.2 \text{ kN}$$

Equilibrium in joint 3

Horizontal force

$$S3 := \frac{S4}{\cos(\theta)} = 138.1 \text{ kN}$$

Vertical force

$$T2 := S3 \cdot \sin(\theta) = 123.3 \text{ kN}$$

Equilibrium in joint 5

Horizontal force

$$T3 := S3 \cdot \cos(\theta) = 62.2 \text{ kN}$$

Vertical force

$$S2 := S3 \cdot \sin(\theta) = 123.3 \text{ kN}$$

Equilibrium in joint 6

Horizontal force

$$S1 := \frac{T3}{\cos(\theta)} = 138.1 \text{ kN}$$

Vertical force

$$T1 := T2 + S1 \cdot \sin(\theta) = 246.5 \text{ kN}$$

Equilibrium in joint 2

Horizontal force control

$$FH := S1 \cdot \cos(\theta) = 62.2 \text{ kN}$$

Vertical force control

$$FC := S2 + S1 \cdot \sin(\theta) = 246.5 \text{ kN}$$

Equilibrium in joint 1

Vertical force control

$$FT := T1 = 246.5 \text{ kN}$$

Equilibrium globally and in joints is confirmed. Need to check capacity of the joints.

Capacity check of STM2**Joint 4**

Only connecting struts.

$$\text{Width of strut based on force S4 } tS4 := \frac{S4}{\sigma_{ja} \cdot t} = 67.1 \text{ mm}$$

$$\text{Geometrical limitation of S4 at joint 4 } tg44 := 2 \cdot 75 \text{ mm} = 150 \text{ mm}$$

$tg44 > tS4$? **CHECK**

Joint 3

Connecting tie in one direction

$$\text{Width of strut based on force S3 } tS3 := \frac{S3}{\sigma_{jb} \cdot t} = 175.2 \text{ mm}$$

$$\text{Geometrical limitation of strut S3 at joint 3 } tg33 := 2 \cdot \frac{s}{\cos\left(\frac{\pi}{2} - \theta\right)} = 380.9 \text{ mm}$$

$tg33 > tS3$? **CHECK**

Geometrical limitation of strut S4 at joint 3 same as in joint 4.

Joint 5

Connecting tie in one direction

$$\text{Width of strut based on force S2 } tS2 := \frac{S2}{\sigma_{jb} \cdot t} = 156.4 \text{ mm}$$

$$\text{Geometrical limitation of strut S2 at joint 5 } tg25 := x = 265.8 \text{ mm}$$

Geometrical limitation of strut S3 in joint 5 $tg35 := 2 \cdot \left(\frac{0.5 \cdot x}{\cos\left(\frac{\pi}{2} - \theta\right)} \right) = 297.8 \text{ mm}$

$tg25 > tS2$? **CHECK**

$tg35 > tS3$? **CHECK**

Reinforcement area required by T3 $Ashreq := \frac{T3}{fydh} = 137.6 \text{ mm}^2$

Required number of rows of horizontal bars $nh := \frac{Ashreq}{\pi \cdot 0.25 \cdot \phi h^2 \cdot 2} = 2.2$

Assumes maximum of three horizontal bars in tie T3.

$nh < 3$? **CHECK**

Joint 6

Connecting tie in two directions.

Tie T1 is already dimensioned at calculation of global force FT. T2 is half the force of T1, no further control necessary.

Width of strut based on force S1, ties in two directions $tS1 := \frac{S1}{\sigma jc \cdot t} = 198.5 \text{ mm}$

Geometrical limitation of strut S1 in joint 6 $tg16 := 2 \cdot \frac{s}{\cos\left(\frac{\pi}{2} - \theta\right)} = 380.9 \text{ mm}$

$tg16 > tS1$? **CHECK**

Joint 2

Only struts connected. Compressive zone controlled by calculation of FC, and z, x calculated on reduced strength for joint connecting struts. S2 limited in joint 5 due to lower strength, same for S1. Assume unlimited area of distribution for FH in joint 2.

F. Analysis files from DIANA 9.6

The nonlinear finite element analysis results presented in this thesis utilize various finite element models for the structural walls, though with minor differences. The input data file and analysis command file for the wall specimen SW22 are enclosed, which utilizes the solution strategy defining the 3D base model with additional applied axial loading and a phased analysis procedure. Note that the material parameters in SW22 differ from the 3D base model. In addition, the analysis file for the 3D base model SW21 is provided.

F.1 Data input file for SW22

Note that the provided .dat file is not complete due to the extensive amount of coordinate positions, node numbers and reinforcement bar elements. Areas with omitted lines are marked by vertical dots.

```
: Diana Datafile written for Diana 9.6
FEMGEN MODEL   : SW22
ANALYSIS TYPE  : Structural 3D
'UNITS'
LENGTH MM
TIME SEC
TEMPER KELVIN
FORCE N
'COORDINATES'
  1  0.000000E+00 -3.250000E+01  0.000000E+00
  2  1.300000E+02 -3.250000E+01  0.000000E+00
      .
      .
      .
507  1.300000E+02  3.250000E+01  1.412500E+03
508  0.000000E+00  3.250000E+01  1.412500E+03
'ELEMENTS'
SET B1
CONNECTIVITY
  1 CHX60 1 13 2 19 8 24 7 18 85 94 199 208 60 89 64 213 159 203 163
    212
  2 CHX60 2 14 3 20 9 25 8 19 94 103 190 199 64 98 68 214 155 194
    159 213
      .
      .
      .
24 CHX60 69 113 73 228 144 173 148 227 108 117 168 177 32 44 33 50
```

APPENDIX F. ANALYSIS FILES FROM DIANA 9.6

39 55 38 49
25 CHX60 73 122 77 135 131 164 144 228 117 126 139 168 33 45 34 51
40 56 39 50
MATERIAL 2
DATA 1
SET B2
CONNECTIVITY
26 CHX60 29 41 30 47 36 52 35 46 285 294 399 408 260 289 264 413
359 403 363 412
27 CHX60 30 42 31 48 37 53 36 47 294 303 390 399 264 298 268 414
355 394 359 413
.
.
.
49 CHX60 269 313 273 428 344 373 348 427 308 317 368 377 232 244
233 250 239 255 238 249
50 CHX60 273 322 277 335 331 364 344 428 317 326 339 368 233 245
234 251 240 256 239 250
MATERIAL 2
DATA 1
SET B3
CONNECTIVITY
51 CHX60 229 241 230 247 236 252 235 246 457 458 467 468 429 441
430 447 436 452 435 446
52 CHX60 230 242 231 248 237 253 236 247 458 459 466 467 430 442
431 448 437 453 436 447
53 CHX60 231 243 232 249 238 254 237 248 459 460 465 466 431 443
432 449 438 454 437 448
54 CHX60 232 244 233 250 239 255 238 249 460 461 464 465 432 444
433 450 439 455 438 449
55 CHX60 233 245 234 251 240 256 239 250 461 462 463 464 433 445
434 451 440 456 439 450
MATERIAL 1
DATA 1
SET B4
CONNECTIVITY
56 CHX60 429 441 430 447 436 452 435 446 497 498 507 508 469 481
470 487 476 492 475 486
57 CHX60 430 442 431 448 437 453 436 447 498 499 506 507 470 482
471 488 477 493 476 487
58 CHX60 431 443 432 449 438 454 437 448 499 500 505 506 471 483
472 489 478 494 477 488
59 CHX60 432 444 433 450 439 455 438 449 500 501 504 505 472 484
473 490 479 495 478 489
60 CHX60 433 445 434 451 440 456 439 450 501 502 503 504 473 485
474 491 480 496 479 490
MATERIAL 1
DATA 1
'REINFORCEMENTS'
SET VERT1
LOCATI
143 BAR
LINE 1.500000E+01 -1.750000E+01 0.000000E+00
1.500000E+01 -1.750000E+01 1.430000E+03
MATERIAL 5
GEOMETRY 3
SET VERT2
LOCATI
144 BAR

LINE 7.700000E+01 -1.750000E+01 0.000000E+00
 7.700000E+01 -1.750000E+01 1.430000E+03

MATERIAL 5
 GEOMETRY 3

.
 .
 .

SET HOR1

LOCATI
 165 BAR

LINE 1.000000E+01 -9.500000E+00 1.500000E+01
 6.400000E+02 -9.500000E+00 1.500000E+01

MATERIAL 4
 GEOMETRY 2

SET HOR2

LOCATI
 166 BAR

LINE 1.000000E+01 -9.500000E+00 1.300000E+02
 6.400000E+02 -9.500000E+00 1.300000E+02

.
 .
 .

SET SHRC11

LOCATI
 283 BAR

LINE 5.100000E+02 2.150000E+01 1.165000E+03
 6.390000E+02 2.150000E+01 1.165000E+03

MATERIAL 3
 GEOMETRY 1

SET SHRC12

LOCATI
 284 BAR

LINE 5.100000E+02 2.150000E+01 1.280000E+03
 6.390000E+02 2.150000E+01 1.280000E+03

MATERIAL 3
 GEOMETRY 1

'MATERIALS'

1 NAME CONLIN
 YOUNG 3.04110E+04
 POISON 1.50000E-01
 2 NAME CONCRETE
 YOUNG 3.04110E+04
 POISON 1.50000E-01
 TOTCRK FIXED
 TENCrv EXPONE
 TENSTR 3.23000E+00
 GF1 0.83300E-01
 COMCRV PARABO
 COMSTR 4.30100E+01
 GC 2.08240E+01
 CNFCRV VECCHI
 REDCRV VC1993
 REDMIN 4.00000E-01
 SHRCRV CONSTA
 BETA 1.00000E-01
 POIRED DAMAGE
 3 NAME RE4H
 YOUNG 2.00000E+05

APPENDIX F. ANALYSIS FILES FROM DIANA 9.6

```

YIELD  VMISES
HARDEN  WORK
HARDIA4  430.0 0.0 634.1 0.05
4 NAME  RE625H
YOUNG  2.00000E+05
YIELD  VMISES
HARDEN  WORK
HARDIA625 530.0 0.0 734.1 0.05
5 NAME  RE8H
YOUNG  2.00000E+05
YIELD  VMISES
HARDEN  WORK
HARDIA8  480.0 0.0 684.1 0.05
'GEOMETRY'
1 NAME  SHEAR
  CROSSE 1.25700E+01
2 NAME  HOR
  CROSSE 3.06800E+01
3 NAME  VERT
  CROSSE 5.02700E+01
'DATA'
1 NINTEG 3 3 3
'GROUPS'
REINFO
1 VERTW / VERT1 VERT2 VERT3 VERT4 VERT5 VERT6 VERT7 VERT8 VERT9 VERT10
  VERT11 VERTC1 VERTC2 VERTC3 VERTC4 VERTC5 VERTC6 VERTC7 VERTC8
  VERTC9 VERTC10 VERTC11 /
2 HORW / HOR1 HOR2 HOR3 HOR4 HOR5 HOR6 HOR7 HOR8 HOR9 HOR10 HOR11 HOR12
  HORC1 HORC2 HORC3 HORC4 HORC5 HORC6 HORC7 HORC8 HORC9 HORC10
  HORC11 HORC12 /
3 SHW / SHL1 SHL2 SHL3 SHL4 SHL5 SHL6 SHL7 SHL8 SHL9 SHL10 SHL11 SHL12
  SHR1 SHR2 SHR3 SHR4 SHR5 SHR6 SHR7 SHR8 SHR9 SHR10 SHR11 SHR12
  SHLC1 SHLC2 SHLC3 SHLC4 SHLC5 SHLC6 SHLC7 SHLC8 SHLC9 SHLC10
  SHLC11 SHLC12 SHRC1 SHRC2 SHRC3 SHRC4 SHRC5 SHRC6 SHRC7 SHRC8
  SHRC9 SHRC10 SHRC11 SHRC12 TSHL1 TSHL2 TSHL3 TSHL4 TSHL5 TSHL6
  TSHL7 TSHL8 TSHL9 TSHL10 TSHL11 TSHL12 TSHR1 TSHR2 TSHR3 TSHR4
  TSHR5 TSHR6 TSHR7 TSHR8 TSHR9 TSHR10 TSHR11 TSHR12 TSHLI1 TSHLI2
  TSHLI3 TSHLI4 TSHLI5 TSHLI6 TSHLI7 TSHLI8 TSHLI9 TSHLI10 TSHLI11
  TSHLI12 TSHRI1 TSHRI2 TSHRI3 TSHRI4 TSHRI5 TSHRI6 TSHRI7 TSHRI8
  TSHRI9 TSHRI10 TSHRI11 TSHRI12 /
'SUPPORTS'
NAME SET_1
/ 1-28 / TR 1
/ 1-28 / TR 2
/ 1-28 / TR 3
NAME SET_2
/ 1-28 434 440 451 / TR 1
/ 1-28 / TR 2
/ 1-28 / TR 3
'LOADS'
CASE 1
ELEMEN
/ 56-60 /
  FACE  ZETA2
  FORCE  -0.4307700E+01
  DIRECT 3
CASE 2
DEFORM
/ 434 440 451 / TR 1 -0.100000E+01

```

```
'DIRECTIONS'
  1 1.000000E+00 0.000000E+00 0.000000E+00
  2 0.000000E+00 1.000000E+00 0.000000E+00
  3 0.000000E+00 0.000000E+00 1.000000E+00
'END'
```

F.2 Analysis command file with phased analysis for SW22

```
*FILOS
INITIA
*INPUT
READ FILE "SW22.dat"
*PHASE
BEGIN ACTIVE
  SUPPORT SET_1
END ACTIVE
*NONLIN
BEGIN EXECUT
  BEGIN LOAD
    LOADNR 1
    STEPS EXPLIC SIZES 0.1(10)
  END LOAD
  BEGIN ITERAT
    BEGIN CONVER
      FORCE CONTIN
      DISPLA OFF
      BEGIN ENERGY
        TOLCON 0.001
        CONTIN
      END ENERGY
    END CONVER
    MAXITE 50
    METHOD NEWTON REGULA
    LINESE MAXLS 10
  END ITERAT
END EXECUT
BEGIN OUTPUT
FILE "AXIAL"
  DISPLA TOTAL TRANSL GLOBAL
  DISPLA PHASE
  FORCE REACTI TRANSL GLOBAL
  PARAME BANDWI
  STRAIN CRACK GREEN
  STRAIN TOTAL GREEN GLOBAL INTPNT
  STRAIN TOTAL GREEN LOCAL INTPNT
  STRAIN TOTAL GREEN GLOBAL
  STRAIN TOTAL GREEN PRINCI INTPNT
  STRAIN TOTAL TRACTI LOCAL
  STRESS TOTAL CAUCHY GLOBAL INTPNT
  STRESS TOTAL CAUCHY LOCAL INTPNT
  STRESS TOTAL CAUCHY GLOBAL
  STRESS TOTAL CAUCHY PRINCI INTPNT
  STRESS TOTAL TRACTI LOCAL
  STRESS CRACK CAUCHY LOCAL
```

```

END OUTPUT
*PHASE
RENEW
BEGIN ACTIVE
  SUPPORT SET_2
END ACTIVE
*NONLIN
BEGIN EXECUT
  BEGIN START
  LOAD PREVIO
  END START
END EXECUT
BEGIN EXECUT
  BEGIN LOAD
  LOADNR 2
  BEGIN STEPS
  BEGIN EXPLIC
  SIZES 1e-15 0.1(5) 0.5(41)
  END EXPLIC
  END STEPS
END LOAD
BEGIN ITERAT
  BEGIN CONVER
  FORCE CONTIN
  DISPLA OFF
  BEGIN ENERGY
  TOLCON 0.001
  CONTIN
  END ENERGY
  END CONVER
  MAXITE 50
  METHOD NEWTON REGULA
  LINESE MAXLS 10
END ITERAT
END EXECUT
BEGIN OUTPUT
FILE "HORDISP"
DISPLA PHASE
DISPLA TOTAL TRANSL GLOBAL
FORCE REACTI TRANSL GLOBAL
PARAME BANDWI
STRAIN CRACK GREEN
STRAIN TOTAL GREEN GLOBAL INTPNT
STRAIN TOTAL GREEN LOCAL INTPNT
STRAIN TOTAL GREEN GLOBAL
STRAIN PLASTI GREEN GLOBAL INTPNT
STRAIN TOTAL GREEN PRINCI INTPNT
STRAIN TOTAL TRACTI LOCAL
STRESS TOTAL CAUCHY GLOBAL INTPNT
STRESS TOTAL CAUCHY LOCAL INTPNT
STRESS TOTAL CAUCHY GLOBAL
STRESS TOTAL CAUCHY PRINCI INTPNT
STRESS TOTAL TRACTI LOCAL
STRESS CRACK CAUCHY LOCAL
END OUTPUT
*END

```

F.3 Analysis command file for SW21: 3D base model

```

*FILOS
INITIA
*INPUT
*NONLIN LABEL="Structural nonlinear"
BEGIN EXECUT
  BEGIN LOAD
    LOADNR 2
    STEPS EXPLIC SIZES 0.100000(5) 0.500000(41)
  END LOAD
  BEGIN ITERAT
    MAXITE 50
    METHOD NEWTON
    LINESE MAXLS 10
    BEGIN CONVER
      FORCE CONTIN
      DISPLA OFF
      BEGIN ENERGY
        TOLCON 0.001
        CONTIN
      END ENERGY
    END CONVER
  END ITERAT
END EXECUT
SOLVE PARDIS
BEGIN OUTPUT
  TEXT "Output"
  FEMVIE
  BINARY
  FILE A212
  SELECT STEPS ALL /
  DISPLA TOTAL TRANSL GLOBAL
  STRAIN TOTAL GREEN GLOBAL INTPNT
  STRAIN TOTAL GREEN GLOBAL
  STRAIN TOTAL GREEN PRINCI INTPNT
  STRAIN PLASTI GREEN GLOBAL INTPNT
  STRAIN TOTAL GREEN VOLUME INTPNT
  STRAIN CRACK GREEN
  STRESS TOTAL CAUCHY GLOBAL
  STRESS CRACK CAUCHY LOCAL
  STRESS TOTAL CAUCHY PRINCI INTPNT
  STRESS TOTAL CAUCHY GLOBAL INTPNT
  FORCE REACTI TRANSL GLOBAL
END OUTPUT
*END

```

References in appendices

- A1. Irgens F. Fasthetslære. Trondheim: Tapir akademisk forl.; 2006.
- A2. *fib. fib* Model Code for Concrete Structures 2010. Ernst & Sohn. 2013.
- A3. Øverli J.A. TKT4222 Concrete Structures 3. Trondheim: Department of Structural Engineering, NTNU; 2014.
- A4. TNO DIANA. DIANA User's Manual Material Library Release 9.6. 2015.